Advanced Resist Materials for Next Generation Lithography

by

Carmen-Mariana Popescu

A thesis submitted to The University of Birmingham
for the degree of Doctor of Philosophy

School of Physics and Astronomy

University of Birmingham

January 2019

UNIVERSITY OF
BIRMINGHAM

University of Birmingham Research Archive

e-theses repository

This unpublished thesis/dissertation is copyright of the author and/or third parties. The intellectual property rights of the author or third parties in respect of this work are as defined by The Copyright Designs and Patents Act 1988 or as modified by any successor legislation.

Any use made of information contained in this thesis/dissertation must be in accordance with that legislation and must be properly acknowledged. Further distribution or reproduction in any format is prohibited without the permission of the copyright holder.

Abstract

With the advancement in technology the minimum lithographic feature size decreases more and more for every generation. The development of lithographic techniques and resist materials capable of meeting the requirements for the upgraded technology (resolution, sensitivity, roughness) started to play a trivial role.

However, the issue represents a fundamental principle in lithography (the RLS trade-off) and it proves difficult to overcome. Addition of quenchers in chemically amplified resists reduces the acid diffusion length and improves the line edge roughness and increases the resolution of the patterned features, but decreases the sensitivity. The current most commonly researched approach to boost the sensitivity in organic resists is the addition of metals embedded in the molecular structure by covalent bonds. This approach was investigated in this thesis, and an extension towards high-Z organic additive compounds and high-Z cross-linkers was conducted.

Furthermore as feature sizes less than 20 nm are routinely required, pattern collapse driven by the capillary forces upon development has become a serious limiting factor, independent of the lithography technique involved. Alongside with constantly developing the resist platforms there is also the need to improve the adhesion of the resist material to the silicon substrate, reducing pattern collapse and allowing for ultra high resolution and high aspect ratio patterning.

In this thesis I will present the research I have undertaken in order to implement a resist platform suitable for next generation lithography and I will introduce and

describe the new multi-trigger mechanism concept developed for this resist system. I will also present a study on active underlayes investigated for improved adhesion between the resist and the substrate.

To My Parents

Acknowledgements

I thank Dr. Alex P.G. Robinson for his supervision and suggestions in the past 4 years, and for giving me the opportunity to conduct this work.

I am thankful to the entire Irresistible Materials team especially Alex McClelland for all her advice and fruitful discussions.

I thank my second supervisor Dr. Wolfgang Theis and Prof. Richard Palmer for giving me the opportunity to work in NPRL.

Special thanks to people at Paul Scherrer Institute, Switzerland, especially Michaela Vockenhuber, Dimitrios Kazazis and Yasin Eckinci for their technical support in EUV-IL and EBL experiments.

Very special thanks to my parents and my sister for their support and for believing in me throughout my entire life.

List of Publications

Multi Trigger Resist for EUV Lithography, **Carmen Popescu**, Y. Vesters, A. McClelland, D. De Simone, G. Dawson, J. Roth, W. Theis, G. Vandenberghe, A.P.G. Robinson, Journal of Photopolymer Science and Technology, 31 (2018).

Multi Trigger Resist for Electron Beam Lithography, **Carmen Popescu**, A. McClelland, G. Dawson, J. Roth, D. Kazazis, Y. Ekinci, W. Theis, A.P.G. Robinson, Proceedings SPIE, 104466 (2017).

Multi-trigger resist for electron beam and extreme ultraviolet lithography, **Carmen Popescu**, A. McClelland, D. Kazazis, G. Dawson, J. Roth, Y. Ekinci, W. Theis, A. P. G. Robinson Proc. SPIE 10775, 1077502 (2018).

High-Resolution EUV Lithography using a Multi-Trigger Resist, **Carmen Popescu**, D. Kazazis, A. McClelland, G. Dawson, J. Roth, W. Theis, Y. Ekinci, A.P.G. Robinson, Proc SPIE 10583 (2018).

Sensitivity Enhancement of the High-Resolution xMT Multi-Trigger Resist for EUV Lithography, **Carmen Popescu**, A. Frommhold, A. McClelland, J. Roth, Y. Ekinci, A.P.G. Robinson, Proceedings SPIE, 10143 (2017).

Multi-Trigger Resist Patterning with ASML NXE3300 EUV Scanner, Yannick Vesters, A. McClelland, D. De Simone, **C. Popescu**, G. Dawson, J. Roth, W. Theis, G. Vandenberghe, A.P. Robinson, Proceedings SPIE (2018).

Contents

Abstract **i**

Acknowledgements **iv**

List of Publications **v**

List of Figures **ix**

List of Tables **xvi**

Abbreviations **xvii**

1 Introduction **1**

1.1 Literature Review 2
1.2 Lithography Background 3
1.3 Types of Lithography 7
1.3.1 UV Lithography 8
1.3.2 DUV Lithography 11
1.3.3 EUV Lithography 12
1.3.4 Electron beam Lithography 17
1.3.5 Ion Beam Lithography 22
1.4 Resist materials 23
1.4.1 Important Properties 23
1.4.1.1 Sensitivity and Contrast 24
1.4.1.2 Resolution 24
1.4.1.3 Line Edge Roughness and Line Width Roughness . 25
1.4.2 Resist Materials Evolution 27
1.4.3 Chemically Amplified Resists 28
1.4.4 Non-Chemically Amplified Resists 33
1.5 Pattern Collapse 36
1.5.1 Silanes as Adhesion Promoters 40

1.6 Overview of Lithography Techniques 44
1.7 Thesis Outline 45

2 Experimental Techniques and Methods 46
2.1 Materials used 46
2.2 Electron Beam Lithography 47
2.3 EUV Lithography 49
2.4 Image Analysis Using SUMMIT 52
2.5 Sample Preparation for Lithography 54
2.6 Silane Deposition Methods 55
2.7 Contact Angle Microscopy 57
2.8 Surface Profiler 60
2.9 FTIR (Fourier Transform Infrared Spectrometry) 61

3 xMT Negative Tone Molecular Resist System 63
3.1 xMT 63
3.2 Formulation Optimisation Experiments 67
3.3 Enhanced xMT: EX2 and EX3 72
3.4 Metal Hybrids 77
3.5 Metal Ion Removed Resist 86
3.6 Organic High-Z Compounds for Increased Optical Density 90
3.7 Organic High-Z Cross-linker 95
3.7.1 Iodinated Cross-linker 96
3.8 Overview 99
3.9 Conclusions 99

4 Multi-trigger Resist 103
4.1 Mechanism 103
4.2 Optimised Component Ratio 105
4.3 Quencher Effect on Resist Stochastics 112
4.4 Conclusions 115

5 Achieving Ultimate Resolution 117
5.1 Post Exposure Bake Variation 117
5.2 Resist Film Thickness Variation 120
5.3 Pattern Collapse Mitigation. Active Underlayers 122
5.3.1 Contact Angle Measurements 123
5.3.2 Lithography on Silanized Substrates 128
5.3.3 Mechanical Stress on Lithographic Features 131
5.4 UV Assisted and Active Rinse 143
5.5 Conclusions 146

6 Final Conclusions and Future Work 149

A Higher magnification-SuMMIT analysis **153**

B Method used to calculate the efficiency of epoxide cross-linking from IR spectra **155**

Bibliography **159**

List of Figures

1.1 Moore's Law representation from [10] . . . 4
1.2 Schematic of a standard lithographic process. The left side shows a positive tone resist that becomes more soluble in developer when absorbing energy and the right side shows a negative tone resist in which the solubility decreases when energy is transferred to its constituent molecules. . . . 5
1.3 Modes in UV lithography, from [13] . . . 8
1.4 Interaction of light with the mask in UV photolithography, from [14] 9
1.5 Illustration of resolution defined as the minimum separation between two objects that can be seen as well defined separate images, from [14] . . . 10
1.6 Schematics of multilayer stack. Relatively high reflectivity is achieved from cumulative reflection at all interfaces . . . 14
1.7 Interactions in the EUV exposure mechanism, from [27] . . . 15
1.8 Photoionization produced by EUV photons. From [28] . . . 16
1.9 Inter-Coulombic decay (ICD). (A) A^{*++} - doubly charged ion in metastable excited state after Auger relaxation. Residual internal energy is not sufficient for intra-atomic Auger process. (B) Energy is transferred from A^{*++} to neighbouring B, creating a B^{+} ion. From [33] . . . 17
1.10 Schematic diagram of the interactions of the electron beam with the atoms in the resist . . . 18
1.11 Monte Carlo simulation of electron trajectories in polystyrene. Incident electron energies from 1 keV to 20 keV, from [36] . . . 20
1.12 Distribution of electrons in the resist film during exposure with electron beam with acceleration voltages of 10 keV, 25 keV and 50 keV, adapted after [38] . . . 21
1.13 Example of sensitivity curves for positive and negative tone resist . 24
1.14 Representation of pitch size and feature size or critical dimension . 25
1.15 Representation of LER and LWR . . . 26
1.16 Acid-catalyzed deprotection mechanism for polarity change in poly(4-tert-butoxycarbonyloxystyrene) resist, from [57] . . . 29
1.17 Acid catalyzed cross-linking mechanism in epoxy-based resists, from [57] . . . 31

1.18 Schematic representation of chemical amplification and close up on the acid diffusion at the edges of the features from [59] 32
1.19 SEM images of isolated lines on fMAPDST-MMA resist at pitch 100 nm, line width 20 nm, dose 40 μC/cm^2 from [66] 33
1.20 SEM image of lines patterned with EBL on C_{60}-PCMS-PHS resist from [70] 34
1.21 SEM images of single pixel lines on fullerene based resist at pitch 48 nm (left) and 46 nm (right). Measured LWR on these features is 4.5 nm for the 48 nm pitch and 3.4 nm for the 46 nm pitch from [71] 35
1.22 Schematic representation of resinous HSQ, from [74] 36
1.23 SEM images of left: stable, centre: collapsed, and right: super-collapsed pure PMMA nanostructures from [81] 37
1.24 Schematics of the action of the two forces involved in the adhesion failure model of pattern collapse in resists features after development 38
1.25 General chemical structure of a silane molecule. R can be an aryl, alkyl or organofunctional group and OR' can be a methoxy or an ethoxy group 41
1.26 Diagram of silanes chemistry, from [91] 42
1.27 Summary of lithographic techniques with corresponding resist materials and their describing lithographic parameters [96–98], [66], [69–71],[77] [99, 100] 44

2.1 Diagram of electron beam lithography tool 48
2.2 Diagram of electron beam pattern 49
2.3 Schematics of the EUV Interference Lithography from [101] 50
2.4 left: Design of the mask used for the EUV-IL experiment; right: SEM image of one of the 16 fields exposed on the resist using this mask 51
2.5 Summit analysis results from lines and pillars. PSD curve shown is obtained from the SEM image of the lines 53
2.6 Methods of silane deposition: 1. immersion, 2. spin coating, 3. vapour priming 57
2.7 Young's contact angle (static contact angle) at mechanical equilibrium of surface tensions of the three phases - solid, liquid and vapour 58
2.8 Illustration of dynamic contact angle technique 59
2.9 Theoretical plot of hysteresis curve between advancing and receding contact angle 59
2.10 Diagram of surface profiler 60

3.1 Chemical structure of components in the xMT baseline system . . . 65
3.2 IR spectra of the cross-linker and PAG formulated in 2:1 ratio. blue line - no treatment applied, red line - UV exposed for 15 minutes and green line - UV exposed and post exposure bake applied for 1 minute at 90 ° C 66

3.3 SEM image of xMT resist formulation patterned with 30 kV electron beam. Dose is 176.89 pC/cm^2, pitch size 44 nm, CD 15.6 ± 0.04 nm, LER 3.3 ± 0.07 nm . . . 68
3.4 SEM images of xMT resist formulations at standard (left) and high resin ratio (right) with 2.5% quencher added . . . 69
3.5 SEM images of xMT resist formulations at standard resin ratio with 2.5% quencher (left) and high resin ratio without quencher (right) . 69
3.6 SEM images of xMT resist formulations at standard and high resin ratio with 3% quencher added. . . . 70
3.7 SEM images of xMT resist formulations : standard and high resin ratio with 3% quencher added. . . . 71
3.8 SEM images of xMT resist standard and high resin formulations with 3% quencher added.CD in this case is the size of the non-exposed hole in between the patterned grating . . . 72
3.9 Chemical structure of the enhanced xMT resin. Top left: xMT molecule; top right: EX2 synthesised with a double bond on the chain to increase its mechanical strength; bottom: EX3 contains the double bond and two more t-BOC groups for improved cross-linking capability . . . 73
3.10 SEM images of dense lines at 32 nm pitch size patterned with EUV-IL on xMT, EX2 and EX3 resist formulations. . . . 74
3.11 SEM images of pillars on 50 nm and 60 nm pitch patterned with EBL at 100 kV on xMT, EX2 and EX3 resist formulations. Dose is 515 $\mu C/cm^2$. . . . 75
3.12 Atomic absorption cross-section as a function of the atomic number of the element, from [124] . . . 77
3.13 SEM images of dense lines at 32 nm pitch size patterned in EUV-IL on xMT resist standard formulation (left) and metal complex added formulation . . . 78
3.14 SEM images of dense lines at 32 nm pitch size patterned in EUV-IL on EX3 resist standard formulation (left), and metal complex added formulation (right) . . . 79
3.15 Comparison of dose required by xMT and EX3 and the metal hybrids to pattern 32 nm pitch dense lines with EUV and LER value obtained . . . 79
3.16 SEM images of dense lines at 32 nm pitch size patterned in EUV-IL on EX2 + 2.5% quencher resist formulation (left), and metal complex added formulation (right) . . . 80
3.17 SEM images of dense lines at 32 nm pitch size patterned in EUV-IL on EX2 + 3% quencher resist formulation (left), and metal complex added formulation (right) . . . 80
3.18 Dose and LER for 32 nm pitch size on EX2 + 3% quencher resist formulation and metal complex added formulations . . . 81
3.19 SEM images of dense lines at 32 nm pitch patterned on MIR EX3 resit formulation with 3% Q (left) and 2% SnI_2 added (right) . . . 82

3.20 SEM images of pillars at 50 nm pitch patterned with EBL on xMT and EX3 resit formulation with 3% quencher and with 2% SnI_2 added. Dose is 350 μC/cm^2 . . . 83
3.21 SEM images of dense lines at 32 nm pitch patterned with EBL on xMT and EX3 resit formulations with 3% quencher and with 2% SnI_2 added. . . . 84
3.22 SEM images of lines and ellbows patterned with EBL on xMT and EX3 resit formulation with 3% Q and with 2% SnI_2 added. . . . 85
3.23 Example of metal levels detected before and after metal ion removal purification process . . . 87
3.24 SEM images of dense lines at 32 nm pitch size patterned in EUV-IL on non-MIR and MIR xMT formulation . . . 88
3.25 SEM images of dense lines at 32 nm pitch size patterned in EUV-IL on non-MIR and MIR EX2 formulation . . . 88
3.26 SEM images of dense lines at 32 nm pitch size patterned in EUV-IL on non-MIR (left) and MIR EX3 (right) formulations . . . 89
3.27 SEM images of dense lines at 32 nm pitch size patterned in EUV-IL on standard formulation of MIR EX2 resist and formulations containing C_6H_5I in various concentrations. (1) - number of iodine atoms from C_6H_5I match the number of iodine atoms added in metal hybrid formulation; (2) - number of iodine atoms from C_6H_5I match the number of iodine atoms plus the number of tin atoms added in metal hybrid formulation; (3) the number of C_6H_5I molecules match the number of SnI_2 molecules . . . 91
3.28 SEM images of dense lines at 32nm pitch size patterned in EUV-IL on MIR EX3 resist and formulations containing C_6H_5I in various concentrations. (1) - number of iodine atoms from C_6H_5I match the number of iodine atoms added in metal hybrid formulation; (2) - number of iodine atoms from C_6H_5I match the number of iodine atoms plus the number of tin atoms added in the metal hybrid formulation . . . 93
3.29 Chemical structure of high opacity iodinated CL molecule synthesised with 6 iodine atoms to increase its opacity and the sensitivity of the resist material . . . 95
3.30 SEM images of 32 nm pitch (left) and 28 nm pitch (right) dense lines patterned with EUV-IL on resist formulation with the ICL . . 96
3.31 SEM images of 32 nm pitch (left) and 28 nm pitch (right) dense lines patterned with EUV-IL on resist with ICL in optimised formulation 97
3.32 CD as a function of dose measured on dense lines patterned with EUV-IL on resist formulations with the iodinated CL. Red - standard formulation by weight; Blue - optimised formulation for number of molecules of each component in the resist system . . . 97

3.33 LER as a function of critical dimension on dense lines patterned with EUV-IL on resist formulations with the iodinated CL. Red - standard formulation by weight; Blue - optimised formulation for number of molecules of each component in the resist system 98
3.34 Summary of lithographic performance improvements and disadvantages in various resist systems tested in this chapter 99

4.1 Schematics of the MTR mechanism 104
4.2 MTR standard formulation (left) and high resin ratio (right) from [126] 105
4.3 Critical dimension patterned as a function of dose when increasing the MTR ratio in MTR2 106
4.4 Critical dimension patterned as a function of dose when increasing the MTR ratio in MTR3 107
4.5 Dense lines at 36 nm pitch patterned with EBL on MTR2 formulations at standard and higher resin ratios 108
4.6 Dense lines at 36 nm pitch patterned with EBL on MTR3 formulations with standard and higher resin ration 109
4.7 Sparse lines patterned with EBL at 28 nm pitch on MTR3 formulations with standard and higher resin ratio 110
4.8 Sparse lines patterned with EBL at 36 nm pitch on MTR3 formulations at standard and higher resin ratio 111
4.9 Contribution of quencher to total LER value in EUV lithography, from [129] 113
4.10 Effect of quencher level on the dose and LER of features patterned on MTR3 resist formulations with various MTR ratios 113

5.1 LER measured on xMT, EX2 and EX3 resist samples that have been treated with post-exposure bake at 90 °C for 1 min and samples that have not received post-exposure bake 118
5.2 CD and LER measured on MIR MTR3 resist samples that have been treated with post-exposure bake at temperatures between 20 °C to 90 °C for 1 min 119
5.3 SEM images of lines patterned at 32 nm pitch on MIR MTR3 resist samples that have been treated with post-exposure bake. left: 20 °C, center: 60 °C, right: 90 °C for 1 min 120
5.4 Dose required to pattern pitches 32 and 28 nm at different thicknesses of the resist. LER measured at various thicknesses for 32 and 28 nm pitch size 121
5.5 Scheme of the silanization and lithography process 122
5.6 Water droplet on bare (left), hydroxylated (center) and silanized (right) silicon. The change in shape of the droplet demonstrates surface modification. The hydroxylated silicon is very hydrophobic, therefore the contact angle was very small (~ 5 °) and not easily detected by the software at the moment when the image was taken 123

5.7 Dynamic contact angle measurements on differently treated Si substrates. The change in the wetting behaviour of the substrate demonstrates surface modification . . . 124
5.8 Dynamic contact angle variation with the immersion time . . . 125
5.9 Hysteresis of the dynamic contact angle of the silanized Si substrate for (a) 1 h, (b) 2 h, (c) 3 h and (d) 4 h immersion in the TEVS solution. The highly inhomogeneous layer can be seen after 4 h . . . 126
5.10 Dynamic contact angle for the silanized substrates, where the silane was deposited through immersion (imm), spin coating (sp c) and vapour priming (vap prim). Immersion and vapour priming methods result in the most hydrophobic surfaces . . . 127
5.11 Comparison of the dynamic contact angle measured on silanes deposited on silicon substrate; Amino propyl triethoxy silane, triethoxy vinyl silane, 3-(ethoxydimethylsilyl) propyl-amine and 3-glycidyloxypropyl (dimethoxy) methylsilane . . . 128
5.12 SEM images of 36 nm pitch dense lines patterned with EUV-IL on control sample - bare Si substrate, silane UL (immersion), silane UL (spin coating), silane UL (vapour priming) . . . 129
5.13 SEM images of 36 nm pitch dense lines patterned with EUV-IL on resist coated from cyclohexanone and PGMEA on top of TEVS and APTES UL . . . 130
5.14 Pattern designed for EBL exposures with lines at different pitch sizes separated by various spacings in order to introduce different capillary forces during rinsing . . . 131
5.15 SEM images of 40 nm pitch lines patterned with EUV-IL on resist on top of silane UL . . . 132
5.16 SEM images of various CDs at various pitch sizes patterned with EBL on 28 nm film thickness of resist on top of APTES UL . . . 134
5.17 SEM images of various CDs at various pitch sizes patterned with EBL on 28 nm film thickness of resist on top of TEVS UL . . . 135
5.18 SEM images of various CDs at various pitch sizes patterned with EBL on 28 nm film thickness of resist on top of EDMSPA UL . . . 136
5.19 SEM images of various CDs at various pitch sizes patterned with EBL on 28 nm film thickness of resist on top of GPDEMS UL . . . 137
5.20 SEM images of various CDs at various pitch sizes patterned with EBL on 34 nm film thickness of resist on top of TEVS UL . . . 138
5.21 SEM images of various CDs at various pitch sizes patterned with EBL on 34 nm film thickness of resist on top of EDMSPA UL . . . 139
5.22 Mechanical stress in features patterned on 28 nm and 34 nm resist thickness on different silane underlayers . . . 140
5.23 Mechanical stress in features patterned on 28 nm and 34 nm resist thickness on different silane underlayers at the collapse point . . . 141
5.24 Mechanical stress and inner spacing (S_1) for 19 nm features patterned on 28 nm resist thickness on different silane underlayers at the collapse point . . . 141

5.25 Measured CD of lines patterned at the same dose on the same resist at designed hp of 16 nm, 20 nm and 30 nm on different underlayers 142
5.26 Line edge roughness and CD as a function of dose measured after rinse in standard rinse liquid, UV assisted rinse 144
5.27 Line width as a function of dose measured after rinse in standard rinse liquid and acid additive rinse 145
5.28 LER as a function of dose measured after rinse in standard rinse liquid, and acid additive rinse 146

A.1 Summit analysis results from lines imaged at 300k and 400k magnifications 153

B.1 Aromatic C-C stretch IR peak in formulations of cross-linker and photoacid generator: a) after drop casting, b) after 15 minutes exposure to UV light, c) exposed to UV for 15 minutes and received PEB 156
B.2 Epoxide IR peak in formulations of cross-linker and photoacid generator: a) after drop casting, b) after 15 minutes exposure to UV light, c) exposed to UV for 15 minutes and received PEB 157
B.3 IR complete spectra of formulations of cross-linker and photoacid generator: a) after drop casting, b) after 15 minutes exposure to UV light, c) exposed to UV for 15 minutes and received PEB 158

List of Tables

3.1 Conversion rate of epoxy groups in the CL+PAG, CL+PAG+UV and CL+PAG+UV+PEB samples as calculated from the IR spectra 67
3.2 Dose, CD and LER of 32 nm pitch dense lines patterned on xMT, EX2 and EX3 with EUV-IL 74
3.3 Diameter (ϕ), LER and Eccentricity of pillars at 50 nm and 60 nm pitch patterned on xMT, EX2 and EX3 with EBL 76
3.4 Dose, CD and LER of lines at 36 nm pitch patterned on xMT, EX3 and corresponding metal hybrid formulations with EBL 85
3.5 MIR vs non-MIR formulations - Change in Sensitivity and LER . . 89
3.6 Dose required to pattern dense lines at 32 nm pitch size and LER obtained in EUV using MIR EX2 + C_6H_5I. (1) - number of iodine atoms from C_6H_5I match the number of iodine atoms added in metal hybrid formulation; (2) - number of iodine atoms from C_6H_5I match the number of iodine atoms plus the number of tin atoms added in metal hybrid formulation; (3) the number of C_6H_5I molecules match the number of SnI_2 molecules 92
3.7 Dose required to pattern dense lines at 32 nm pitch size and LER obtained in EUV using MIR EX3 + C_6H_5I. (1) - number of iodine atoms from C_6H_5I match the number of iodine atoms added in metal hybrid formulation; (2) - number of iodine atoms from C_6H_5I match the number of iodine atoms plus the number of tin atoms added in the metal hybrid formulation 93
3.8 Change in sensitivity and LER in MIR EX2 and MIR EX3 when C_6H_5I is added to the resist formulation compared to the control samples 94

4.1 Dose and LER for four different MTR ratios in MTR2 and MTR3 evaluated with EUV-IL 108
4.2 Dose and LER for three different MTR component ratios in MTR2 and MTR3 evaluated with EBL 111

Abbreviations

AFM	**A**tomic **F**orce **M**icroscopy
APTES	**A**mino**p**ropyl **T**ri**e**thoxy **S**ilane
CAR	**C**hemically **A**mplified **R**esist
CD	**C**ritical **D**imension
CL	**C**ross **L**inker
DNQ	**D**iazo**N**aphto**Q**uinone
DPP	**D**ischarge **P**roduced **Palsma**
DRAM	**D**ynamic **R**andom **A**ccess **M**emory
DUV	**D**eep **U**ltra **V**iolet
EBL	**E**lectron **B**eam **L**ithography
EDMSPA	3-(**E**thoxy**dim**ethyl**s**ilyl)**p**ropyl-**a**mine
EUV	**E**xtreme **U**ltra **V**iolet
EUV-IL	**E**xtreme **U**ltraviolet **I**nterference **L**ithography
GPDEMS	3-**g**lycidyloxy**p**ropyl (**d**im**e**thoxy) **m**ethyl**s**ilane
HMDS	**H**exa **M**ethyl **Dis**ilazane
HP	**H**alf **P**itch
HSQ	**H**ydrogen **s**ilses**q**uioxane
ICD	**I**nter - **C**oulombic **D**ecay
IRDS	**I**nternational **R**oadmap for **D**evices and **S**ystems
LER	**L**ine **E**dge **R**oughness
LPP	**L**aser **P**roduced **Plasma**

LWR **L**ine **W**idth **R**oughness

MAPDST (4-**m**eth**a**cryloyloxy) **p**henyl) **d**imethyl**s**ulfonium **t**riflate

MEMS **M**icroelectromecanical **S**ystems

MIR **M**etal **I**on **R**emoval

MMA **M**ethyl **M**eth**a**crylate

MTR **M**ulti **T**rigger **R**esist

NA **N**umerical **A**perture

n-CAR **n**on - **C**hemicaly **A**mplified **R**esist

PAB **P**ost **A**pplication **B**ake

PAC **P**hoto**A**ctive **C**ompound

PAG **P**hoto **A**cid **G**enerator

PBOCST **P**oly (4-tert-**b**ut**o**xy**c**arbonyloxy**s**tyrene)

PEB **P**ost **E**xposure **B**ake

PHOST **P**oly(4 - **h**ydr**o**xy**s**tyrene)

PHS **P**oly **H**ydroxy**s**tyrene

PMMA **P**oly(**M**ethyl **M**eth**A**crylate)

PSD **P**ower **S**pectral **D**ensity

RLS **R**esolution, **L**ine Edge Roughness and **S**ensitivity

SEM **S**canning **E**lectron **M**icroscopy

SiUL **Si**lane **U**nder**l**ayer

SPL **S**canning **P**robe **L**ithography

SPM **S**canning **P**robe **M**icroscopy

STM **S**canning **T**unneling **M**icroscopy

tBOC **t**ert**B**ut**O**xy**C**arbonyl

TEVS **T**ri**e**thoxy **V**inyl **S**ilane

UV **U**ltraviolet

Chapter 1

Introduction

Nanotechnology finds its roots in 1959 at the American Physical Society meeting in Richard's Feynman talk entitled "There is plenty of room at the bottom: an invitation to enter a new field of physics" [1]. This anticipated a large range of now well established fields such as quantum electronics, projection electron microscopy, electron and ion beam fabrication and microelectromecanical systems (MEMS). An unrealistic idea at that time but one which is successfully achieved in 1985 by Tom Newman [2] when writing the first page of "A tale of two cities" by Charles Dickens reduced in size by 25000 times, with each character measuring 50 nm width, using an electron beam lithography (EBL) tool. Since then the development of micro- and nanothechnologies has seen very high interest with the main goal being to fabricate and use structures, devices and systems that have unique functionality due to their small size.

There are two different approaches in nanofabrication; the first approach is "top-down" and it progressively reduces the dimensions of the fabricated structures. The fabrication process goes from large to small scale using carving or etching to create nanostructured devices from larger materials. Top-down is the workhorse

of the semiconductor industry. This approach includes techniques such as electron beam lithography, photolithography and nanoimprint lithography. There are chemical top-down techniques developed as well as reported by [3]. These include templated etching, selective dealloying, anisotropic dissolution and thermal decomposition. The main advantage of top-down techniques is the high level of control of the process, but they can be slow, can require expensive and complex equipment and processes and typically have a limit on ultimate resolution of 10 nm or more.

The second approach is “bottom-up” and in this case the nanostructures are being assembled out of smaller blocks. This technique includes carbon nanotubes synthesis and molecular self assembly. In this thesis I will show the results obtained using top-down techniques specifically e-beam and EUV lithography. This type of techniques are fast and low cost but the level of controlling the process is also very low. The other disadvantage is the non-uniformity of the structures created at a large scale. Nanofabrication processes are used in a large number of fields such as chemistry [4], opto-electronics, micro-electronics [5, 6] and even biology [7]. However, the primary economic driver for progress in nanofabrication processes is the ever-increasing desire for faster computers, high-volume data storage and processing [8].

1.1 Literature Review

In this chapter I will introduce the process of lithography by presenting a brief history and describing the main types of lithography. I will then talk about the main laws driving the constant evolution of lithography, and the materials used in this process. Further I will review some of the most common resist materials and present their advantages and disadvantages with regards to optimization for next generation lithography processes.

This chapter also describes the basic metrics required to describe the performance of a given resist material. This includes discussion of important parameters involved in the characterization of a resist material such as sensitivity, contrast, line edge roughness and line width roughness.

In order to fully understand the behaviour of a specific material, the intrinsic properties of that material are important to know. In this study the most important of these properties is the mechanical strength of the resist material, which plays a pivotal role in pattern collapse. Investigating and improving the mechanical strength of the resist material enables pattern collapse mitigation, reduction in line width roughness and reduction in pattern defectivity. All these phenomena have a tremendous effect on the final process of device microfabrication and their study is an important topic for advances in the semiconductor industry.

1.2 Lithography Background

The word “lithography” comes from greek *“lithos”* - stone and *“graphia”* - to write. As the name suggests, lithography is a method used to produce patterns or three-dimensional structures on a substrate. The structures are transferred onto the substrate via direct writing as is the case in electron beam lithography or projected through a mask as is the case in photolithography (lithography that uses light).

The concept of lithography has been around for more than 200 years. It was first discovered in 1798 by Alois Senefelder but only became popular in 1820 [9]. Senefeder was a playwrigth and in 1798 he discovered an interesting process. His ink was a mixture of soap, wax and lampblack and his writing surface was polished limestone. After writing on the stones he was covering them with an acid solution and he noticed that only in the areas where he hadn’t written the limestone was

etched away. Then he noticed that he could transfer the writing from the stone onto paper by simply and carefully covering the surface of the stone with a layer of ink and press the stone against the paper. This was the first lithographic press ever built. Prints of local views and illustrated bills could be rapidly and cheaply produced through lithography. Originally lithography used stone as the printing surface but the Bavarian limestone most suited to production was eventually replaced by zinc (from 1830) and later aluminium (from 1890) [9].

The term is most associated today with the semiconductor industry, specifically for device microfabrication. The goal of lithography is to project a designed pattern onto a suitably sensitive resist film to form a mask that can then be transferred in the underlying substrate, which is most often a semiconducting silicon wafer. The patterned silicon wafer offers the base for the integrated circuit manufacturing process.

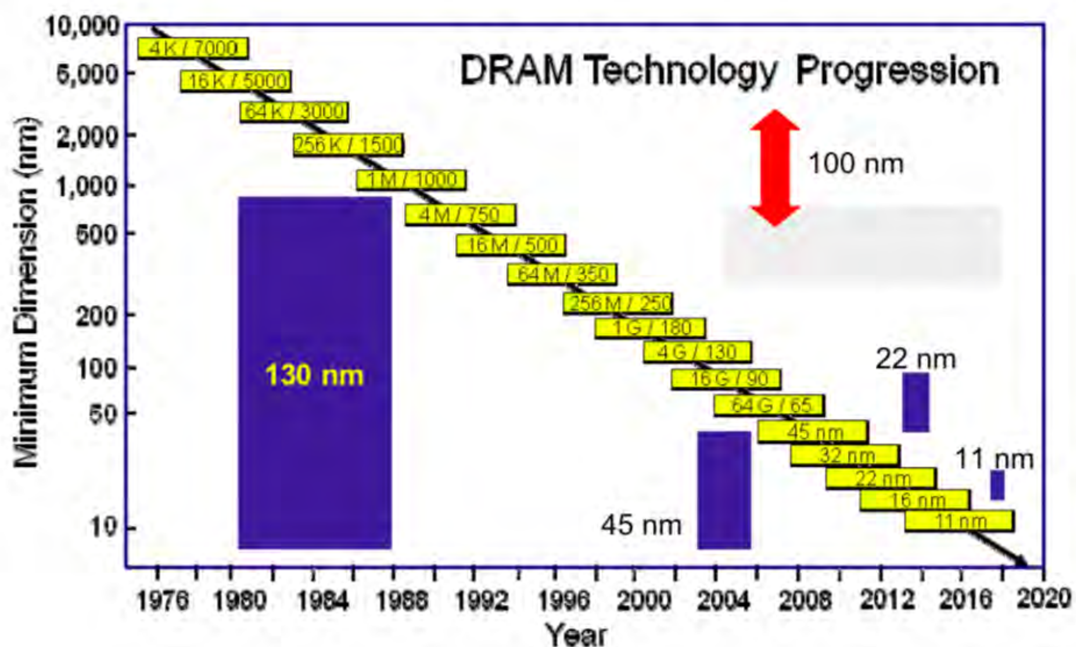

FIGURE 1.1: Moore's Law representation from [10]

Technological progress constantly challenges the lithographic process. Gordon Moore observed in 1960 that the number of transistors that could be fabricated on

a chip, of a given size, at an acceptable cost, doubled every year [11, 12]. The effect that this has on the electronics industry is that the power of computers significantly increases, as the cost goes down, at an exponential rate. This implies that progress in the semiconductor industry requires the packing of the transistors more tightly with every new generation of chips, scaling down the size of transistors.

The workhorse of lithography and the leading technique in the semiconductor industry has, for many years been, photolithography. Photolithography uses a beam of light projected through a mask to pattern the chip. The steps of a basic process of lithography are schematically illustrated in the figure 1.2.

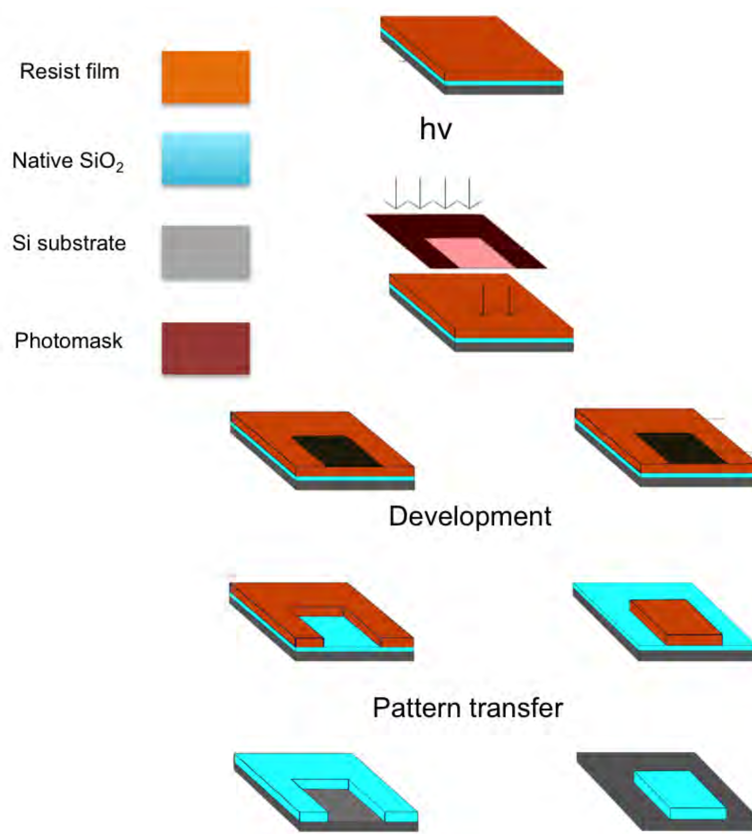

FIGURE 1.2: Schematic of a standard lithographic process. The left side shows a positive tone resist that becomes more soluble in developer when absorbing energy and the right side shows a negative tone resist in which the solubility decreases when energy is transferred to its constituent molecules.

The typical process flow is as follows. In the first step the Si substrate is cleaned using a ultrasonic bath of acetone and a second of isopropanol in order to remove

contaminants from the surface, which could otherwise lead to poor adhesion and defect formation in the resist film spun on top of the silicon surface. The next step is to spin coat the resist solution (a mixture of the radiation sensitive polymeric material dissolved in an appropriate casting solvent). Varying the solution concentration and/or the spin speed controls the thickness of the resist film. After resist coating the sample is baked (post application bake, PAB) in order to evaporate the excess solvent and to eliminate residual stress built up in the resist during the spinning process. The resist film is then exposed to radiation through a mask in photo- and X-ray lithography or directly to finely focused electron beams in electron beam lithography. Exposure of the resist to a specific radiation source causes chemical changes in the exposed area by selectively altering the solubility of the exposed areas compared to the unexposed areas in the developing solvent. After exposure the sample may be baked again (post exposure bake, PEB) to trigger further chemical changes in the exposed or unexposed areas. In the next step the sample is developed by spray, puddle or immersion in an appropriate solvent. If the unexposed areas of the resist are removed from the silicon substrate after developing process, the resist has a negative tone; otherwise the resist has a positive tone. The pattern obtained will then be transferred to the substrate by for instance etching or lift-off. The final step is to remove the resist structures from the substrate using a liquid stripping process or dry oxygen plasma etching.

Smaller transistors imply that the lithography tools have to be able to pattern smaller features. This can be achieved by using a source of light with a shorter wavelength, which allows the patterning of smaller features with good resolution. Therefore lithography has progressed from initially utilising UV light at 365 nm to deep UV light at 248 nm and then 193 nm. Current semiconductor manufacturing uses 193 nm wavelength to expose the photosensitive resist material. In order to enhance the resolution and downscale the feature size even more, immersion photolithography has been developed. In this method a liquid with a refractive index

higher than 1 is introduced between the final lens of the optical system in the exposure tool and the photoresist. Issues like water uptake and pattern degradation may occur in this case, therefore, an intermediate coating layer or a water resistant photoresist must be used. However this increases the complexity of the manufacturing process. Extreme ultraviolet lithography is the next step in the technology roadmap. It uses a radiation source with a 13.5 nm wavelength and employs a set of reflective lenses operating in a high vacuum environment. The light generated from the source is focused onto a reflecting mask creating two-dimensional patterns reflected from the mask onto the resist film. Another lithography method is electron beam lithography, which uses a finely focused electron beam to draw the designed pattern on the resist film. It has the benefit of not being limited by the diffraction phenomenon, and is thus one of the most promising techniques in terms of resolution capability. However, it has the disadvantage of low throughput, and is not suitable for industrial manufacturing at present but it is being heavily used for mask fabrication.

1.3 Types of Lithography

Depending on the type of radiation source used to expose the resist material there are different categories of lithography:

- **photolithography:** ultraviolet (UV), deep ultraviolet (DUV), and extreme ultraviolet (EUV)
- **electron beam lithography**
- **charged particle lithography:** ion beam lithography

1.3.1 UV Lithography

UV lithography is the most common technique used in lithography and although it is being replaced by next generation techniques for high resolution patterning it is still being used for large feature size patterning. The photons emitted by the source excite the resist molecules to a higher energy temporary state allowing for photochemically driven changes. The source is a mercury lamp and the strongest emission lines are used in this technique - 436 nm (g-line lithography), 405 nm (h-line lithography), and 365 nm (i-line lithography). There are three modes of UV lithography : proximity, contact and projection. A schematic of the tool configuration is shown below.

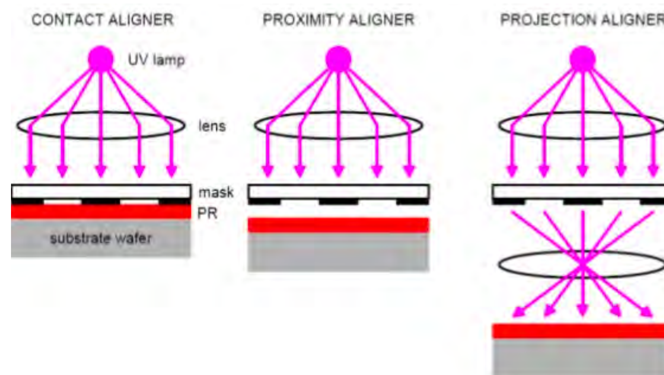

FIGURE 1.3: Modes in UV lithography, from [13]

The resolution of the features patterned decreases from the former to the latter.

When light interacts with the mask, the effects are different for each one of the 3 configurations.

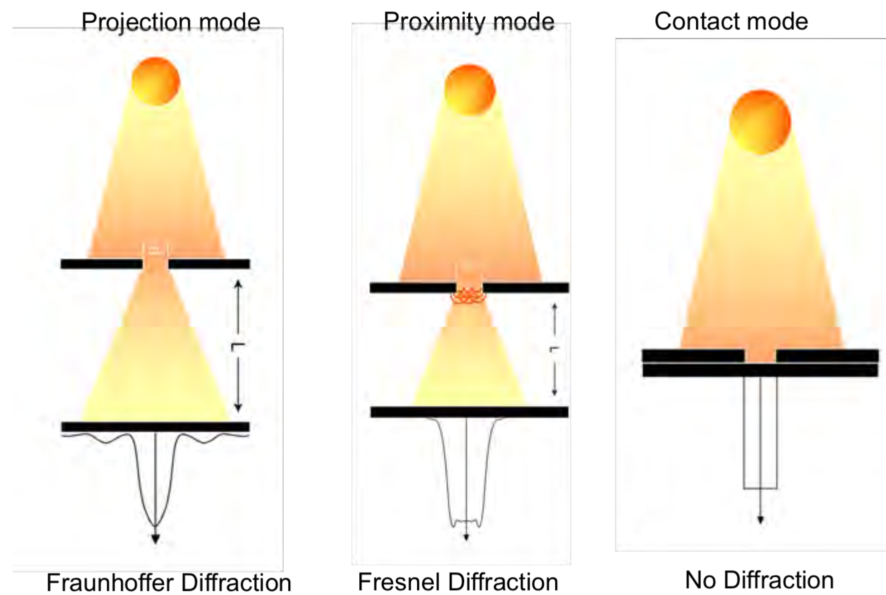

FIGURE 1.4: Interaction of light with the mask in UV photolithography, from [14]

Projection UV lithography uses a series of lenses that project the light through the mask and produce the image on the resist film. The features on the wafer can be reduced down to 4 times less than their size on the mask. This simplifies the mask production process [15] but the disadvantage is that the projection optics increases the complexity of the exposure tool. In projection mode, the distance between the mask and the resist surface is large enough ($L > d^2/\lambda$) to allow for Fraunhoffer diffraction events. If the distance between the mask and the resist sample is smaller than d^2/λ Fresnel diffraction events will take place instead. The difference between the two configurations have a major impact on the resolution that can be achieved with each technique. The lithographic resolution is diffraction limited in projection and proximity mode of UV photolithography. In order to discuss the lithographic resolution that can be achieved in UV lithography, Rayleigh criterion must be introduced. Rayleigh's criterion defines the minimum separation between two light sources that can be resolved as separate objects.

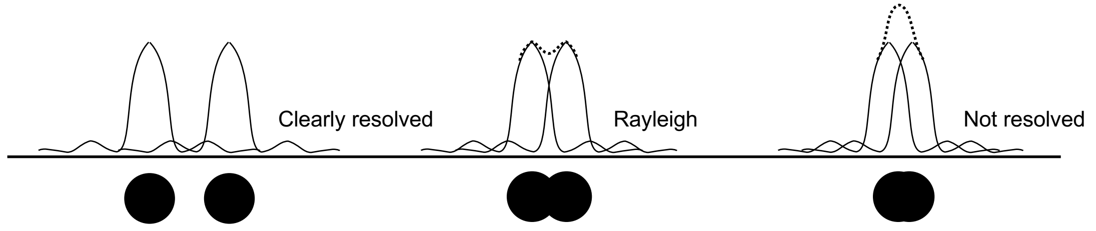

FIGURE 1.5: Illustration of resolution defined as the minimum separation between two objects that can be seen as well defined separate images, from [14]

In the case of projection mode UV photolithography the minimum resolvable separation depends on the focal length of the lens and is given by equation 1.1:

$$\Delta l_{min} = 1.22\frac{f\lambda}{d} \tag{1.1}$$

where f is the focal length of the lens and d is the feature diameter. Common practice is to use the numerical aperture of the lens system instead of the focal length.

$$NA = n_0 sin\alpha = \frac{D}{2f} \tag{1.2}$$

where D is the diameter of the aperture. Numerical aperture varies for each UV lithographic tool and can take values between 0.2 and 1 for non immersion systems.

Substituting the focal length with the NA in the minimum separation equation we obtain the resolution in projection UV photolithography as:

$$d_{min} = k_1\frac{\lambda}{NA} \tag{1.3}$$

where k_1 is a process parameter defined in equation 1.4 and can take values between 0.5 an 1 for typical UV tools but can be lower for advanced techniques with a theoretical limit of 0.25.

$$k_1 = \frac{D}{2\Delta l_{min}} \tag{1.4}$$

In proximity mode the mask is situated close to the surface of the wafer, therefore the resolution is limited by Fresnel diffraction events.

$$L \approx \frac{d_{min}^2}{\lambda} \tag{1.5}$$

$$d_{min}^2 = L\lambda \tag{1.6}$$

$$d_{min} = \sqrt{L\lambda} \tag{1.7}$$

where L is the gap between the mask and the wafer and λ is the wavelength of the exposure source.

The size of the features to be patterned are the same size on the mask.

In contact mode the mask lays on top of the resist coated wafer and the resolution is not diffraction limited and is comparable to the wavelength of the source. The only limiting factor for the resolution in this technique is the mask feature size. Contact often introduces defects in the resist film and increases the risk of damaging the mask.

1.3.2 DUV Lithography

Between 1980 and 1990, in order to increase the resolution in lithography, the wavelength of the source had to be decreased, as can be seen in equation 1.3. Therefore, the industry moved towards KrF excimer lasers with the wavelength of 248 nm. The DUV light is produced by the KrF gas plasma in a sealed chamber and emitted through a CaF_2 window.

Further optimisation of this technique introduced the 193 nm ArF lasers and most current industrial applications use 193 nm DUV lithography tools. Efforts have

been made to lower the wavelength even further but suitable optics for the sub-193 nm region are expensive and sensitive, therefore a move to 157 nm was not implemented in industry.

To increase the resolution further, NA can be increased by introducing a medium with a refractive index higher than air in between the projection lens and the resist coated wafer. This is known as immersion UV lithography and while it demonstrates improved resolution compared to traditional projection UV lithography it does increase the complexity of the tool and introduces a risk of damaging the resist and the mask just as in contact mode UV lithography.

1.3.3 EUV Lithography

In the last decade EUV has received most of the attention as the next generation lithography technique most likely to replace the currently industrially used-193 nm. The extreme ultraviolet wavelength band covers the wavelength range from 10 nm to 120 nm but the 11 –14 nm range is most used in lithography. According to equation 1.3 this should significantly improve the patterning resolution achieved by EUV tools. Sub 14 nm resolution [16], a world record of 7 nm lines in HSQ [17] and 12 nm resolution in CAR [18] was achieved using EUV lithography.

However EUV lithography is a challenging transition. Producing the photons with this wavelength is the first challenge in this technique. Unlike the DUV lithography, where corrosive gas is not an issue in the EUV tools separations windows are not an option, due to the fact that light at this wavelength is easily absorbed by all materials.

One way to produce EUV photons is using a synchrotron. This was first achieved by Solak et al. in 1990s with a Lloyds mirror interferometer setup [19]. The EUV light produced by the synchrotron could be passed through a monochromator and it was spatially and temporarily coherent enough to produce interference. The

EUV light produced a fringe pattern using incident light at a grazing angle, with a half pitch of 19 nm and it had the capability of changing the period of the fringes by adjusting the grazing angle. Synchrotron produced EUV light is very useful for research purposes [20] but the disadvantage of using this as a source in industrial application is the high cost of producing the specific bandwidth of radiation used in manufacturing [21].

An alternative way of producing EUV photons is via a laser-produced plasma (LPP) or discharge-produced-plasma (DPP). In LPP sources a pulsed laser is focused onto a target material and a plasma is produced. Upon recombination of electrons with highly energetic ions in the plasma, the EUV photons are produced [22]. The target material was initially Xe until a side phenomenon was observed —the highly charged Xe^{+10} ions were sputtering the target [23], producing contaminants that damaged the optics of the tool. Currently the target material used for LPP EUV sources is Sn, which was chosen for its high conversion efficiency to EUV light [24].

In DPP sources the plasma is generated by a high potential applied in between electrodes. The main drawback of this method is the low intensity of the light produced with these sources, meaning that they are not suitable for industrial applications. Moreover, DPP as well as LPP EUV sources produce a broad bandwidth of light, most of which is in DUV region and can unnecessarily expose the resist.

The second challenge of EUVL is that all materials absorb strongly at this wavelength, and therefore the EUV lithography tools have to operate in vacuum and use reflective optics instead of transmission optics. However, the reflectivity of materials at such short wavelengths is very low at near-normal angles of incidence. The solution to this problem came in 1980 when Barbee et. al. started to investigate the reflectivity of multilayer coatings [25] and showed practical efficiency at sub –15 nm wavelengths. Following this study it was possible to produce mirrors

which reflect between 60% and 70% of EUV light by using multilayers of materials with very different atomic numbers. Small reflectivity at each interface adds up to relatively high reflectivity when a sufficient number of layers is used and Bragg condition is met at near-normal incidence. Molybdenum and silicon layers are the most used materials to coat mirrors for EUVL. Using this type of mirrors renders an efficiency in the reflectivity of 2% for the entire system.

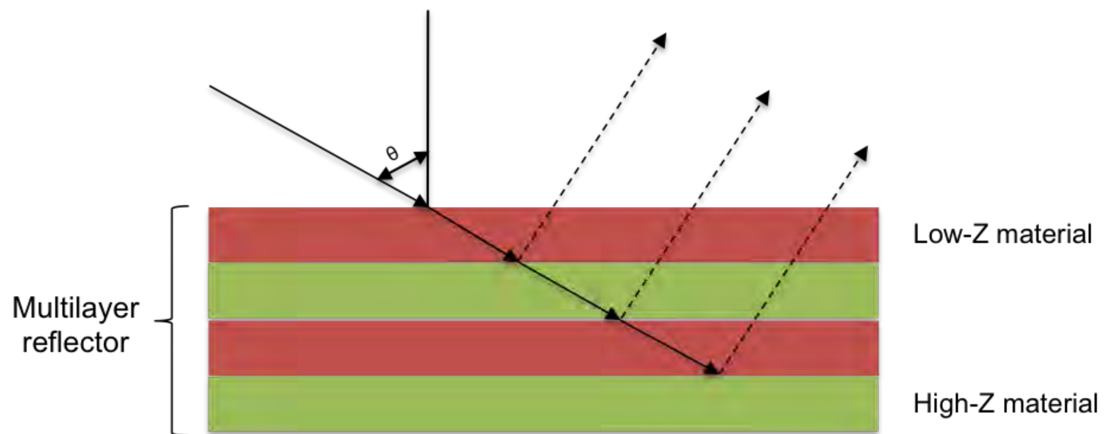

FIGURE 1.6: Schematics of multilayer stack. Relatively high reflectivity is achieved from cumulative reflection at all interfaces

One problem with the multilayers encountered in EUVL is the instability at high temperatures, where the Mo layers and Si layers start to intermix.

The other important issue that needs to be resolved in EUV tool is the contamination of the mirrors and masks through deposition of carbon generated during the exposure of resist materials [26]. This significantly affects the reflectivity of the mirrors and degrades the mask.

A further complication of the EUVL technique is the resist exposure mechanism and the physics and chemistry involved in EUV lithography, which is more complex than the well studied photolithographic process. A diagram of the current theoretical understanding of the process is sketched in figure 1.7 below.

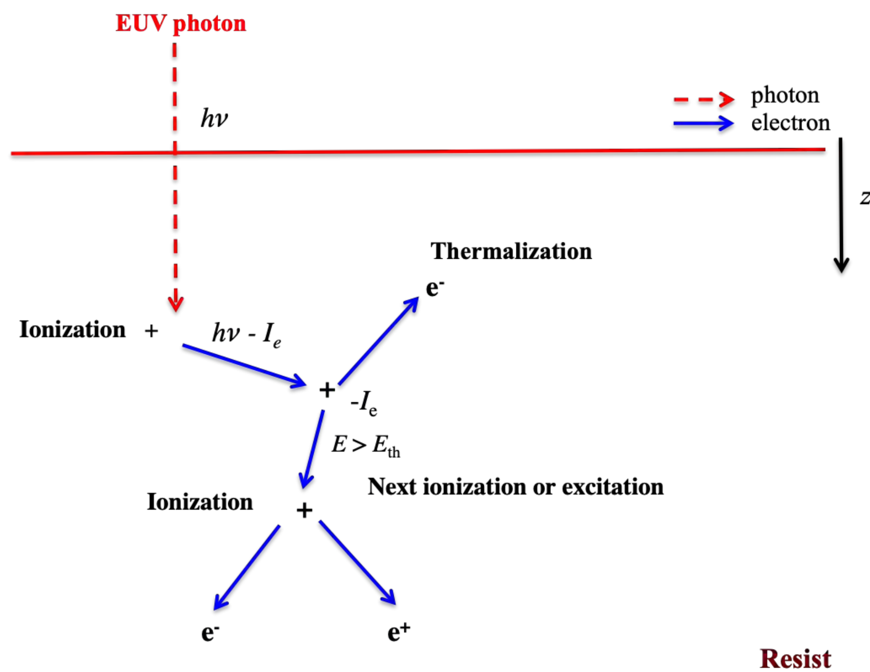

FIGURE 1.7: Interactions in the EUV exposure mechanism, from [27]

The energy of the incident photons is much higher in EUV, 92 eV as opposed to 6.4 eV in 193 nm lithography. Therefore, instead of exciting molecules and causing photochemistry, photons will ionise molecules generating photoelectrons upon absorption. The exposure mechanism then resembles the electron beam lithography mechanism with one difference —the relaxation processes have an important role in EUVL. At the interaction of the EUV photons with resist molecules, the 92 eV photon is absorbed with an electron being emitted and forming a stable ion with some residual internal energy. A very important aspect has to be considered in this discussion, the fact that the molecular or atomic orbitals that can be excited by EUV photons are the ones which are most strongly bound in the system, therefore the stable ion left behind after photo-absorption has a significant amount of residual internal energy. This is the reason why the relaxation processes are important in EUVL, since during this process additional secondary electrons generation can occur together with molecular fragmentation into radicals. Figure 1.8 presents the three steps in the excitation process at the interaction of EUV photons with resist

molecules.

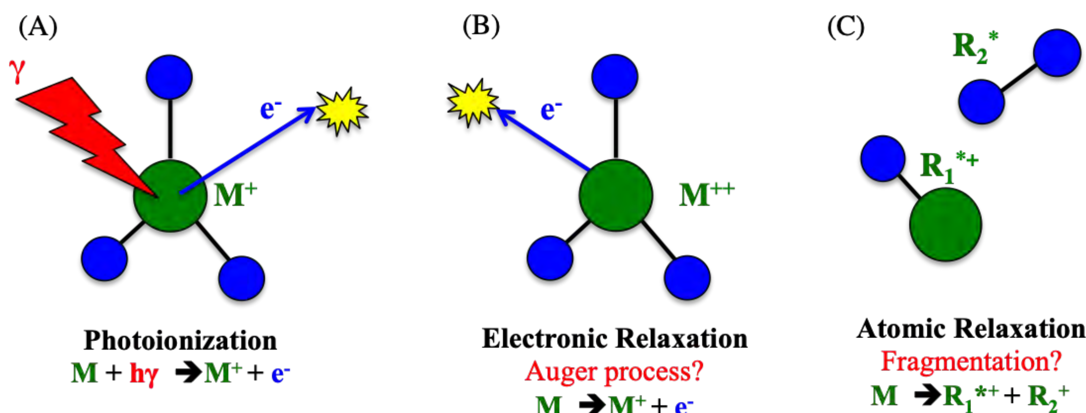

FIGURE 1.8: Photoionization produced by EUV photons. From [28]

In the first step the EUV photon is absorbed. Because the EUV photons can only excite the strongest bound molecular orbitals, the secondary electron being emitted will have low energy. In the second step the ionised molecule which has sufficient residual internal energy undergoes a process where the electrons are reorganising –in order to achieve minimum internal energy –with the emission of an additional secondary electron in an Auger process rendering a doubly ionised molecule (if energetically possible). In the last step the atoms reorganise changing their position in the molecule and fragmentation can occur if the molecule is doubly ionised or if the residual internal energy is sufficient for the process to occur. Radicals and radical ions are obtained.

The relaxation process of the excited molecules can be a quick process and depending on the residual internal energy the relaxation can be accompanied by the emission of one ore more secondary electrons, or it can be a slow process —fluorescence if Auger processes are not allowed. Intercoulombic decay, illustrated in 1.9 is also a process that can occur during relaxation of molecules in condensed films [29–31] and in this process the excited molecules can transfer their energy to their close neighbours. This is a non-radiative Coulomb interaction and it occurs when Auger process is not energetically favourable. Another process that can occur in

atomic relaxation was described by Stumpf et. al in [32]. It is an electron transfer mediated decay and it involves transferring energy and charge to neighbouring atoms.

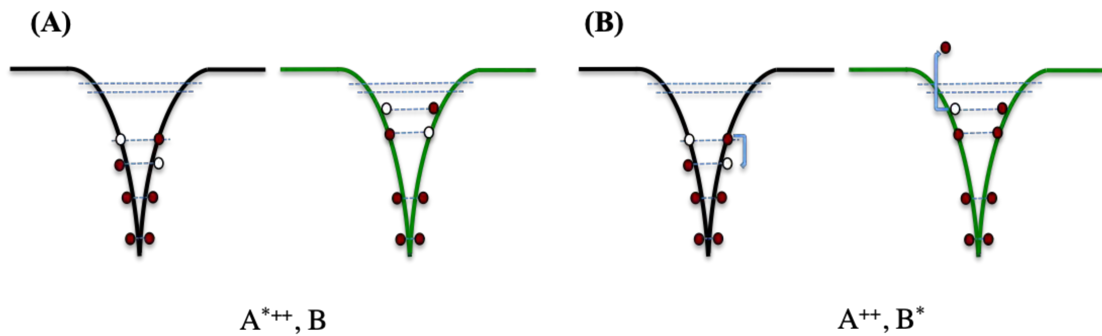

FIGURE 1.9: Inter-Coulombic decay (ICD). (A) A^{*++} - doubly charged ion in metastable excited state after Auger relaxation. Residual internal energy is not sufficient for intra-atomic Auger process. (B) Energy is transferred from A^{*++} to neighbouring B, creating a B^{+} ion. From [33]

Another issue that is raised in EUV lithography is the increasing level of stochastic phenomena and this is due to the lower number of photons absorbed by the resist material at a given dose.

1.3.4 Electron beam Lithography

Electron beam lithography is a mask-less lithographic technique, which is particularly utilised for creating extremely fine patterns. Using e-beam lithography features as small as 5 nm can be patterned. The method involves scanning a finely focused electron beam across the surface of the resist film depositing energy in a designed pattern. The beam is paused at chosen locations for the appropriate amount of time to deposit a certain amount of energy in that location. As the beam scans it also switches off and on to draw the shapes designed in the pattern.

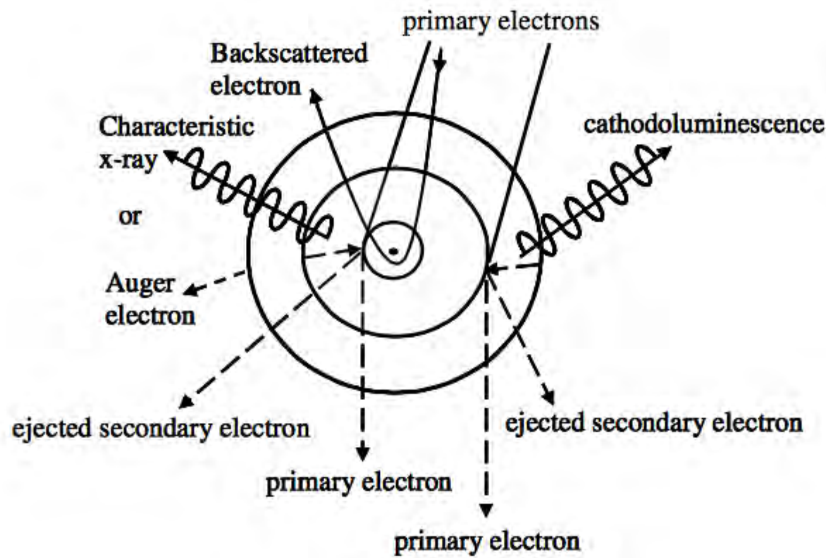

FIGURE 1.10: Schematic diagram of the interactions of the electron beam with the atoms in the resist

Figure 1.10 shows a sketch of the interactions that take place between the electron beam and the atoms in the resist. The primary electrons can be completely back-scattered after strong Columbic interaction with the nucleus. This interaction does not deposit energy in the resist film.

When primary electrons interact with electrons from inner shells of the atom the electrons can be removed if the energy of primary electrons is high enough. As a result, a vacancy will be formed in the inner shell, which is quickly filled by an electron from an outer shell, process which is accompanied by the emission of a photon, know as characteristic X-ray because its energy equals the difference between the energy of the shell its coming and the energy of the shell it ends up into.

Upon this rearranging of electrons, sometimes the difference in energy between the inner shell and the outer shell is not emitted as a photon but as an electron which is ejected from the atom and is known as an Auger electron. At high energies of the electron beam, photons at characteristic wavelengths can also be produced in a process known as cathodoluminescence.

There are two types of scattering events manifesting as the electron beam penetrates the resist material, which have an impact on the patterning process: forward scattering and backscattering. In forward scattering the electrons are deflected by a small angle from their initial trajectory following interactions with the atoms in the resist material. Forward scattered electrons will contribute to beam broadening, increasing the feature size in the resist pattern [34].

The backscattering process consists of electrons being scattered at much larger angles (some of them travelling back towards the surface of the resist) as they interact primarily in the substrate. The backscattered electrons are responsible for the proximity effect, which is when scattered electrons deposit energy in the areas that are supposed to remain unexposed in the resist film [35].

Incident electrons or backscattered electrons can undergo inelastic scattering processes in the resist film and create secondary electrons. The generation process of secondary electrons continues as the incident electrons travel in the resist film until the primary electrons lose their energy, which (in electron beam lithography) is between 5 and 100 keV. Secondary electrons with energies of 10—100 eV are responsible for most of the resist exposure process. They are also responsible for further beam diameter widening, as they can travel several nanometres in the resist film before interacting with a resist molecule.

In [36] Monte Carlo simulations were conducted to predict the trajectories of secondary electrons in a polystyrene film. The incident electron's energy were varied from 1 keV to 20 keV, and as can be seen in figure 1.11, the authors found that at energies below 5 keV forward scattering is significant and there are almost no electrons reaching the substrate. Going towards 20 keV many electrons travel deep into the substrate as the penetration depth increases with the electrons energy.

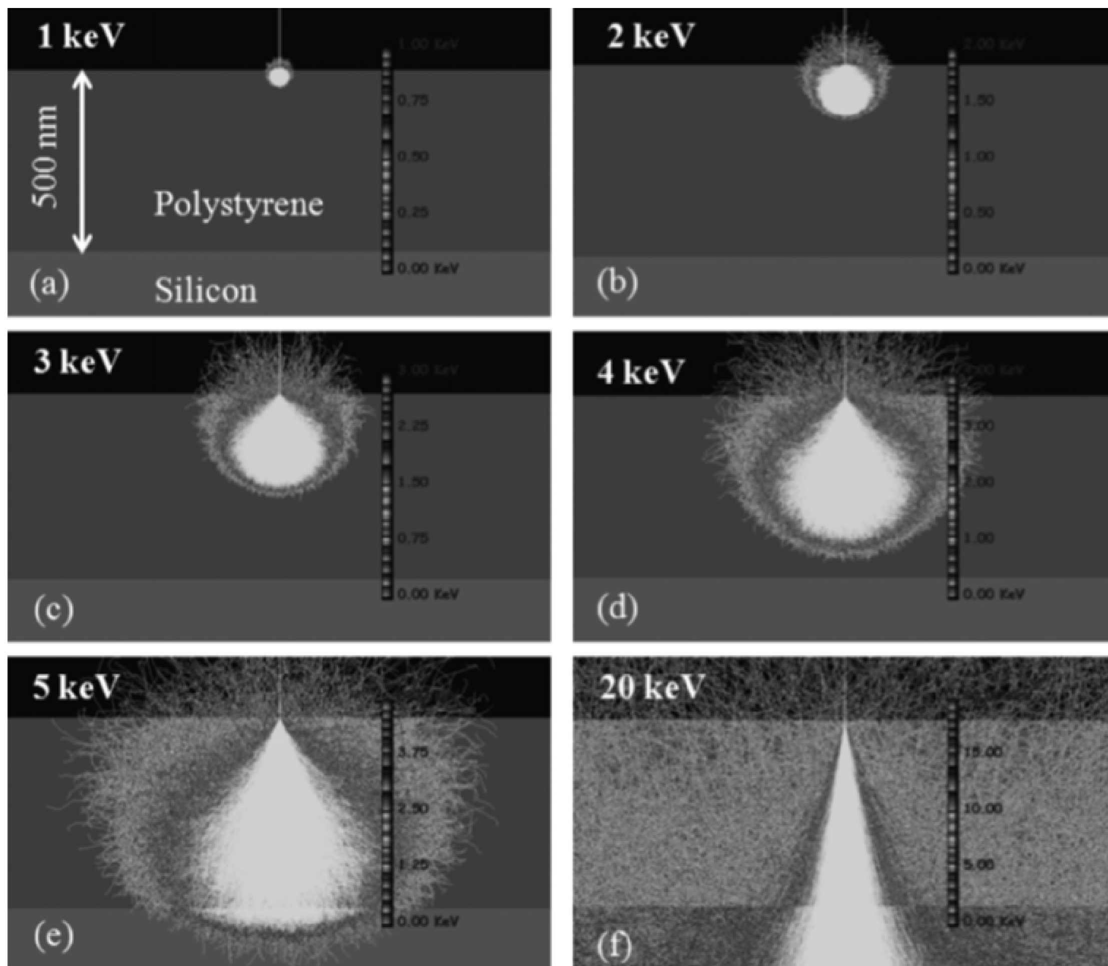

FIGURE 1.11: Monte Carlo simulation of electron trajectories in polystyrene. Incident electron energies from 1 keV to 20 keV, from [36]

The exposure of the resist is affected by more factors than just the beam energy, such as the resist film thickness, substrate atomic number, resist atomic number. However some relationships will hold independent of these factors. The energy loss per unit path length and the forward-scattering cross-section decrease as the energy of the beam increases, which means that the lateral spatial distribution and the dissipated energy per forward-scattered electron are decreasing while the lateral spatial distribution of the backscattered electrons is expanding.

At very low energies, below 5 keV the scattering is very low, and it is possible to achieve high resolution. However, at such small energies only very thin resist films can be used, which can significantly impact the etch resistance. Furthermore,

the electromagnetic lenses used to shape and align the electron beam don't work very well at low energies. This is the reason why industrial EBL tools use 100 keV electron beams. Between 5 keV and 20 keV the effect of forward electron scattering is significant, as was shown in figure 1.11 and the pattern can suffer from short range proximity effects. However, increasing the electron energy above 20 keV, renders a straight trajectory of most electrons in the incident beam and scattering is reduced, offering improved resolution and more vertical sidewalls (better profile). [37].

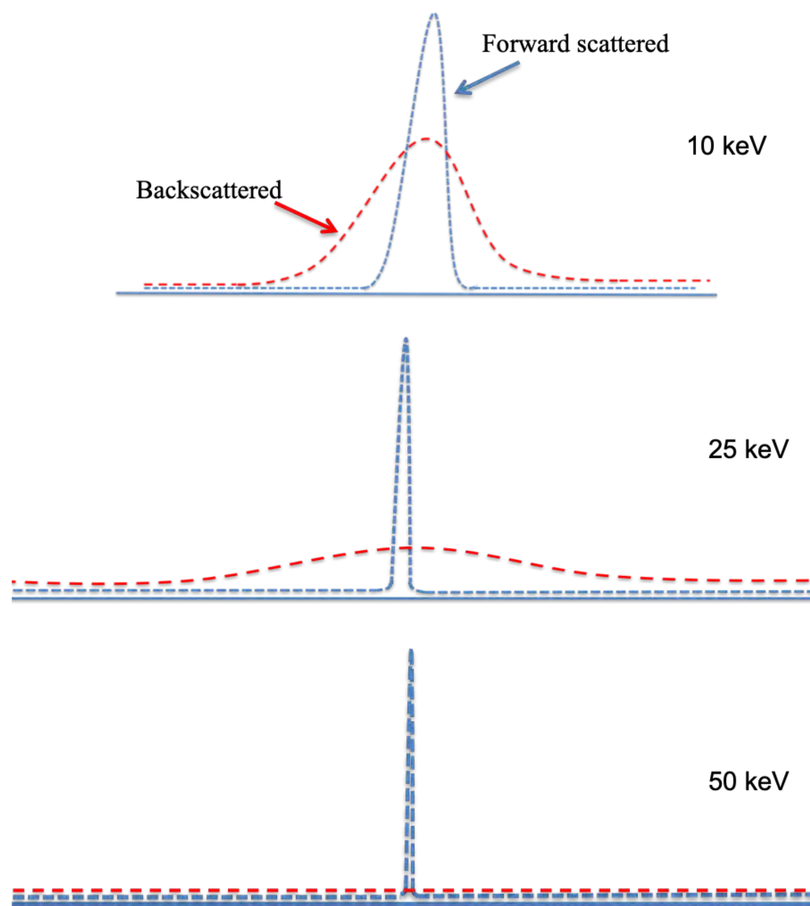

FIGURE 1.12: Distribution of electrons in the resist film during exposure with electron beam with acceleration voltages of 10 keV, 25 keV and 50 keV, adapted after [38]

Figure 1.12 demonstrates the exposure distribution of the electrons at incident

energies of 10 keV, 25 keV and 50 keV. It can be seen that the number of backscattered electrons decreases around the centre of the patterning area and the distribution becomes wider with the increasing of acceleration voltage of the incident beam. On the other hand, the forward scattered electrons become more focused in the patterning region and their distribution narrows as the incident beam becomes more energetic. From this, it can be observed that higher energy electron beams have an advantage over the lower energy electron beams with regards to the high angle forward-scattering, which will start happening in the substrate below the resist film without affecting the beam broadening [38].

Despite the high resolution and the flexibility in pattern choice, electron beam lithography is very slow, therefore it does not meet the requirements for the industrial throughput at the moment, but is the leading method for producing the masks used in all other types of lithography.

1.3.5 Ion Beam Lithography

Ion beam lithography shares its working principle with electron beam lithography. The main difference is that ions are used in stead of electrons. Ions have significantly higher mass compared to the electrons. The resolution achieved with the ion beam is comparable to that achieved with e-beam with the careful choice of ions. Due to the fact that ions are heavier than the electrons, they will generate 50 to 100 times more secondary electrons when interacting with the resist molecules at 30 keV acceleration voltage [39], reducing the required dose. On the other hand, the resolution is limited by the ion diameter, so small ions are used in lithography. The most used is the helium ion beam.

Due to their small mass He ions, much lighter than any atom in the resist material, but heavier than their counterpart, the electrons in EBL, will be loosing their energy in the top 100 nm of the sample being very slightly deflected from the

incident beam trajectory with a very small fraction of ions being backscattered [40]. This translates into significantly reduced proximity effect in IBL. The main drawback of this technique is the low throughput compared to photolithography.

1.4 Resist materials

Resist materials are usually classified as positive tone or negative tone systems. In the positive tone system, after the exposure the material becomes more soluble in the developing solvent. In negative tone resists the exposed areas become less soluble in the developer.

Another classification of the resist materials can be done according to the type of radiation the material is sensitive at: photoresists, e-beam resists, EUV resist and X-ray resists. Moreover, depending on the exposure mechanism resists can be classified as chemically amplified resists (CAR) and non-chemically amplified resists (nCAR). In order to further describe these materials, the main properties that characterise the performance of a resist material are introduced in the next section.

1.4.1 Important Properties

The most common parameters involved in the characterisation of the resist performance are sensitivity and contrast, which depend on the exposure wavelength, resist chemistry and the processing conditions such as baking temperature and developing solvent. Other primary metrics include resolution and line edge roughness (or line width roughness).

1.4.1.1 Sensitivity and Contrast

The sensitivity represents the dose required to change the dissolution behaviour of the resist. For positive resists the sensitivity is expressed as the dose at which the exposed areas are completely removed from the substrate. For negative resists the sensitivity is expressed as the dose at which 50 % of the film thickness is retained on the exposed areas, reflecting the point in each case at which the resist mask can be usefully employed for further processing.

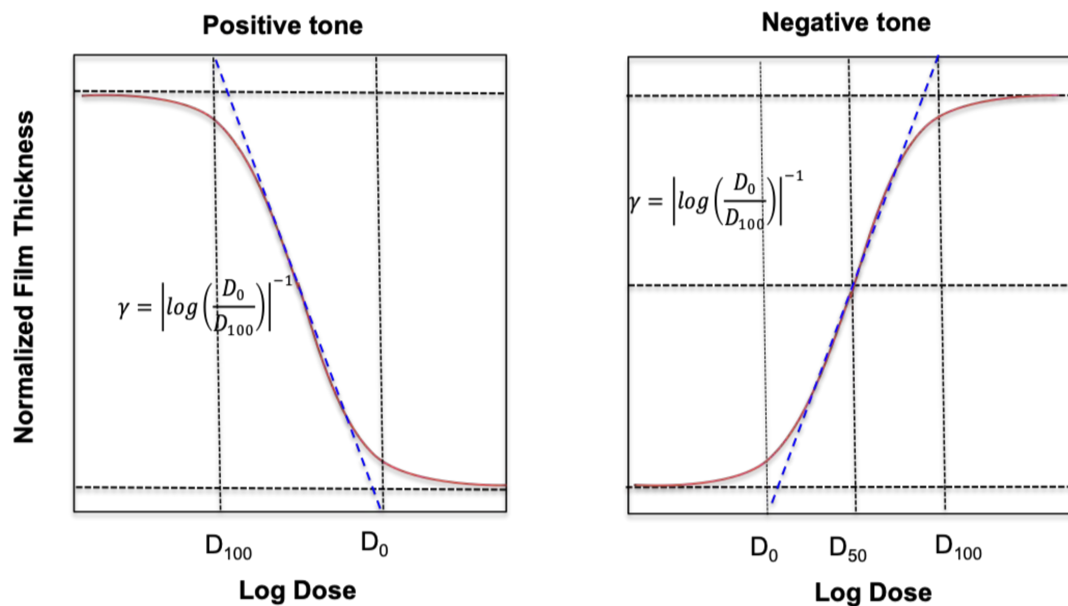

FIGURE 1.13: Example of sensitivity curves for positive and negative tone resist

The contrast of the resist quantifies the conversion of the spatial distribution of energy into spatial distribution of resist material that gives the relief image [41]. Contrast is given by the slope of the sensitivity curve (normalised remaining thickness of resist after development as a function of the dose).

1.4.1.2 Resolution

In lithographic terms there are two types of resolution: the pitch resolution, which is the smallest pitch that can be printed and the feature resolution, which is the

smallest feature that can be printed [42]. The pitch resolution will determine how closely together transistors on a chip can be packed and the feature resolution will impact the performance of an individual transistor. The physics of lithography limits the two resolutions differently. The pitch resolution is limited by the wavelength of the exposure source and the numerical aperture of the optical lens as postulated by the Rayleigh criterion. The feature resolution on the other hand is limited not only by the capability of the tool and the resist but also by our capability to control the entire lithographic process - exposure tool, development conditions and aspect ratio of the structures patterned, and post processes such as line trimming with a plasma etch.

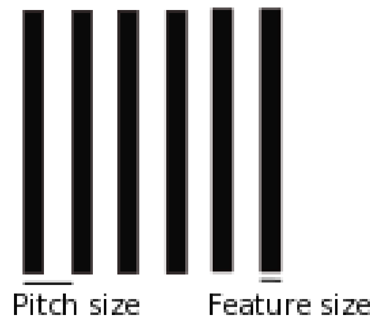

FIGURE 1.14: Representation of pitch size and feature size or critical dimension

The pitch in a pattern can be equal to the line width, in which case the lines of the pattern will be dense lines and if the pitch is larger than the line width, the lines are sparse lines, although the term semi-dense is used when the line width to the pitch ratio is less than 1:5.

1.4.1.3 Line Edge Roughness and Line Width Roughness

With the transition to sub-100 nm devices came the problem of feature roughness and its effect on the properties, reliability and performance of the device. Various

published studies draw a connection between the resist features roughness and the final device performance [43–51]. Other studies investigate the connection between process conditions such as PEB and the LER of the features [52] and more recent studies focus on the influence of secondary electrons interactions in photoresists on the LER value [53].

The line edge roughness quantifies the displacement of the edge position from the ideal. Line width roughness (LWR) quantifies the variation in line width. This can be done according to different methods [54].

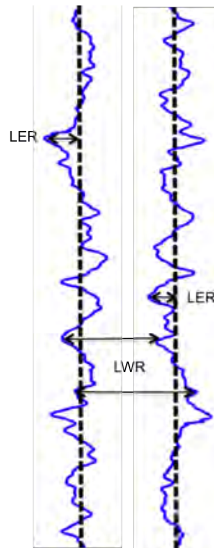

FIGURE 1.15: Representation of LER and LWR

Most commonly, the width of the feature is measured at a number of positions N over a length L. A width residual, w_i can be calculated at any point using the average width obtained over the length L. The IRDS (International Roadmap for Devices and Systems) specifications for LWR make use of three times the standard deviation of the root mean square metric, R_0, where R_0 is described in 1.8.

$$R_0^2 = \frac{1}{N-1} \sum_{i=1}^{N} {w_i}^2 \tag{1.8}$$

LER is a form of correlated and uncorrelated noise that shows along the edges of the resist features, which in CAR systems is caused by the acid diffusion over a spacial range. The correlation properties of the LER can be determined by analysing the LER along the feature length and the correlation function of the LER dictates the power spectral density (PSD) function. At large spatial frequencies corresponding to lengths smaller than the correlation length the PSD magnitude will be small. At low spatial frequencies corresponding to lengths larger than the correlation length the PSD magnitude will be large and this will be the range that contributes to the total LER the most.

1.4.2 Resist Materials Evolution

The resist material used for many years for i-line lithography was the diazonaphtoquinone (DNQ)/novolac resist, a two component system containing a novolac resin and a photoactive compound (PAC) –the DNQ. The novolac is soluble in aqueous base due to its phenolic functionality. However, the lipophilic DNQ will inhibit the dissolution of the resist film in an aqueous base developer. Upon exposure to 365 nm source of light the PAC will generate a highly chemically reactive carbene which will rearrange to ketene, which reacts further with water molecules in the film and produce indenecarboxylic acid [55]. The result is a photochemical transformation in the dissolution rate, and therefore the exposed areas of the film will dissolve much faster than the unexposed ones in aqueous developer. On the other hand the role of novolac in the lithographic performance of this resist is also important. The aromatic structure of this molecule provides it with high etch resistance and its molecular weight affects the dissolution, the thermal stability and the overall lithographic performance. The optimization of novolac polymer and DNQ properties with the improvement in i-line exposure tools increased the resolution of lithography to the sub 50 μm regime [56]. As the resolution requirements increased a translation from i-line towards deep UV (254 nm from Xe-Hg lamps

and 248 nm from KrF excimer lasers) was implemented. The novolac/DNQ resist exhibits poor imaging quality and insufficient sensitivity in this region. New resist materials had to be developed at this point. The sensitivity issue was tackled by the introduction of chemical amplification process. In the next sections the resist materials will be therefore categorised into chemically amplified resist (CAR) and non-chemically amplified resists (n-CAR).

1.4.3 Chemically Amplified Resists

Researchers initially focused on Polymethylmethacrylate (PMMA), which was successfully used as a positive tone resist for high resolution patterning below 5 nm in e-beam. Also hydrogen silsesquioxane (HSQ) gives similar results in e-beam as a negative tone resist. Despite the excellent resolution and very small LER values observed in both these materials the sensitivity was also poor.

The transition to deep UV needed a completely new concept and this was the chemical amplification. This was discovered in the 1980s, and utilises a catalytic reaction chain that is triggered by one initial photon or electron and exposes multiple molecules, as opposed to several photons needed to activate a single molecule in a non-chemically amplified system [55]. The quantum yield is significantly increased in a chemically amplified resist (CAR), and therefore the sensitivity is increased by several orders of magnitude. The photoactive component in a CAR is a photoacid generator (PAG). Photobase generators have been studied as well but base catalysis has not been accepted as a viable resist design yet. The selection of the PAG is based on a number of factors that impact on the lithographic performance of the resist material such as quantum efficiency of acid generation, compatibility with the resin, thermal stability, strength and size of released acid, impact on dissolution rate, etc. Many image formation mechanisms based on an

acid catalysed chain reaction have been developed including deprotection, scission, rearrangement, and polymerization/depolymeraization.

Deprotection was the first chemically amplified mechanism to be realised via acid-catalysed cleavage of a hydrophobic protecting group to expose a hydrophylic functional group. The IBM tboc resist was the first CAR used in a dynamic random access memory (DRAM) manufacturing with 248 nm lithography [57].

The material is a positive tone resist, consisting of poly(4-tert-butoxycarbonyloxystyrene) (PBOCST) and onium salt PAG, triphenylsulfonium trifluoromethanesulfonate. The mechanism of this resist is shown below:

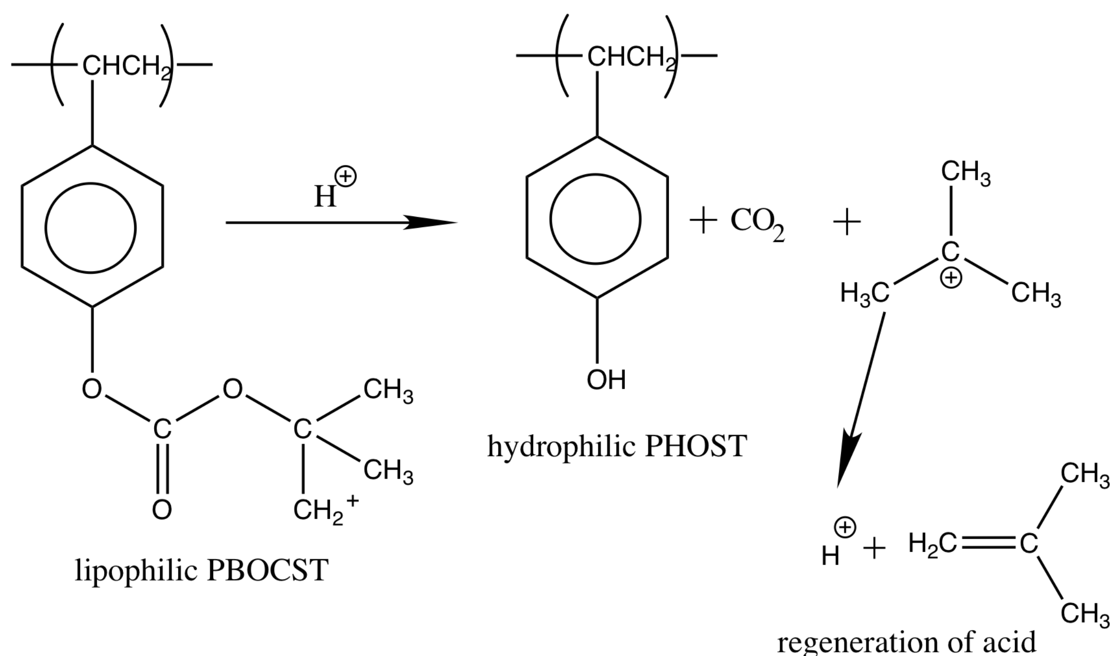

FIGURE 1.16: Acid-catalyzed deprotection mechanism for polarity change in poly(4-tert-butoxycarbonyloxystyrene) resist, from [57]

The phenolic hydroxyl group is blocked in the PBOCST with an acid-labile tert-butoxycarbonyl (tBOC) group, making the polymer hydrophobic. After the generation of photo-acid under exposure, the tBOC protection group can react with the acid, releasing a t-butyl cation and carbon dioxide. The t-butyl cation then deprotects to form isobutylene regenerating the proton. The PBOCST is converted into

a hydrophilic poly(4- hydroxystyrene) (PHOST), which is soluble in aqueous developers. As the acid is regenerated rather than consumed after the deprotection, the reaction is catalytic with a chain length of up to 1000 under normal process conditions [55]. The temperature required to activate the acid-catalysed reaction is around 100 °C, whilst the tBOC group is thermally stable up to 190 °C without acid.

Due to the excellent resolution achieved with this type of system, most of the subsequently developed advanced positive tone CARs are based on acid-catalysed deprotection. Typical examples are the hydroxystyrene type APEX resist, hydroxystyrene/methacrylate type ESCAP resist and acrylate type resists [41].

Negative tone CARs can also be created by using PAGs either for polarity change or to participate in a cross-linking reaction that will increase the molecular weight of the polymer and decrease their dissolution rate in the developer. The PBOCST resist can be used as a negative tone resist if the aqueous developer is exchanged with a non-polar organic developer such as anisole, which will dissolve the PBOCST rather than the PHOST removing the non-exposed areas in the resist film and leaving behind a negative tone image. SU-8 (Micro Chem) is a negative tone CAR based on acid-catalyzed cross-linking of the constituent epoxide functional groups. In this resist the negative tone patterning is realized by cationically catalized ring-opening polymerization, increasing the molecular weight and thus decreasing the polymer solubility [41, 55] as shown in 1.17

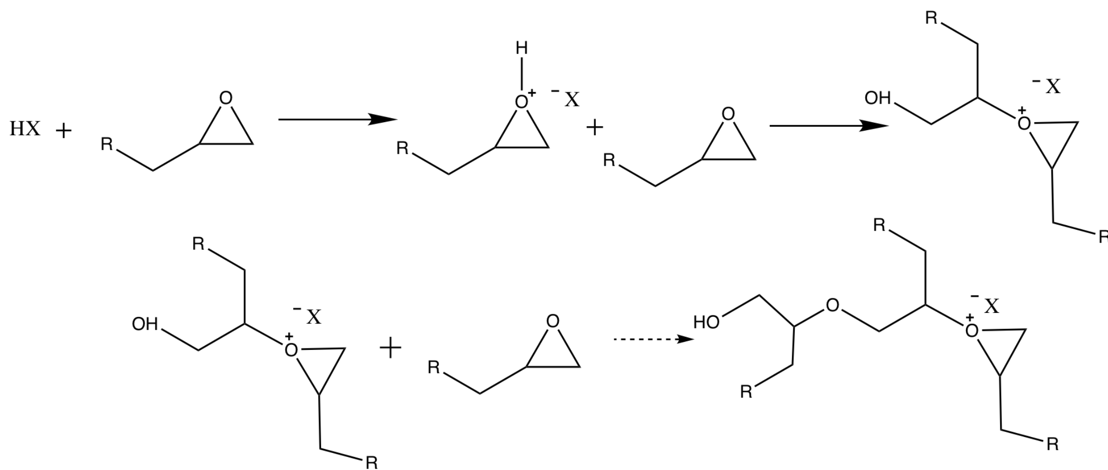

FIGURE 1.17: Acid catalyzed cross-linking mechanism in epoxy-based resists, from [57]

The mechanism works for very thick films, (>50μm) with high aspect ratio. The SU-8 resist also has a high thermal stability and demonstrates high sensitivity, which make it an ideal material for microelectromechanical systems (MEMS) [58]. However the most encountered issue in cross-linked CARs is swelling produced by the penetration of solvent in the cross-linked network. This can limit their high-resolution capability by distorting the patterns, introducing bridging or wobbling [55].

The main issue that limits the high-resolution in chemically amplified resists is the acid diffusion length, which can not be externally controlled during the exposure process. It is a stochastic process and it contributes to the LER. The figure below shows the chemical amplification process, schematiccaly.

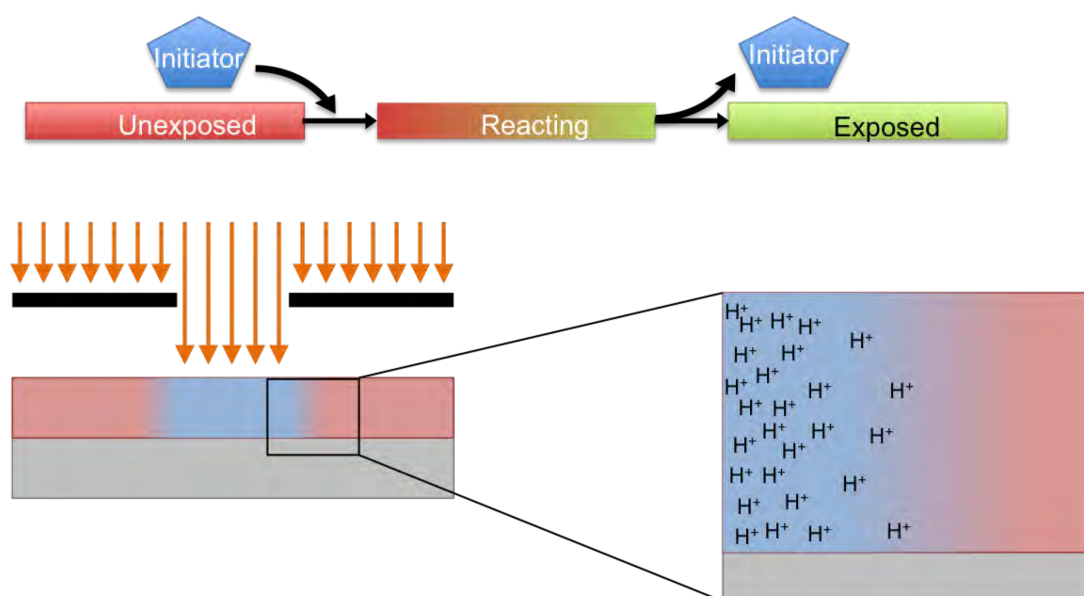

Figure 1.18: Schematic representation of chemical amplification and close up on the acid diffusion at the edges of the features from [59]

The acid diffusion length is dependent on a series of factors such as the type of polymer [60, 61], molecular size of PAG [61] and PEB temperature and time [62]. In order to reduce acid diffusion a base quencher molecule can be added to the resist formulation. The quencher is usually a base that either undergoes a competition reaction with the photoacid molecules by binding to resist molecules or neutralises the photoacid. Therefore, LER is reduced and resolution is improved [63].

However, the addition of the quencher molecules reduces the sensitivity of the resist and changes the dissolution behaviour of the material [64]. Moreover, due to the fact that the quencher is always added in very low concentrations relatively to the entire formulation, it is almost impossible to predict the distribution of these molecules in the resist film and therefore to precisely control the acid diffusion.

1.4.4 Non-Chemically Amplified Resists

Although CARs have shown high sensitivity, the inability to control the acid diffusion introduces high level of roughness in the features patterned on these materials limiting resolution for sub 20 nm feature size [60]. To address this issue new resist platforms have been developed.

Sulfonium Based Resists

Sulfonium salts have shown sensitivity to UV and electron beam and they can be bound to polymers [65]. Therefore they can be used as the radiation sensitive part of the non-chemically amplified resist. Such an example is the copolymer formed of (4-methacryloyloxy) phenyl) dimethylsulfonium triflate (MAPDST) and methyl methacrylate (MMA) [66]. Dissolved in ethanol this copolymer gives a negative tone resist formulation that shows a sensitivity of 2.06 $\mu C/cm^2$ in 20 kV e-beam exposure. Figure 1.19 shows the SEM image of the highest resolution achieved of 20 nm line width with 100 nm spacing [66].

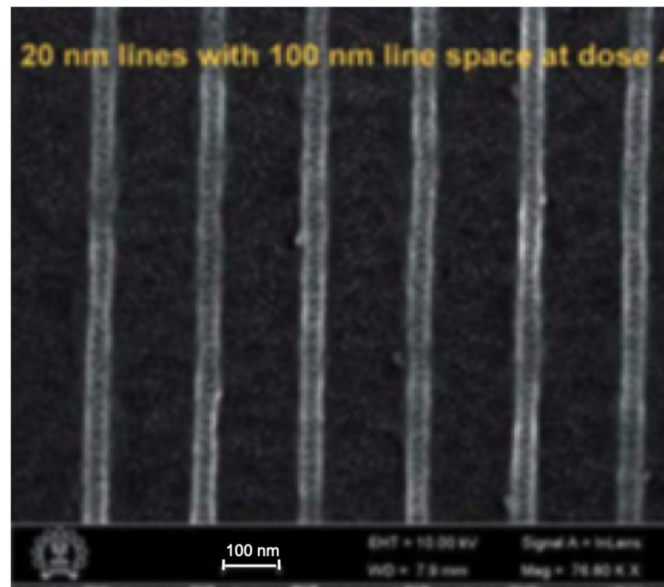

FIGURE 1.19: SEM images of isolated lines on fMAPDST-MMA resist at pitch 100 nm, line width 20 nm, dose 40 $\mu C/cm^2$ from [66]

The MAPDST-MMA resist also showed relatively low LER values of 1.8 - 2.0 nm. Due to its high sensitivity this material could be used as an e-beam resist.

Fullerene Based Resists

Tada et al. first found the potential of fullerenes as negative tone resists once they discovered its sensitivity to electron beam [67]. Its small diameter (0.7 nm) makes it a suitable material for high resolution lithography [68]. In their work, Tada et al. showed a solubility reduction of a C_{60} film in toluene after being exposed to e-beam [67], but its sensitivity is very low 12 mC/cm^2, as shown by Gibbons et al. [69].

Nevertheless, research has been done on incorporating the C_{60} into a polymer, which has a high electron sensitivity such as poly (p-chloromethylstyrene) (PCMS) [70]. A blend with poly hydroxystyrene (PHS) was required since the hydroxyl groups promote the adhesion of the C_{60} containing resist to the silicon wafer. The minimum resolution achieved with this material in 100 keV e-beam was 50 nm lines at 286 μC/cm^2 with a LER value of ~7 nm.

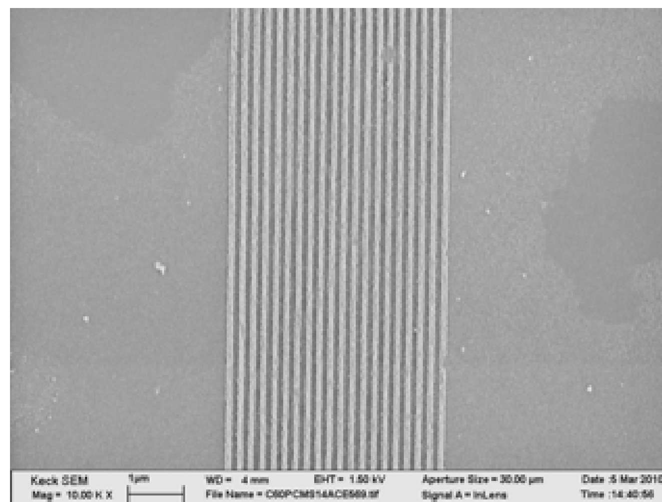

FIGURE 1.20: SEM image of lines patterned with EBL on C_{60}-PCMS-PHS resist from [70]

In figure 1.21 the results are shown from a different study by Yang D.X. et al. where phenol-based fullerene resists were introduced [71]. The line width in these

images varies between 13 and 15 nm and the exposure was done at 30 kV at a dose range between 240 and 350 pC/cm^2.

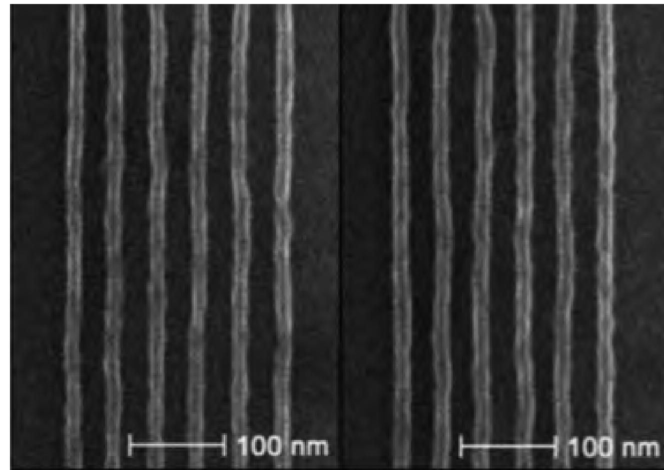

FIGURE 1.21: SEM images of single pixel lines on fullerene based resist at pitch 48 nm (left) and 46 nm (right). Measured LWR on these features is 4.5 nm for the 48 nm pitch and 3.4 nm for the 46 nm pitch from [71]

This material contains a cross-linker and a PAG moiety and works as a negative tone CAR for e-beam lithography. Figure 1.21 shows single pixel lines with the line width between 13 and 15 nm exposed in 30 kV e-beam at 240-350 pC/cm^2.

Inorganic Resists

Compared to organic resists, inorganic resists exhibit higher contrast and increased etch resistance whilst showing excellent resolution, but suffer from very low sensitivity. The material that stands out the most in terms of lithographic performance in this category is HSQ. Its cubic structure [72] shown in 1.22 opens under the electron beam forming cross-linked networks [73].

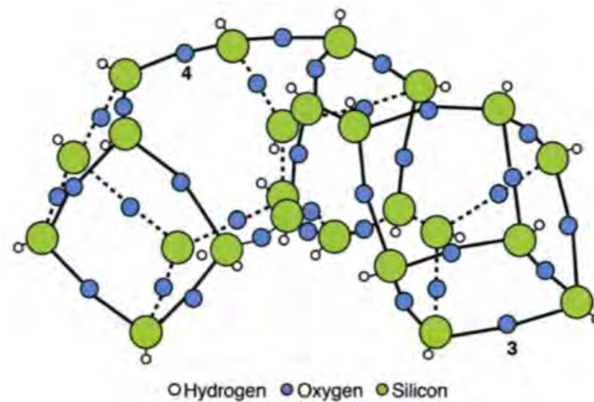

FIGURE 1.22: Schematic representation of resinous HSQ, from [74]

Studies have previously reported resolutions of 7 nm line width on dense lines patterns at $\sim$ 1 mC/cm^2 at 30 kV e-beam [75], 5 nm lines on 40 nm pitch at 10 kV [76] and isolated lines with 6 nm line width at 5.5 mC/cm^2 and 7 nm dense lines at 33 mC/cm^2 at 100 kV [77]. However, despite the excellent resolution of HSQ, its poor sensitivity issue together with its short shelf life time and high process variability prevent the industrial use of HSQ for next generation lithography.

Consequently, new materials containing silsesquioxane or other metal fragments were developed. Two of the most studied inorganic resists are the negative tone HafSO$_x$ and ZircSO$_x$ resists [78]. The cross-section opacity in these two polymers was measured to be higher than the electron density measured in PMMA, which makes the two novel materials more effectively absorbent to the energy of the incident electrons, therefore increasing the sensitivity of HafSO$_x$ to 21 µC/cm^2 and 7.6 µC/cm^2 for ZircSO$_x$ [79].

1.5 Pattern Collapse

Sensitivity, resolution and LER are important for characterisation of resists, but as the feature dimensions become smaller, issues like pattern collapse must be addressed in order for integrated circuit technology to progress. In 1995 Namatsu et

al. encountered limitations in designing silicon nanolines due to pattern plastic distortion introduced by the surface tension of water [80]. Their findings showed that pattern collapse occurred when the distance between the Si features was smaller than the product between a constant k, which describes the surface properties of the Si and the square root of the aspect ratio of the features. There are two main factors leading to pattern collapse. The mechanical strength of the material is an important characteristic, which dictates the likelihood of pattern collapse through bending of the features. Unbalanced capillary forces occur in the resist structure during drying and the mechanical stress introduced by these forces leads to bending or even breaking of thin features. An example of pattern collapse is shown in figure 1.23 where PMMA structures were patterned at different aspect ratios and pattern collapse was observed at aspect ratios higher than 4.16 [81].

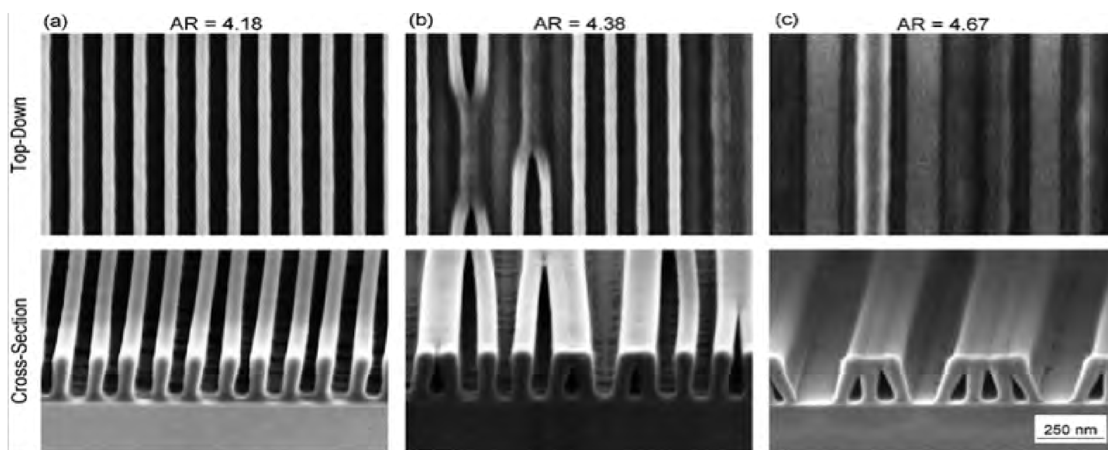

FIGURE 1.23: SEM images of left: stable, centre: collapsed, and right: super-collapsed pure PMMA nanostructures from [81]

Another mechanism of pattern collapse is adhesion failure between the resist structures and the substrate, due to mechanical stress caused by the excessive capillary forces of the rinsing liquid. In the simple approximation shown in figure 1.24 the resist features are considered to be rigid beams, which do not suffer from a breaking type of deformation. In this case, two rotation moments will be involved in pattern failure; the capillary forces produce one rotation momentum and the other one is produced by the van der Waals forces manifested at the resist-substrate

interface and referred to as the adhesion momentum. When the capillary momentum overcomes the adhesion momentum, the pattern will begin to peel off from the substrate and collapse will occur. The surface tension of the rinsing liquid will determine the force that distorts the resist features by introducing a negative pressure beneath the interface liquid-air between resist features. Figure 1.24 shows a schematic model of what happens during drying of the rinsing liquid.

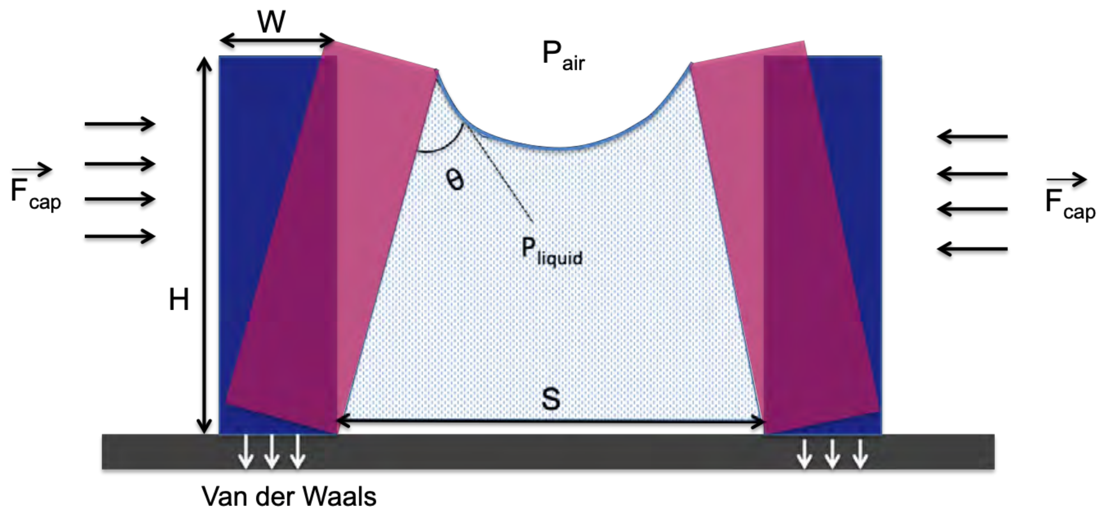

FIGURE 1.24: Schematics of the action of the two forces involved in the adhesion failure model of pattern collapse in resists features after development

The following set of equations were taken from [80] to derive the critical mechanical stress at the collapse point. The difference in the pressures exerted on each side of the meniscus is:

$$P = P_{air} - P_{liquid} = \gamma / r \quad (1.9)$$

where γ is the surface tension of the rinsing liquid and r is the radius of the meniscus formed by the rinsing liquid.

$$r = \frac{S}{2cos\theta} \quad (1.10)$$

where S is the spacing between the features and θ is the contact angle between the liquid and the feature surface. If we now rewrite P we get:

$$P = \frac{2\gamma cos\theta}{S} \tag{1.11}$$

This pressure difference introduces a bending moment, M on the features:

$$M = \int_0^H PLhdh = \frac{PLH^2}{2} \tag{1.12}$$

where h defines the vertical position of the feature wall with respect to the base. The radius of curvature introduced by the bending moment will then be:

$$R = \frac{EI}{M} \tag{1.13}$$

where E is the Young's modulus of the resist material and I is the second moment of area of the feature wall.

$$I = \frac{LW^3}{12} \tag{1.14}$$

where L and W are the length and width of the feature. At the bending moment, a tensile strain will occur on the outer side of the feature wall which is $W/(2R)$. The maximum tensile stress associated with this strain is given by:

$$\sigma_{max} = \frac{EW}{2R} \tag{1.15}$$

The maximum compressive stress exerted on the inner side of the feature wall can then be calculated:

$$\sigma_{max} = \frac{6\gamma cos\theta}{S}(\frac{H}{W})^2 \tag{1.16}$$

As can be seen in equation 1.16, as the aspect ratio of the features increases, the stress during developing in a given liquid with a certain surface tension increases as well. To lower the maximum stress on the resists features, choosing another

solvent with a lower surface tension has been investigated. Various strategies have been investigated to reduce the pattern collapse in EUV lithography [82, 83] and the properties of the resist material responsible for pattern collapse intensively studied [84, 85].

Some research groups have studied the use of alternative rinsing and drying methods to manipulate and possibly reduce the capillary forces. Therefore, surfactants have been added in the rinsing liquid [86, 87], supercritical fluid added in the drying process [88, 89], and the combination of surfactant and supercritical fluid has been tested [90]. However, these methods introduce shrinkage or swelling of the resist features. An alternative route towards the mitigation of the pattern collapse is to enhance the adhesion strength between the resist film and the substrate by using interface layers as adhesion promoters.

1.5.1 Silanes as Adhesion Promoters

Adhesion forces manifested between substrates and resists in the lithography process influence the mechanical properties and quality of the resist pattern. Organic (resist) and inorganic (substrate) materials are very different in their chemical reactivity and surface properties, and as a result strong adhesion between these two materials is hard to achieve. An adhesion promoter will act at the interface between the organic and the inorganic parts of the system to chemically and physically combine their individual properties. This adhesion promoter will have dual chemical functionality (organic and inorganic). A suitable head group, such as a silane will give the molecule reactivity to the inorganic wafer, and an organic tail group attached to the head will offer the adhesion promoter organic reactivity. The general chemical structure of a silane group is represented below:

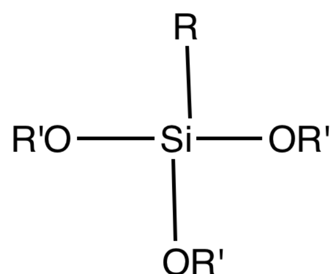

FIGURE 1.25: General chemical structure of a silane molecule. R can be an aryl, alkyl or organofunctional group and OR' can be a methoxy or an ethoxy group

The silanes condense with themselves to give an oligomeric structure [91] on the substrate and the tail groups are available to bind to the resist, promoting the adhesion between these two dissimilar materials. Nonreactive adhesion promoters can be also used to enhance the adhesion between organic and inorganic surfaces by manipulating the atomic forces (Van der Waals interactions, dipole interactions) at the interface. Much of the work conducted so far in this field has involved the use of hexamethyldisilazane (HMDS) which makes the surface more organiphilic by manipulating the van der Waals interactions between resist molecules and functional groups on the substrate [92]. Van der Waals forces, however, are weak interactions. Therefore, a better approach in addressing adhesion failure would be to introduce a surface modifier that covalently binds both to the resist and to the substrate. The predominant adhesion promoter type is organosilane and it has been widely studied in a broad range of applications [92, 93].

Silanes chemistry

Silicon, as well as carbon, is placed in the fourth group in the periodic table of elements. Silicon binds four substituent groups to form the most stable form. Hence, silicon compounds can be synthesized to have both organic and inorganic functionality in a single molecular structure, which indicates the use of silanes as adhesion promoters. Due to its electropositive nature, silicon will manifest a high chemical reactivity.

Inorganic hydroxyl terminated surfaces such as -Si-OH, -Al-OH, or metal-OH are able to react with chlorine, amine, methoxy, acetoxy or hydroxyl groups from a silane molecule. The product of this bond is not normally stable but through a condensation reaction silaxane -Si-O-Si- or silazane -Si-NH-Si- are generated [91] as shown in 1.26.

In the case of chlorosilanes and methoxysilanes ($RSiCl_3$, or CH_3O) hydrolysis is the reaction leading to formation of silanetriol, -$Si(OH)_3$ which is then followed by condensation to form the stable siloxane -Si-O-Si-.

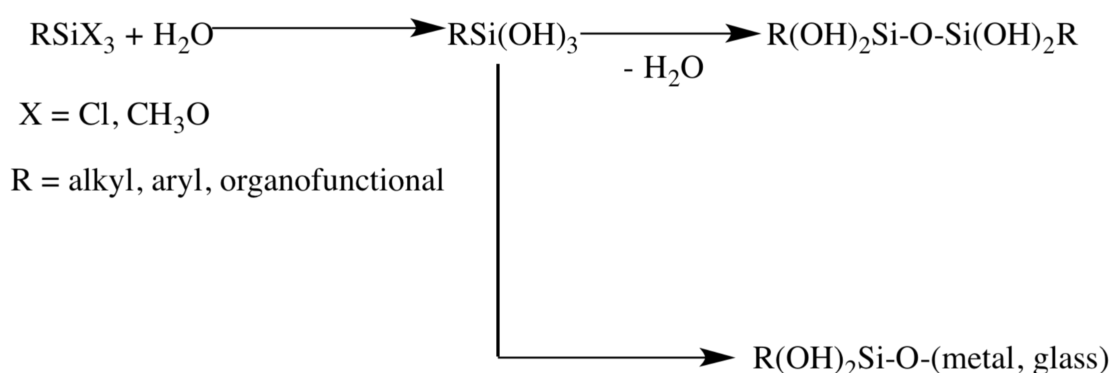

FIGURE 1.26: Diagram of silanes chemistry, from [91]

In an adhesion promoter the silicon atom can be bound to non-reactive organic groups such as methyl, ethyl, butyl, octyl, phenyl, or to a functional organic group with a reactive group such as amino, epoxy, methacrylate or sulfide. A spacer group is normally encountered in such structures to separate the silicon atom from the organo-functional group. Depending on the length of the spacer chain the chemical reactivity of the organic group resembles the reactivity of the carbon analogue compound (at least three carbons length in the spacer), or the reactivity of the organic group will be influenced by the silicon atom (one or two carbons length in the spacer)[91]. Other reactive silanes, particularly vinyl silanes, -$Si\text{-}CH{=}CH_2$, and silicon hydrides, -Si-H, are useful reactive groups in silicon chemistry [91].

Bonding to the inorganic surface (the substrate)

The reactive inorganic groups in a silane based adhesion promoter easily and rapidly bind to a wide range of inorganic surfaces (silicon, aluminium, metals in general) [91]. Using either residual water from the inorganic substrate (retained after the cleaning process) or added water a hydrolyse reaction can occur between alkoxy groups in the silane based adhesion promoter and silanols form. A coordination reaction then occurs between the silanols and the hydroxyl groups on the inorganic surface forming an oxane bond and releasing water [94].

Control of the siloxation formation in monolayers on a planar substrate without 3D growth of a polymer is difficult to achieve. Considering this, ethoxysilanes are a better choice over the methoxysilanes or chlorosilanes since they hydrolyse at slower rates, producing less oligomer in the solution and reducing the probability of forming multilayer films [94].

Once the adhesion promoter is attached to an inorganic surface, the surface chemistry of the functionalized surface will be dictated by the reactive organic group in the adhesion promoter. The silanized substrate now exhibits the surface energy of the reactive organic group in the silane adhesion promotor [91].

Bonding to the organic surface (the resist)

The interaction of the silane based adhesion promoter with the organic film (resist) is more complex. For a thermoset polymer, such as the resist material which cross-links when exposed to the suitable type of radiation, the chemically reactive organic groups in the silane molecule will bind to the organic functional groups in the resist film as long as their reactivities match [95], therefore the choice of adhesion promoter molecule is trivial for the mechanism to work.

Adhesion promoters act with the optimum performance when the organo-functional group is involved in the curing mechanism of the polymer structure. Therefore, either an epoxysilane or an aminosilane can participate in the curing mechanism of an epoxy resin; and phenolic resins have several different reaction modes so that

several types of silanes (amino, epoxy, and chloroalkyl, for example) share good characteristics with phenolic composites [91].

All the above being mentioned, a choice of the optimum silane molecule to be used as an interface between the inorganic surface and the resist material can be made considering the organic functional groups in the resist film.

1.6 Overview of Lithography Techniques

Technique	Source	Resist	Resolution	Observations
UV Lithography	i-line 365 nm	DNQ/Novolac	350 nm [96]	5 step and repeat processes
DUV Lithography	KrF 248 nm	PBOCST	180 nm [96]	5 step and repeat processes
	ArF 193 nm	Acrylate and alicyclics	100 nm [96]	4 step and repeat processes
	ArF 193 nm Immersion	Acrylate and alicyclics	40 nm [96]	Improved resolution Water immersion systems introduce deffects
EUV Lithography	13.5 nm	CAR	12 nm [97]	Good resolution, high sensitivity Swelling issues, low cost-efficiency
		HSQ	7 nm [98]	World record resolution Poor sensitivity
Electron Beam Lithography	2 keV	PMMA	5 nm	Positive tone 10 μC/cm² at 2 keV, 90 μC/cm² at 20 keV Good resolution. Poor resistance to corrosive etch.
	10 keV	PMMA derivative	10 nm	Negative tone 1 μC/cm², improved sensitivity
	20 keV	Sulfonium based	20 nm [66]	2.06 μC/cm², relatively low LER (1.8 - 2 nm)
	30 keV	Pure fullerene (C_{60})	20 nm [69]	12 mC/cm², very poor sensitivity
	100 keV	PHS-C_{60}	50 nm [70]	286 μC/cm², LER 7 nm
	30 keV	Chemically amplified C_{60} derivatives	13 nm [71]	8 μC/cm², high sensitivity Some swelling. Etch resistance twice as high as standard novolac based resists
	100 keV	HSQ	6 nm – isolated lines 7 nm – dense lines [77]	5.5 mC/cm² and 33 mC/cm² -very low sensitivity. Extremely good resolution
Ion Beam Lithography	30 keV	HSQ	5 nm half pitch [99]	120 pC/cm
	30 keV	Pure C_{60}	~ 7 nm sparse pitch [100]	40 μC/cm² sensitivity higher than EBL

FIGURE 1.27: Summary of lithographic techniques with corresponding resist materials and their describing lithographic parameters [96–98], [66], [69–71],[77] [99, 100]

1.7 Thesis Outline

Chapter 1 presents a general introduction to the field of lithography with theoretical background to each of the lithography types. Further, I have listed some of the resist mechanisms with their benefits and limitations in order to offer an overview the evolution of materials used in lithography and to underline the importance of the research presented in this thesis, which is conducted for the development of a new material to be used in the next generation lithography.

In **chapter 2** the experimental methods and the equipment used are described and the details of the approaches taken are discussed.

In **Chapter 3** I will introduce the xMT resist system, together with the enhanced variants, EX2 and EX3. I will also discuss the results achieved when introducing metals in the xMT system and their impact on the lithographic performance in terms of sensitivity, LER changes and resolution. I will then present the approach of using an non-metallic high-Z element in the xMT, EX2 and EX3 systems and evaluate the change in their lithographic performance.

In **chapter 4** I will describe the multi-trigger resist concept, discuss the mechanism and present data obtained with EUV-IL and EBL in MTR1, MTR2 and MTR3.

In **chapter 5** of the thesis I will present approaches that have been taken to achieve ultimate resolution in the MTR resist. These include finding the optimum processing conditions - such as film thickness and post exposure bake - the introduction of the appropriate interface between resist and wafer to increase adhesion and mitigate pattern collapse, and also post-exposure processing such as assisted rinse (UV assisted or acid additive rinse).

Chapter 2

Experimental Techniques and Methods

2.1 Materials used

The resist materials used in the following experiments are multi-component resists containing a resin, which is proprietary to Irresistible Materials Ltd (IM), and a cross-linker, photo-acid generator, quencher, and other additives that were bought and used as received, or synthesised by IM, and are listed below.

- xMT, EX2 and EX3 - proprietary resins synthesised by NanoC Inc for Irresistible Materials Ltd. molecular weights: 722.88, 718.53, 951.08; T_g of xMT is 70 °C and the relative density is $\sim$ 1 g/cm^3.

- cross-linkers: Tris (4-hydroxyphenyl) methane triglycidyl ether, molecular weight 460.53, from Sigma Aldrich and iodinated cross-linkers synthesised by IM.

- photo-acid generator: Triphenylsulfonium hexafluoroantimonate, molecular weight 762.51, from Midori Kagaku Co.

- quencher: Triphenylsulfonium tosylate, molecular weight 434.28, from Midori Kagaku Co.

- other additives: tin iodide (SnI_2), iodobenzene (C_6H_5I), from Sigma Aldrich.

The solvents used were bought from Sigma Aldrich and are listed below.

- Ethyl lactate (photoresist grade), cyclohexanone, dichloromethane, chloroform, propylene glycol methyl ether acetate, 4-Methyl-2-pentanol and n-butyl acetate.

For the silanization experiments, four silanes were used and are listed below.

- Triethoxy vinyl silane from Sigma Aldrich, amino propyl triethoxy silane from Sigma Aldrich, 3-glycidyloxypropyl (dimethoxy) methylsilane from Tokyo Chemical Industry and EDMSPA from Tokyo Chemical Industry.

In general I prepared the resist formulations by mixing the appropriate ratio of components and solvents. Formulations that received treatment to reduce trace metal contaminants were prepared by IM/NanoC.

2.2 Electron Beam Lithography

Electron beam lithography is a specialised technique for creating extremely fine patterns. The method involves scanning an electron beam across the surface of the resist film depositing energy in a designed pattern into the resist film. In this technique electrons are accelerated into a beam and finely focused onto the sample. The beam switches off and on as it scans the surface and pauses at each location on the sample long enough to deposit the appropriate dose. In this way the designed shapes of the pattern are written into the resist. Figure 2.1 shows a diagram of the electron beam lithography tool. The main components of the tool are as follows: the electron source for generating the beam; lenses; a mechanism for deflecting the beam; a blanker to turn the beam on and off; stigmator for correcting

any astigmatism in the beam; apertures for defining the beam; alignment systems for centering the beam in the column and an electron detector for assisting with focusing and locating on the sample.

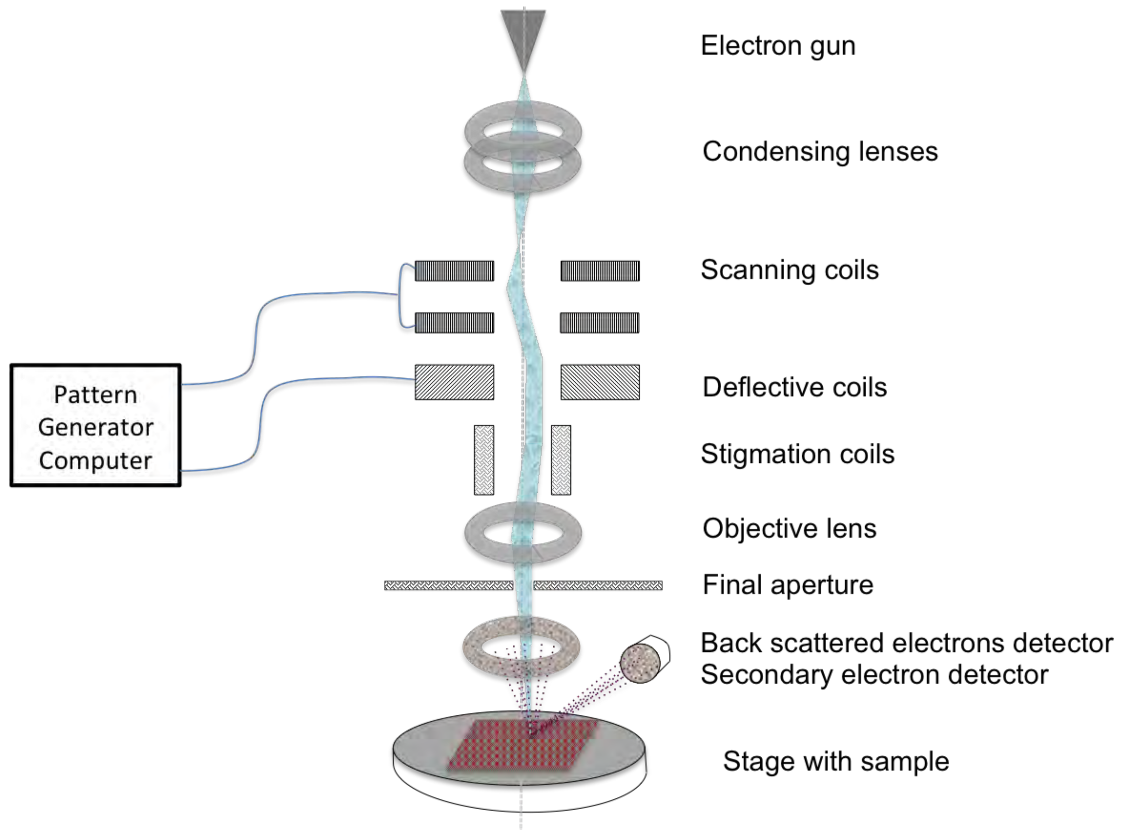

FIGURE 2.1: Diagram of electron beam lithography tool

The lenses and stigmator are used to focus the beam to a small round spot at the sample. The minimum dot diameter is limited by space-charge effects but can approach 1 nm. Despite the fine beam adjustment, one nanometre size features are hard to achieve. The limited resolution in electron beam lithography comes from the interaction of the incident electrons with the atoms in the resist, which lead to electron scattering within the material.

In this study an upgraded Jeol SEM equipped with an ELPHY PLUS pattern generator was used to produce and image high-resolution patterns on Si substrates at beam energies up to 30 keV. The equipment offers a high spatial resolution of down to 5 nm using a finely aligned beam emitted by a Schottky field emission gun.

The pattern generator operates by controlling the deflection coils and blanking aperture of the SEM, allowing the beam to scan a defined area for a specific dwell time and deposit the calculated dose required to draw the pattern in that area.

Additionally, an industrial exposure tool was used at Paul Scherrer Institute –Vistec with an electron beam acceleration voltage of 100 keV. The pattern used to investigate high resolution capabilities of various resist formulations is shown in figure 2.2.

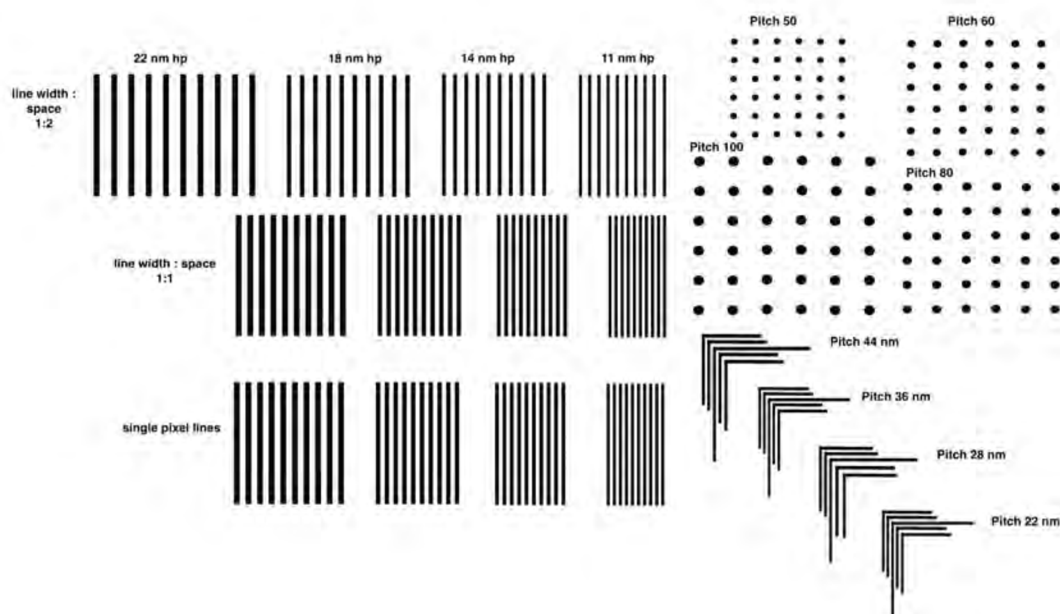

FIGURE 2.2: Diagram of electron beam pattern

2.3 EUV Lithography

The EUV exposures were conducted at the Paul Scherrer Institute and the photons were extracted from the Swiss Light Source synchrotron. Extreme Ultraviolet Interference Lithography (EUVIL) uses 13.5 nm photons, which are generated from the synchrotron utilising an undulator filtered through a pinhole to give a spatially coherent beam that is focused onto a transmission mask consisting of a

pair of gratings as shown in 2.3. Because air would absorb the photons the system has to operate in vacuum.

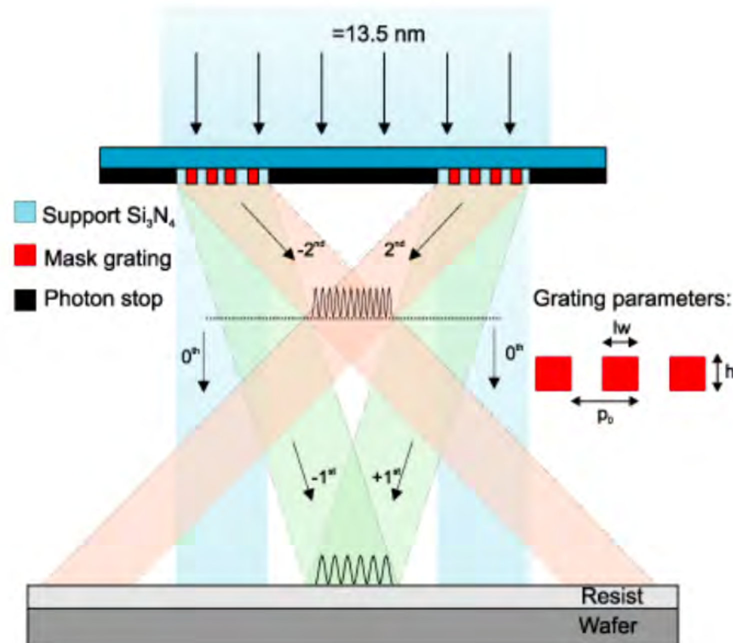

FIGURE 2.3: Schematics of the EUV Interference Lithography from [101]

A simplified diagram of the EUVL tool is shown in figure 2.3. At this wavelength photons are easily absorbed by any material (glass, air), therefore refractive lenses can not be used in the system and reflective lenses (mirrors) have to be used instead. Mirrors must have a structure based on Bragg reflection using a period structure of an alternating sequence of layers of molybdenum and silicon with thickness corresponding to one quarter of wavelength of the illumination source for normal incidence. A Fresnel reflection will be produced at each interface between two layers. The optical path difference between reflections from consecutive interfaces is half the wavelength of the source [102]. Therefore, all reflected components from the interfaces of the mirror interfere constructively, which results in a strong reflection. The number of layers and the difference in the refractive index of the two layer materials determine the total reflectivity. The pattern on the substrate is the interference pattern of the light diffracted from the mask. Depending

on the spacing and arrangement of the gratings on the mask, the features in the lithographic pattern can be tuned.

Figure 2.4 shows the design mask used for the EUV-IL experiments presented in this thesis and the SEM image of one of the fields exposed on the resist sample. Pitches 28 and 22 only the 0 order can be seen due to the low exposure dose. At pitch 32 both 0 order and first interference order can be seen. For pitch 44 the dose used was high enough to obtain the second orders of interference as well.

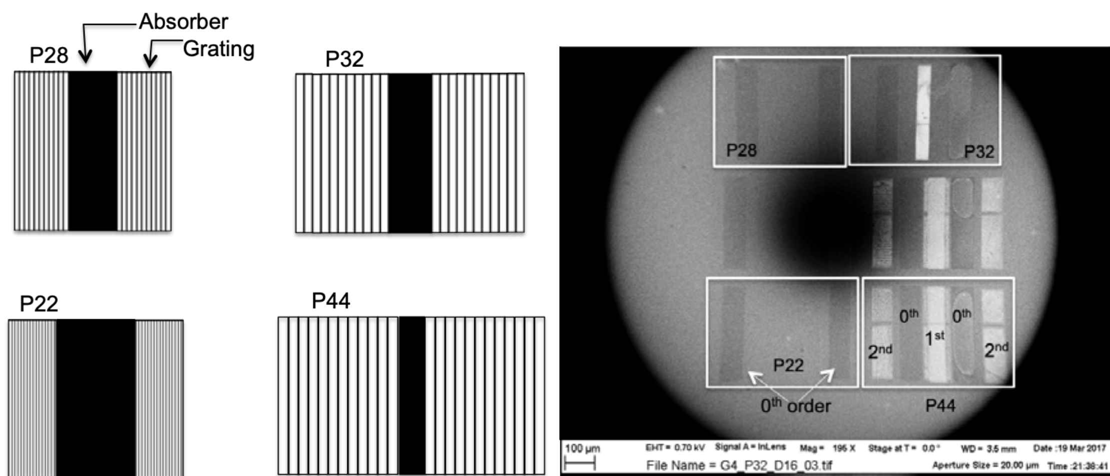

FIGURE 2.4: left: Design of the mask used for the EUV-IL experiment; right: SEM image of one of the 16 fields exposed on the resist using this mask

Resist films spin coated on silicon chips of 28 × 28 mm were loaded on the sample holder and introduced in the exposure chamber, which was then pumped down to a vacuum level of 10^{-7} mbar. The exposure file containing information such as dose and the spatial coordinates of the positions where the pattern should be exposed on the sample was then uploaded on the computer controlling the movement of the mask and sample holder. On each of the resist samples, 16 fields were exposed, with dose increasing exponentially from field 1 to field 16.

2.4 Image Analysis Using SUMMIT

SEM images of features obtained through lithography were analysed using a commercial software package from EUV Technology Corporation, called SUMMIT (SEM Metrology Interactive Toolbox), which is designed to detect the edges of features in the image and measure quantities such as critical dimension and calculates LER and LWR values. It has been used worldwide in many applications in the lithographic field since it was first introduce in 2004, such as mask defects inspection [103], LER characterisation [104] or simply for resist lithographic description (CD and roughness). Moreover, when analysing images containing contact holes and dots, SUMMIT offers information about the diameter of the features, their uniformity and eccentricity –which quantifies the deviation of the patterned contact hole or dot from the nominal circular shape. The program has implemented a filtration operation, which offers filtered LER and LWR values after the SEM noise contribution was cut out. There are other softwares that are used for edge detection in SEM images such as Demokritos and more recently Fractilia but SuMMIT is the most widely used package for this purpose at this time.

In order to measure the LER accurately it is necessary to have a certain minimum line length due to the spatial frequency dependence of LER. The software analysis uses a bound box model and derives the LER from a power spectral density across the box. The variance of the edge displacement (LER) extracted from the PSD is calculated according to the following equation [105].

$$\sigma^2 = \frac{2\pi}{L} \sum_{j=0}^{N-1} PSD_n \tag{2.1}$$

where L is the length of the line, j is the position on the line, N is the number of measurements, n is the frequency bin in the Fourier transform and the PSD is

obtained from the Fourier transform as follows:

$$PSD_n = \frac{L}{2\pi}|F_n|^2 \tag{2.2}$$

In addition to metrology in lithographic features, SuMMIT contains functions for integrated stochastic resist modelling based on the SEM images and resist parameters introduced by the user [106]. Figure 2.5 shows an example of data obtained from analysis of lines and pillars SEM images.

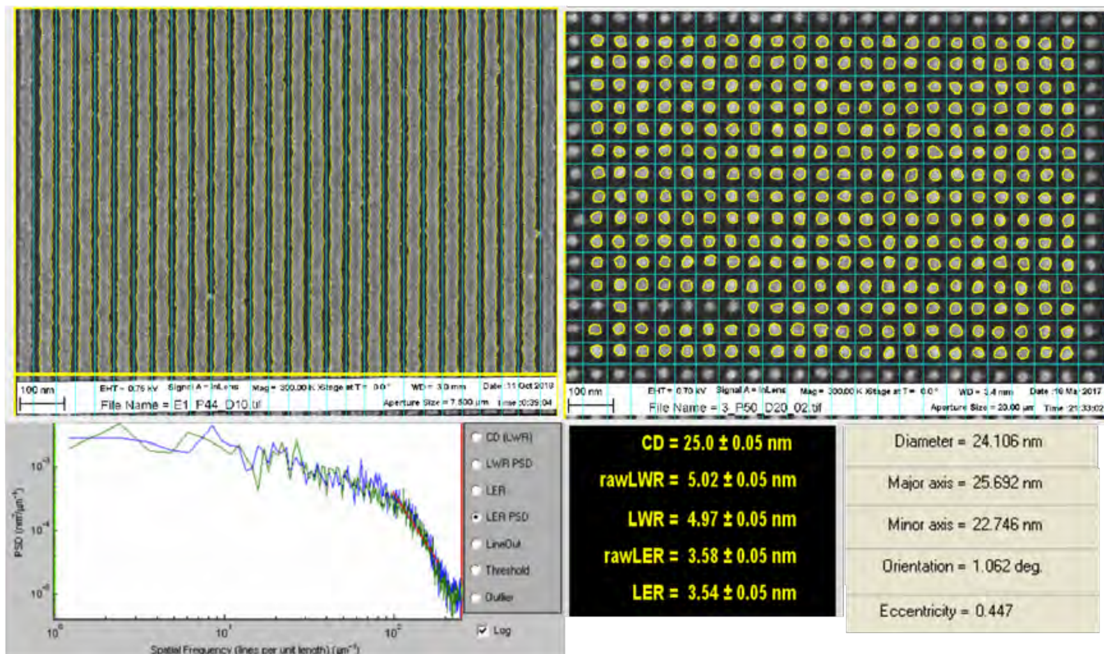

FIGURE 2.5: Summit analysis results from lines and pillars. PSD curve shown is obtained from the SEM image of the lines

When measuring critical dimensions, SuMMIT offers an average value after analysing a number of features in the SEM image ($\sim$ 30 lines, $\sim$ 400 pillars or holes at magnification 300000) at a number of N locations along the features. The error on these values varies between 0.02 and 0.07. A larger error would be obtained if multiple images of the same CD were analysed, however the difference between different images can be attributed to a series of factors such as SEM noise during imaging, SEM focus, electron beam damage of the features during focusing, as

well as fluctuation in parameters of the exposure tool during the experiment, none of which can be controlled. However, for the experiments presented in this thesis a control resist was prepared, exposed and analysed at the beginning of each set of experiments to set a reference for the newly developed materials. Using this reference offers information about any changes that might have occurred in the exposure tools between experiments (including mask degradation, dose fluctuations due to technical modifications etc).

2.5 Sample Preparation for Lithography

The resist material used in the experiment was the negative tone molecular xMT resist and consists of a mixture composed of the resin material, photo acid generator (PAG), and cross-linker (CL), plus other optional additives in different ratios. The casting solvents used were ethyl lactate, chloroform and cyclohexanone depending on the formulation. Silicon wafers were diced up into chips of 28 $\times$ 28 mm using an automatic dicing saw machine. After dicing, the silicon chips were cleaned in acetone for 10 min and in isopropanol for another 10 min in the ultrasonic bath. This was then followed by further cleaning using a 3:1 solution of H_2SO_4 and H_2O_2 for 10 min to ensure the removal of any organic contaminants on the silicon. Finally, a 1 minute treatment with Hydrofluoric acid (HF) was applied. A volume of 80 µl from the resist mixture was dispensed on top of Si substrates (28 $\times$ 28 mm^2) using a P-6708D spin coater at different spin speeds (1500 to 3500 rpm) depending on the required resist film thickness. The spin coating process starts with a spreading step at 500 rpm for 5 seconds followed by a ramping step for 5 seconds, coating step at chosen spin speed for 45 seconds and a final step at 4000 rpm for 5 seconds to ensure complete solvent evaporation. After dispensing the resist the Si chips were baked on the hot plate at 60 °C for 3 min. This process

is known as the post application bake (PAB) and it has the role of removing the excess casting solvent.

Another baking process takes place after the exposure, this is known as post exposure bake (PEB) and it has the role of accelerating the catalysis of the photoacid in the crosslinking reaction. In chapter 6 I show data acquired without the PEB step. The last step in the resist processing is the development process. The solvent used as developer is n-butyl acetate (nBA) and each exposed sample was developed for 60 s and then rinsed in 4-methyl-2-pentanol (MIBC) for 15 s.

2.6 Silane Deposition Methods

The aim of the silanisation experiment was to introduce an interface between the silicon substrate and the resist film in order to increase the adhesion at the organic and inorganic interface and therefore suppress pattern collapse, which occurs in fine patterns during the development process, due to poor adhesion.

A clean surface is a precondition to achieve covalent binding of the silane to the native SiO_2 layer on the silicon [107]. The silicon chips used for underlayer deposition were firstly cleaned in isopropanol for 10 min in the sonication bath, rinsed in deionized water (DI) and then blow dried with nitrogen gas. In order to break down any organic contaminants from the surface the silicon substrates were further treated in piranha solution (H_2SO_4:H_2O_2, 3:1 by volume) for 10 min. The piranha treatment also has the role of the hydroxylation the surface and makes it chemically reactive. Then, the chips were thoroughly rinsed with DI water and blow dried with N_2 gas. Piranha treated silicon chips were stored in DI water until starting the silanisation process in order to keep the surface away from any contamination and preserve the hydroxyl groups.

Several silanes were tested including the vinyl triethoxy silane as it was found that the vinyl groups can thermally crosslink to the functional groups in our resist during the PAB [108]. Ethoxy groups are preferred rather than methoxy groups since ethoxysilanes hydrolize at much slower rates than methoxysilanes forming less oligomer in the solution reducing the potential of producing multilayer films [94]. The hydroxylated Si substrates were treated with vinyl triethoxy silane in order to alter the inorganic surface properties of the substrate and promote the adhesion to the organic resist film.

Three deposition methods were investigated: immersion of the Si substrate in 0.1% (V/V)silane solution in dichloromethane for 1h; spin coating of the pure silane on the Si substrate; and vapour priming of the silane solution on the Si substrate in a glove box over night. Before spinning and vapour priming, the hydroxylated Si substrates received a dehydration bake of 150 °C for 5 min. The immersed substrates were not pre-baked, as water is required in the silanization reaction. Figure 2.6 presents a schematic diagram of the different methods for the silanization process.

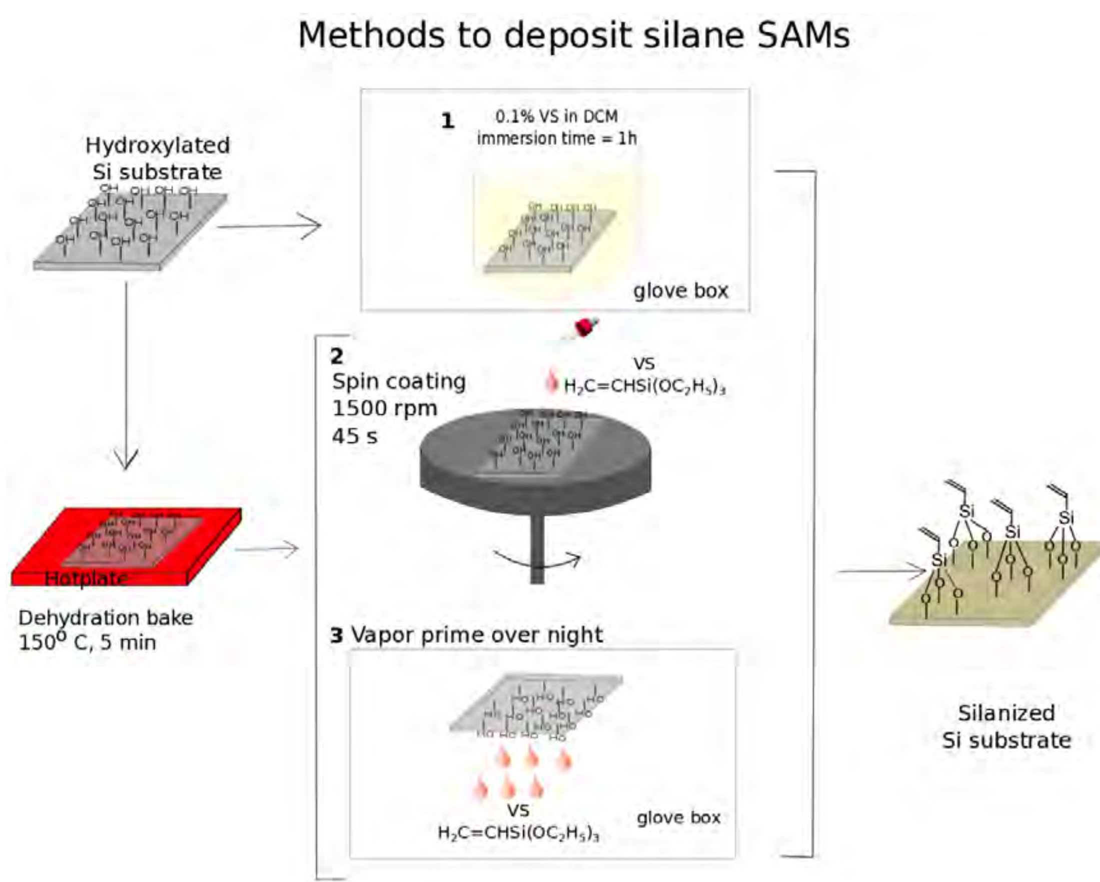

FIGURE 2.6: Methods of silane deposition: 1. immersion, 2. spin coating, 3. vapour priming

In the experimental work, variations of the processes described in the diagram were tried, i.e. the immersion time was varied between 30 min to 4 hs to find the optimum deposition rate, the spin coating was performed from pure silane solution as well as dilution in various solvents such as anisole, toluene and dichloromethane.

2.7 Contact Angle Microscopy

In order to check any changes in the surface, Contact Angle Microscopy can be used to compare the surface energy of the silanized samples with the bare Si substrate. The contact angle is the angle formed by the intersection of a drop

resting on a flat surface (liquid-solid interface) and the liquid-vapour interface. A small contact angle is observed when the liquid spreads on the surface, and a large contact angle will be observed when the liquid beads up. The shape of the drop, and implicitly the value of the contact angle, is determined by the surface tension of the liquid. In practice, the contact angle is defined by a combination of surface tension and external forces such as gravity. On an ideal solid surface the contact angle of a drop of liquid is described by mechanical equilibrium of three surface tensions:

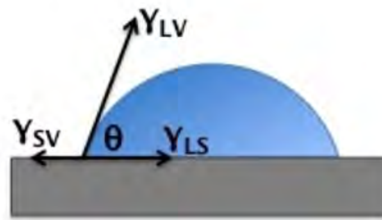

FIGURE 2.7: Young's contact angle (static contact angle) at mechanical equilibrium of surface tensions of the three phases - solid, liquid and vapour

$$\gamma_{lv} cos\theta_Y = \gamma_{sv} - \gamma_{sl} \tag{2.3}$$

where γ_{lv}, γ_{sv} and γ_{sl} are the interfacial tensions between liquid and vapour, solid and vapour and solid and liquid and θ_Y is the contact angle. Equation 2.3 is referred to as Young's equation and θ_Y is Young's contact angle.

The measurement of a single static contact angle to characterise the wetting behaviour of a solid surface is not a very accurate technique since the wetting phenomenon is more than just a static state. Therefore the dynamic contact angle was measured and analysed in this experiment with respect to the investigated surface heterogeneity.

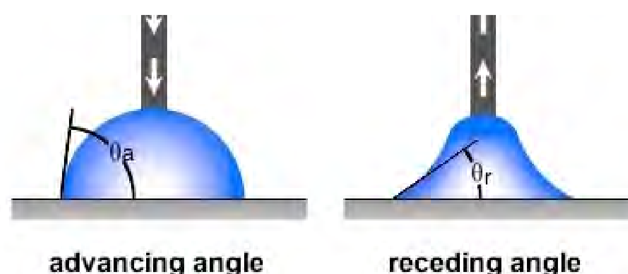

FIGURE 2.8: Illustration of dynamic contact angle technique

The technique consists of expanding and contracting the liquid on the solid surface and measuring the advancing, θ_a, and receding, θ_r, contact angle. These angles cover a range, with the advancing angle approaching a maximum value and the receding angle approaching a minimum value. For non-homogeneous surfaces there will be variation in the contact angle as the motion of the water droplet encounters domains while advancing or receding from the surface. For example if on a hydrophilic surface there are hydrophobic domains, while water wets the surface and the size of the droplet increases and reaches these hydrophobic domains, the motion of the water will be hindered and an increase in the contact angle will be detected. In the same way, a decrease in the contact angle will be observed during the receding of the droplet when the motion of the water will be again hindered by the hydrophobic domains. Similarly, the roughness of the substrate can also pin the drop edge increasing the difference between θ_a and θ_b.

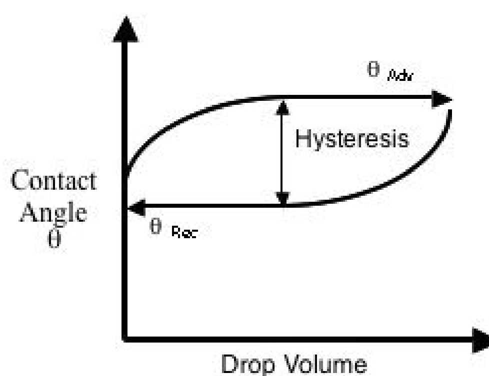

FIGURE 2.9: Theoretical plot of hysteresis curve between advancing and receding contact angle

The difference between the advancing angle and the receding angle is called the hysteresis, H and is a consequence of the surface heterogeneity and/or roughness. A homogeneous surface should not show a hysteresis higher than 10°. If a large number of different domains are present on the surface the hysteresis will increase.

In this experiment a Theta instrument was used was used in sessile drop mode. The liquid used to measure the contact angle on silanized silicon wafers was deionized water. The size of the droplet was 5 µl. The advancing and receding angle were measured and the hysteresis was calculated and plotted to determine whether the surface was homogeneously modified during the silanization process. The contact angles were measured at 10 positions on the wafer, 5 positions away from the center on the x axis and another 5 on the y axis.

2.8 Surface Profiler

The surface profiler was used to measure the thickness of the resist films on the silicon wafers and to determine spin speed curves. The equipment used during these experiments was a Dektak3ST profilometer.

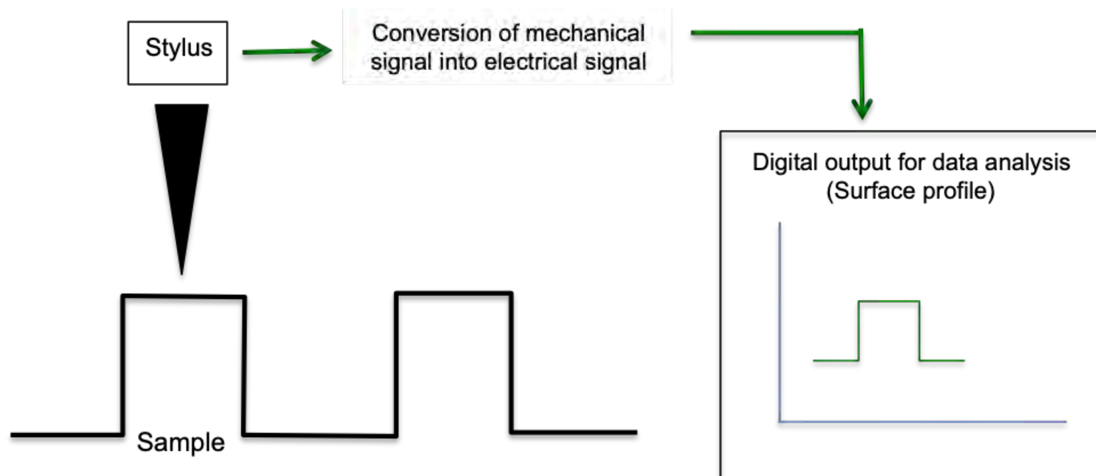

FIGURE 2.10: Diagram of surface profiler

This system measures film thicknesses and surface roughness electromechanically by scanning the surface with a diamond stylus and recording the profile. The radius of the stylus is 2.5 μm and the vertical resolution is 1 nm for general application with thin film, and 8 nm for thick, very rough or curved surfaces. Depending on the surface topography the scan length, scan speed and stylus force can be adjusted accordingly. All thicknesses measured in this thesis were below 50 nm and the measurement range allowed for 1 nm resolution. After spin coating the resist films on the silicon substrate, a step was created on the film by scratching the substrate with a scalpel. This procedure removes the film leaving behind bare silicon wafer. The depth of the scratch was then measured, thus determining the the thickness of the film. Three scans at different positions across the wafer were taken and the average value was calculated. Once measured, the thickness of each material, the spin speed and concentration of the formulation were recorded and reused in order to achieve the desired thickness.

2.9 FTIR (Fourier Transform Infrared Spectrometry)

The principle of IR is that, at resonant frequencies, molecules absorb frequencies characteristic to their structure. The resonant frequencies are related to the strength of the bond and the mass of the atoms in the bond, and therefore the IR spectrum can be used to identify the bonding and the atoms of a molecule.

In FTIR a beam containing a range of wavelengths is used to illuminate a sample and the transmitted intensity of the beam is measured after its interaction with the sample. The process is repeated with different combinations of wavelengths and the transmitted signal after the interaction with the sample measured. After all the raw data has been collected it is being processed by a computer and a spectrum

is generated to show the absorption of light by the sample at each individual wavelength. The algorithm used in processing the data is a Fourier transform operation hence the name of the technique.

The equipment used in the experiments presented in this thesis is a PerkinElmer Spectrum Two Nutraceutical system Version 10.400 with DTGS (deuterated triglycine sulfate) detector. The wavenumber range is between 4000 cm^{-1} and 650 cm^{-1}. This is the mid-infrared region and is used in the study of fundamental vibrations in molecules and associated rotational-vibrational structure. FTIR spectra were taken of drop-casted films of resist solution on silicon.

Chapter 3

xMT Negative Tone Molecular Resist System

This chapter will introduce and describe the xMT resist, which is the baseline system for the resist platform developed during this study. Furthermore, the enhanced variants of the xMT molecule, EX2 and EX3 are also described and their lithographic performance in electron beam and EUV-IL is presented. Metal hybrids of the xMT have been investigated as an approach to increase photo-absorption in EUV and ultimately boost sensitivity. Metal ion contamination in the resist synthesis is also investigated in this chapter and Metal Ion Removed (MIR) formulations are compared to the respective non-MIR formulations. Lastly a non-metal high-Z additive is introduced into the xMT, to increase opacity, without addition of metals. The sensitivity and resolution of the resulting material is presented.

3.1 xMT

With the progress of EUV lithography tools, a new resist material ready to replace the 193 nm photoresists is required to support the new technology [109–111]. To

date no material meets the RLS (the relationship between resolution, LER and sensitivity of a material) requirements, for instance as given by the International Roadmap for Devices and Systems. CARs have pushed their resolution towards 14 nm hp but the sensitivity dropped to 30–40 mJ/cm^2 [112, 113] or more. Metal based resists on the other hand, whilst exhibiting excellent resolution had to improve the sensitivity to meet the new requirements. 25 mJ/cm^2 for 16 nm hp and 35 mJ/cm^2 for 13 nm hp have been reported [114] bringing the two platforms, CARs and inorganic resists to around the same level.

At this point the solution to the trade-off RLS relationship is in developing completely new chemistry pathways in new generation resists. Molecular resists were designed to overcome the limitations of polymeric materials such as the size of the constituent monomers. The smaller size of molecular resists is expected to render smaller LER at resolutions below 50 nm [115].

Irresistible Materials and the University of Birmingham have co-developed a negative tone molecular resist system, xMT, for EUVL and EBL applications. The xMT resist demonstrates good sensitivity and low LER while maintaining high resolution [116]. The xMT molecule is synthesised by reacting diazabiccycloundecene-7-ene (DBU) with tert-butoxycarbonyl (tBOC) protected phenol on a malonate chain. The cross-linker tris(4-hydroxyphenyl)methane triglycidyl ether with molecular weight 461 is purchased from Sigma Aldrich. The PAG used is triphenylsulfonium hexafluoroantimonate from Midori Kagaku Co. The nucleophilic quencher is tripheylsulfonium nonaflate also purchased from Midori Kagaku Co. Figure 3.1 shows the chemical structure of all the components in the basic xMT system.

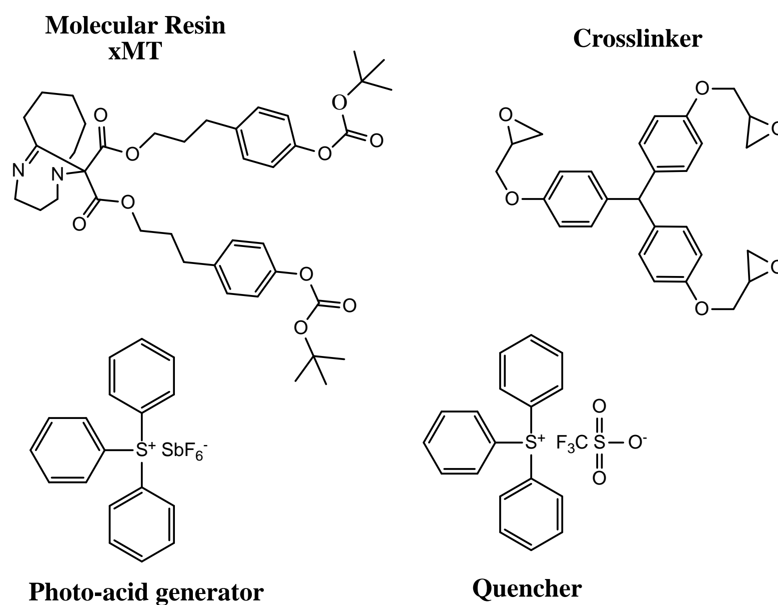

FIGURE 3.1: Chemical structure of components in the xMT baseline system

The reaction mechanism in the xMT material is yet to be elucidated but it is likely that multiple reaction pathways are taking place involving cationic epoxy chain growth and epoxy-phenol condensation. The lithographic performance of xMT resist was analysed in previous studies in this group both in EUV as well as electron beam. The sensitivity of xMT to a 20 kV electron beam was found to be 18.7 μC/cm^2 with a contrast of 1.4 [117]. At 30 kV semidense lines on 38 nm pitch with a CD of 14.7 nm and a LER of 4.5 nm were obtained using a formulation of 0.2:2:1 xMT, cross-linker and PAG [117]. Further improvements have been made to the xMT resist formulation such as choosing a new cross-linker molecule or using a different purification method in the synthesis of the xMT molecule designed to remove the metallic ion contamination and the system demonstrated a resolution of 14 nm half pitch at 14 mJ/cm^2 in EUV [118]. The high sensitivity of this xMT sample is due to the lack of quencher in the formulation, which is a drawback for the LER, which increases to 4.9 nm for this sample. Therefore, in section 3.4

the addition of high-Z sensitisers is investigated as an approach to maintain the resolution while increasing the sensitivity.

Infrared spectroscopy was performed on solid films deposited on silicon substrates and figure 3.2 shows the spectra obtained. This analysis was performed in order to gather information about the level of cross-linking in the resist and to get more insight on the reaction mechanism in the xMT system. The cross-linker and the PAG are the contributors to this reaction therefore, for simplicity the resin and the quencher were not introduced in these formulations. Three spectra are investigated for samples receiving the following treatment: the first sample is the control sample and was not exposed to any treatment, the second sample was exposed to UV for 15 minutes and the third sample was exposed to UV for 15 minutes and a thermal treatment was then applied for 1 minute at 90 ° C.

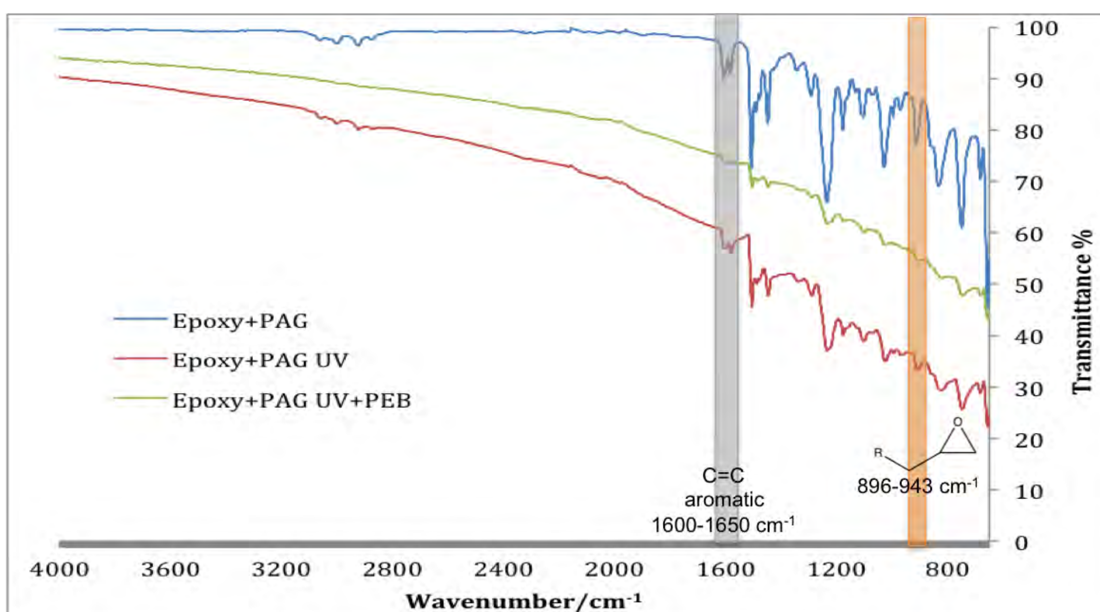

FIGURE 3.2: IR spectra of the cross-linker and PAG formulated in 2:1 ratio. blue line - no treatment applied, red line - UV exposed for 15 minutes and green line - UV exposed and post exposure bake applied for 1 minute at 90 ° C

Sample	Converted epoxies (%)
CL + PAG	27 ± 2.7%
CL + PAG + UV	31 ± 3.1%
CL + PAG + UV + PEB	90 ± 9%

TABLE 3.1: Conversion rate of epoxy groups in the CL+PAG, CL+PAG+UV and CL+PAG+UV+PEB samples as calculated from the IR spectra

Following a method described by R. Lawson in [119] to quantify the conversion of the epoxide group the change in the peak at 916 cm^{-1} is being monitored. In this method, the epoxide content is quantified by the integration of the peak centred at 916 cm^{-1}. The resulting area is then normalised for each spectrum by the area of the aromatic carbon-carbon peak situated at 1600–1650 cm^{-1}.

The evolution of the normalised epoxide peak is monitored in the three spectra and the expectation is that the intensity of the peak will drop towards 0 from the untreated sample to the UV exposed and post exposure baked sample, which will indicate that all the epoxide groups in the film have cross-linked. However, as can be seen in table 3.1 there is a remaining of 10± 5% of the total number of epoxide groups left which haven not been converted. The fact that the epoxide groups are not entirely converted suggests that there is room for formulation adjustment to be made in the resist formulations to find the optimum ratio of the components to render maximum cross-linking of the epoxide network without the need to increase the dose required to achieve this.

3.2 Formulation Optimisation Experiments

As a standard the ratio of the xMT baseline system is written as mass of resin : mass of cross-linker : mass of photo-acid generator : mass of quencher. Exposures in EUV and EBL were performed using formulations containing 0.2 ratio of the

resin (standard ratio) and 0.5 ratio (high ratio), while maintaining the CL : PAG ratio as 2:1. The images obtained using the two techniques were then analysed and conclusions regarding the optimum formulation were drawn. Varying the ratios of the components in the resist formulation can also offer some information about the exposure mechanism of the system.

Figure 3.3 shows electron beam lithography results at 30 kV using the xMT resist standard ratio.

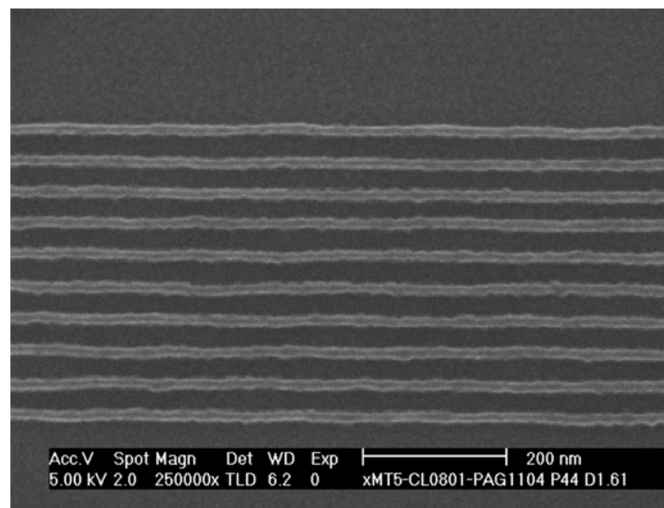

FIGURE 3.3: SEM image of xMT resist formulation patterned with 30 kV electron beam. Dose is 176.89 pC/cm^2, pitch size 44 nm, CD 15.6 ± 0.04 nm, LER 3.3 ± 0.07 nm

Experiments in EUV showed that increasing the xMT ratio in the resist formulation and keeping the quencher level constant improves the LER. Figure 3.4 shows lines patterned with EUV-IL at 32 nm pitch. The left image is using the standard ratio and the right image is with the high ratio. The LER improved slightly from 3.41 nm in the standard ratio formulation to 3.33 nm in the high ratio formulation. This improvement comes at the expense of sensitivity which decreases by 17% in the high ratio formulation.

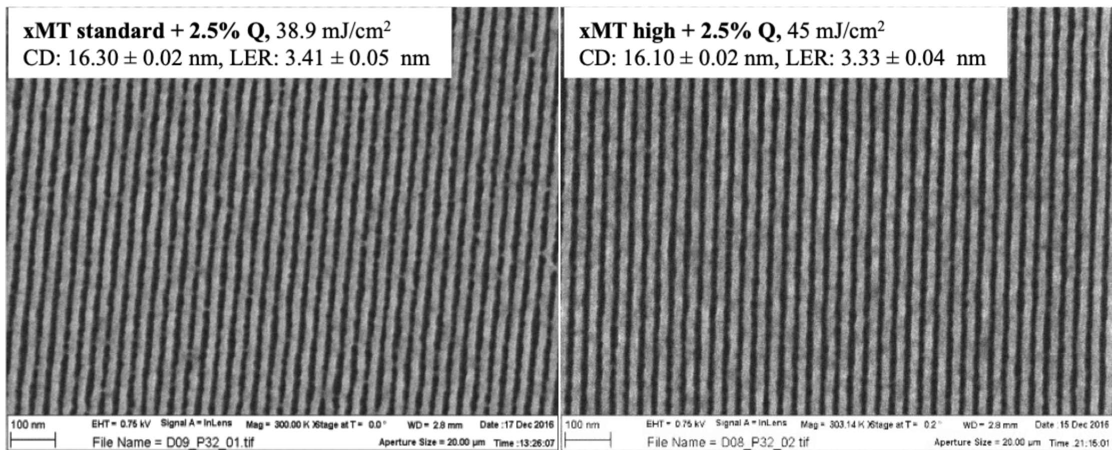

FIGURE 3.4: SEM images of xMT resist formulations at standard (left) and high resin ratio (right) with 2.5% quencher added

More interesting results are observed when comparing the standard ratio resist to a high ratio variant without quencher (high - NoQ). Figure 3.5 demonstrates the lines patterned with EUV-IL at 32 nm pitch on the two formulations. The standard ratio xMT with 2.5% quencher has a LER value of 23% of the CD, whilst the high-NoQ formulation maintains the same sensitivity has a similar LER value of 22% of the CD. As quencher is known to suppress LER in the baseline formulation, this implies an additional LER suppression mechanism occurs in the high resin containing resist matrix that leads to the formation of features with the same roughness, despite the absence of quencher.

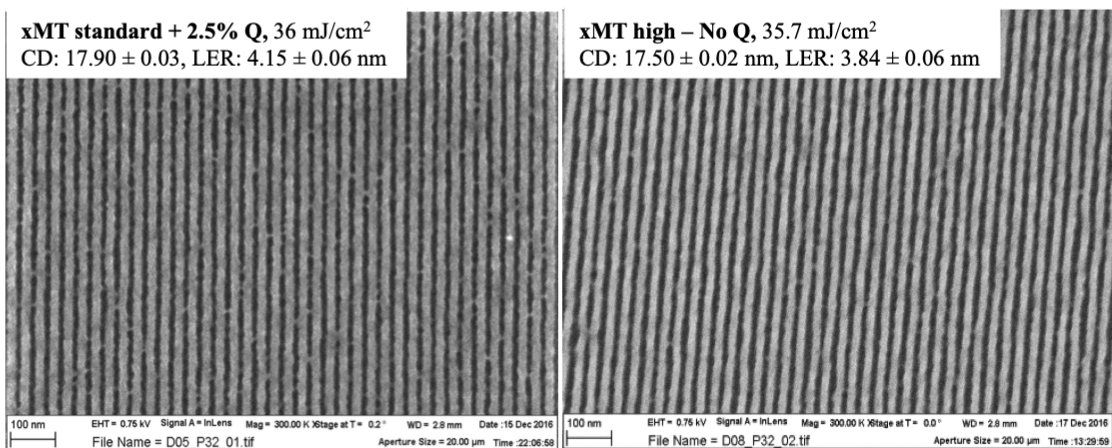

FIGURE 3.5: SEM images of xMT resist formulations at standard resin ratio with 2.5% quencher (left) and high resin ratio without quencher (right)

In EBL, given the flexibility in designing the pattern, in addition to dense lines at various pitches, dots, gratings and L-shaped lines have also been patterned using the two formulations of resist with standard and high resin ratio. Figure 3.6 shows 28 nm pitch dense lines patterned with EBL using the two xMT formulations. The standard formulation, is as expected, more sensitive than the high resin formulation but the quality of the lines is higher in the 0.5 formulation, i.e. with a lower LER value. The high LER value in the standard formulation can be partially attributed to the overdosing of the sample, since the formulation was more sensitive than the lowest dose in the experiment.

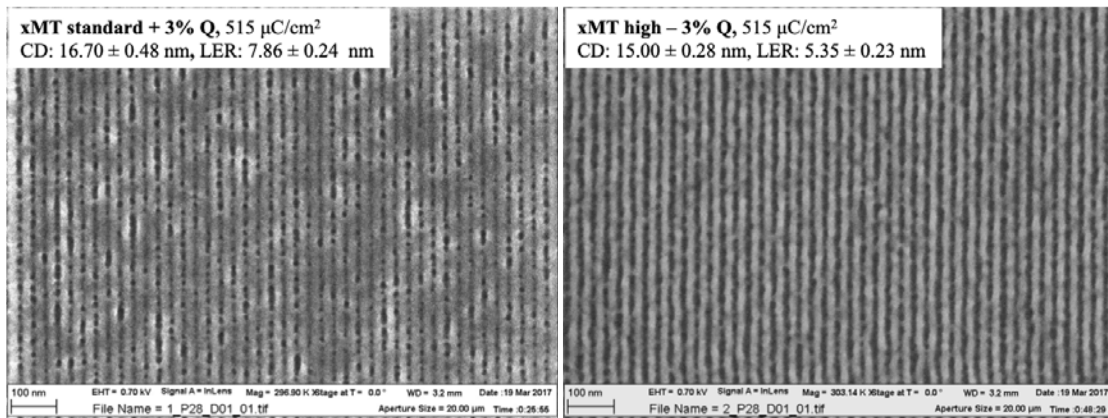

FIGURE 3.6: SEM images of xMT resist formulations at standard and high resin ratio with 3% quencher added.

When analysing pillars, i.e. nominally circular patterns, the three characteristics to monitor are diameter, uniformity (pilar to pilar) and eccentricity, which measures the deviation from the designed shape of an individual pillar. Figure 3.7 shows the pillars obtained on xMT standard and xMT high resin ratio. As with the lines, the standard formulation is more sensitive and gives pillars with an average diameter of 30.2 nm at dose 530 $\mu C/cm^2$ whereas the high resin formulation gives pillars with an average diameter of 25.4 nm at 672 $\mu C/cm^2$. Moreover the uniformity of the pillars patterned on the high resin formulation is lower than the standard formulation, but this can also be due to their smaller size and not entirely caused by the formulation.

At the same time the eccentricity of the standard formulation is lower than the eccentricity of the high resin formulation (0.415 or 1.31% of the average diameter as opposed to 0.447 or 1.76% of the average diameter) suggesting that the standard formulation is the better choice for patterning pillars in EBL. However, just as with LER, where the larger the CD the lower the roughness, the eccentricity of the high resin formulation could be better if the sample received a higher dose and diameters of the pillars were larger. Hence, in figure 3.7 the third image shows pillars patterned in the high resin formulation at 930 μC/cm^2, where the eccentricity of the pillars goes down to 0.405, representing 1.41% of the average diameter of the pillars.

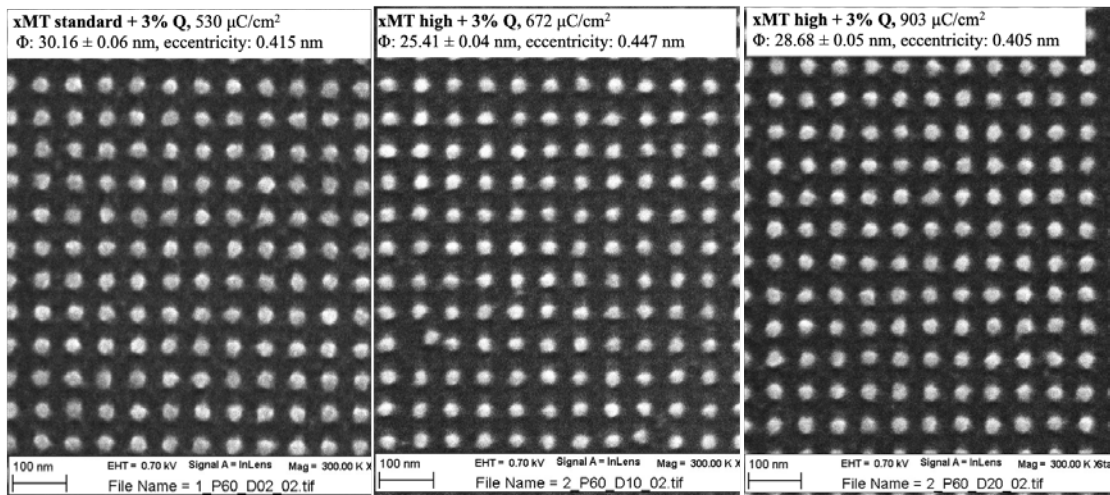

FIGURE 3.7: SEM images of xMT resist formulations : standard and high resin ratio with 3% quencher added.

As well as pillars, holes patterns were also patterned in the xMT resist as shown in 3.8. Holes are obtained by overlapping orthogonal sets of line patterns at various pitches. The right combination of pitch size and dose can be found where the proximity effect in EBL contributes to the exposure of the corners of the squares and circular holes can be obtained. Due to the fact that xMT is a negative tone resist and the measured area is the un-exposed area, the relationship CD vs dose, (where CD is the hole size in this case) takes the opposite relationship to normal (ie higher dose = smaller hole) and thus can not be directly compared to dose vs

CD relationships for pillars or lines. The roughness of the holes was analysed in SuMMIT and the high resin patterned at 855.6 μC/cm^2 showed a value of 4.72 ± 0.06 nm whereas the standard formulation shows 5.33 ± 0.07 nm roughness.

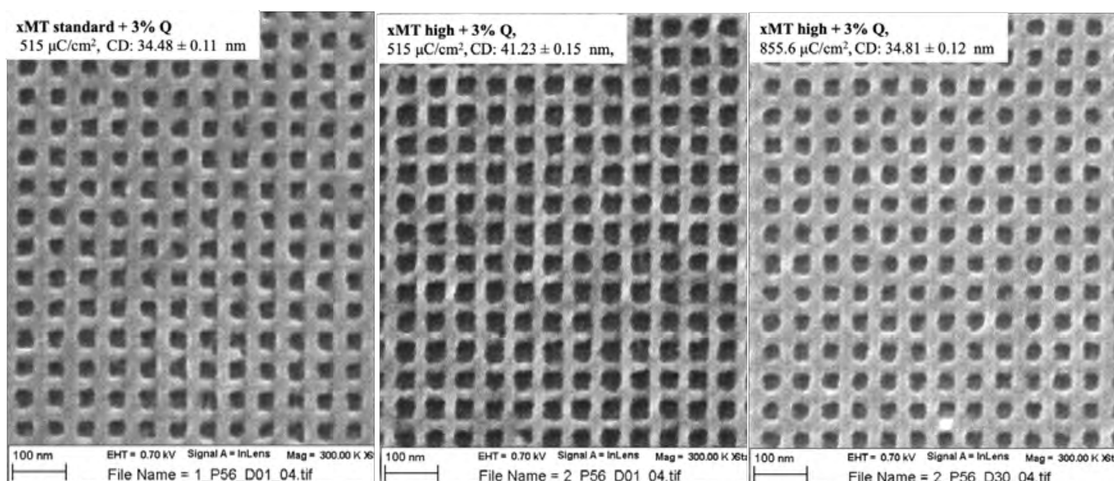

FIGURE 3.8: SEM images of xMT resist standard and high resin formulations with 3% quencher added.CD in this case is the size of the non-exposed hole in between the patterned grating

Investigating the two ratios of the resin in xMT system, showed that whilst the dose required to pattern a specific size of a given feature (line, pillar, hole) increased with the amount of resin, the roughness of the features patterned decreased when xMT high resin ratio was used.

3.3 Enhanced xMT: EX2 and EX3

In the process of optimising the xMT resist system, besides formulation changes, the chemical structure of the xMT molecule itself can also be altered in the interest of better lithographic performance. In that respect in this section two variants of the xMT molecule will be investigated. The EX2 variant is synthesised with two double bonds in the malonate chain compared to xMT and is designed to increase the stiffness of the chain and thus reduce the LER in the patterned structures. The EX3 variant also has the two double bonds, but additionally has two more

cross-linking sites compared to xMT and EX2 and is designed to demonstrate higher sensitivity as well as reduced LER. The two molecules are shown in figure 3.9.

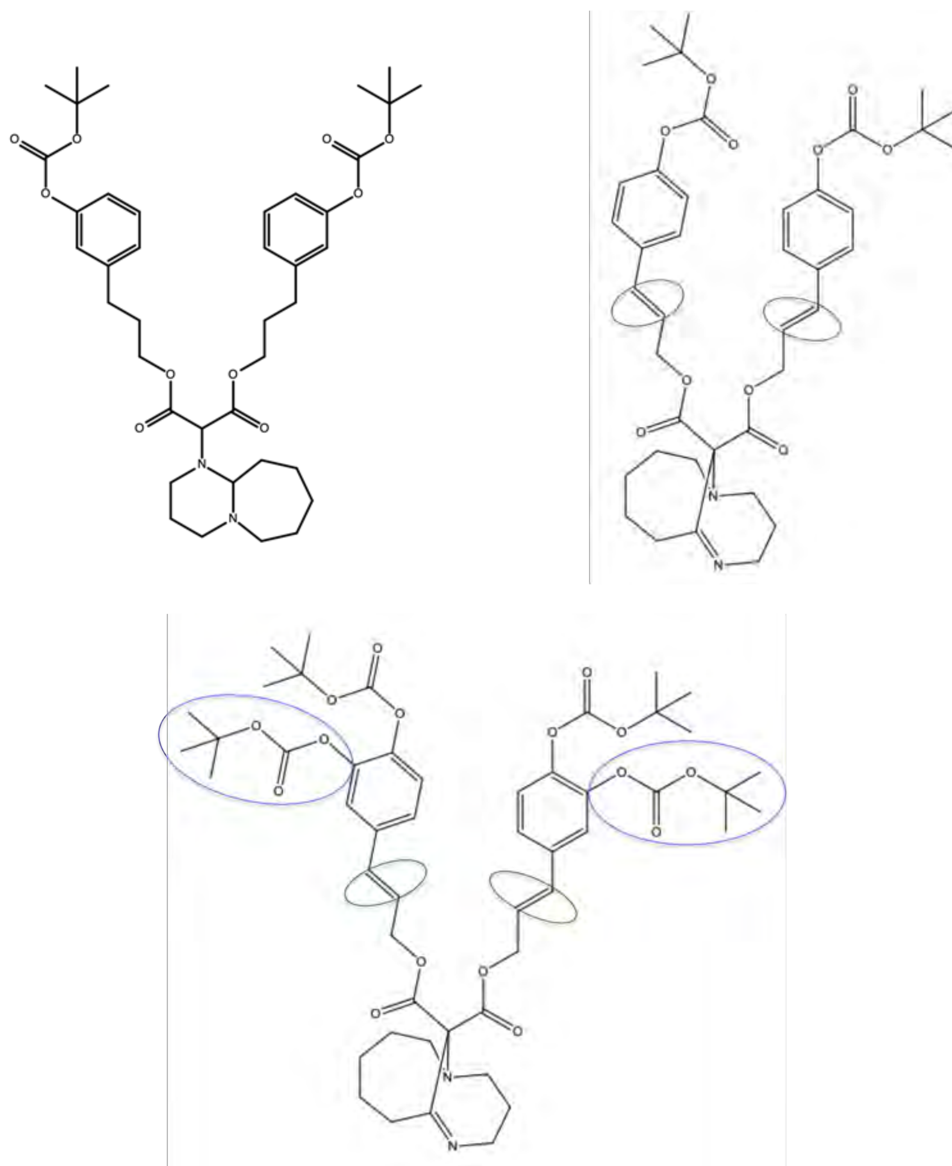

FIGURE 3.9: Chemical structure of the enhanced xMT resin. Top left: xMT molecule; top right: EX2 synthesised with a double bond on the chain to increase its mechanical strength; bottom: EX3 contains the double bond and two more t-BOC groups for improved cross-linking capability

EUV-IL experiments were conducted using EX2 and EX3 in comparison with xMT and figure 3.10 shows SEM images of the 32 nm pitch lines patterned on the 3 resist materials in comparison. The analysis of these images showed that the sensitivity

of the resist is not improved when using the two enhanced molecules. Moreover, the dose required to pattern 32 nm pitch dense lines is 23.5% higher for EX2 and 50% higher for EX3 compared to the dose required to pattern xMT. However, the LER decreases by 2% in the EX2 formulation and by 3% in the EX3 formulation.

Key to frame colour - will be used throughout when comparing performance of different materials: blue - most sensitive material, green - lowest roughness material and for pillars, the orange frame will show the best eccentricity material.

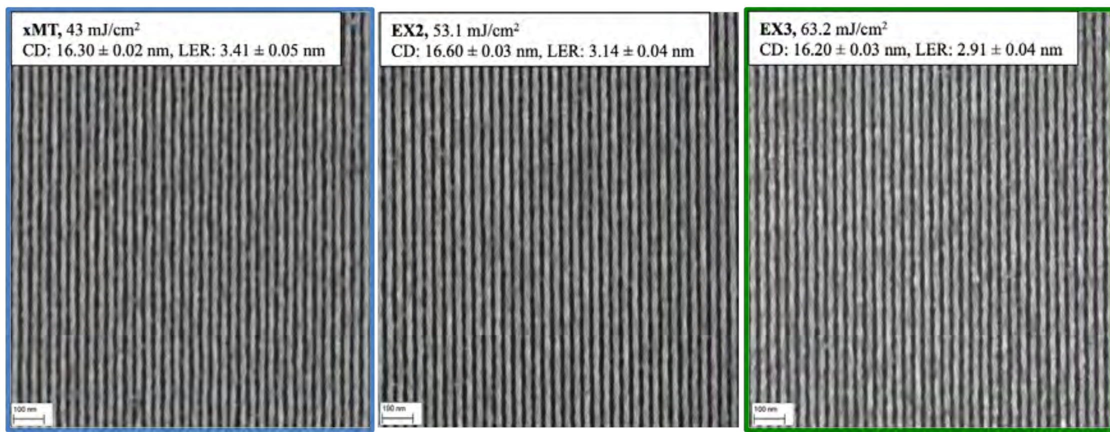

FIGURE 3.10: SEM images of dense lines at 32 nm pitch size patterned with EUV-IL on xMT, EX2 and EX3 resist formulations.

Resin	**Dose (mJ/cm^2)**	**CD (nm)**	**LER (nm)**	**LER %**
xMT	**43 ± 2.2**	16.30 ± 0.02	3.41 ± 0.05	20.92 ± 0.43
EX2	53.1 ± 2.7	16.60 ± 0.03	3.14 ± 0.04	18.92 ± 0.42
EX3	63.2 ± 3.2	16.20 ± 0.03	2.91 ± 0.04	**17.96 ± 0.43**

TABLE 3.2: Dose, CD and LER of 32 nm pitch dense lines patterned on xMT, EX2 and EX3 with EUV-IL

Analysing the LER values it is always difficult to compare between two LER values shown by different materials at similar but not identical CD values. The difference between 16.30 ± 0.03 nm and 16.60 ± 0.02 nm might seem very small but the dose deposited in the material to obtain these two features is different. EX2 received 10 mJ/cm^2 more than the xMT to obtain lines which are only 0.3 ± 0.03 nm

wider. However that additional 10 mJ/cm^2 represents ∼ 4193 more photons in the volume of a 16 nm line, which is going to reduce significantly the photon shot noise. The previous values are obtained using calculations used by [120–122].

The same applies for the EX3 resist, which receives an additional 20 mJ/cm^2 over xMT. Although 2% and 3% change in the LER value might not seem significant, these changes do show a significant reduction of 0.50 ± 0.05 nm in the LER of features of very similar sizes 16.30 ± 0.02 nm and 16.60 ± 0.03 nm.

EBL results show that for pillars (presented in figure 3.11) the EX2 resist is more sensitive than the xMT and EX3 resists. The lowest LER is demonstrated by the xMT resist but the best eccentricity is exhibited by the EX3 resist.

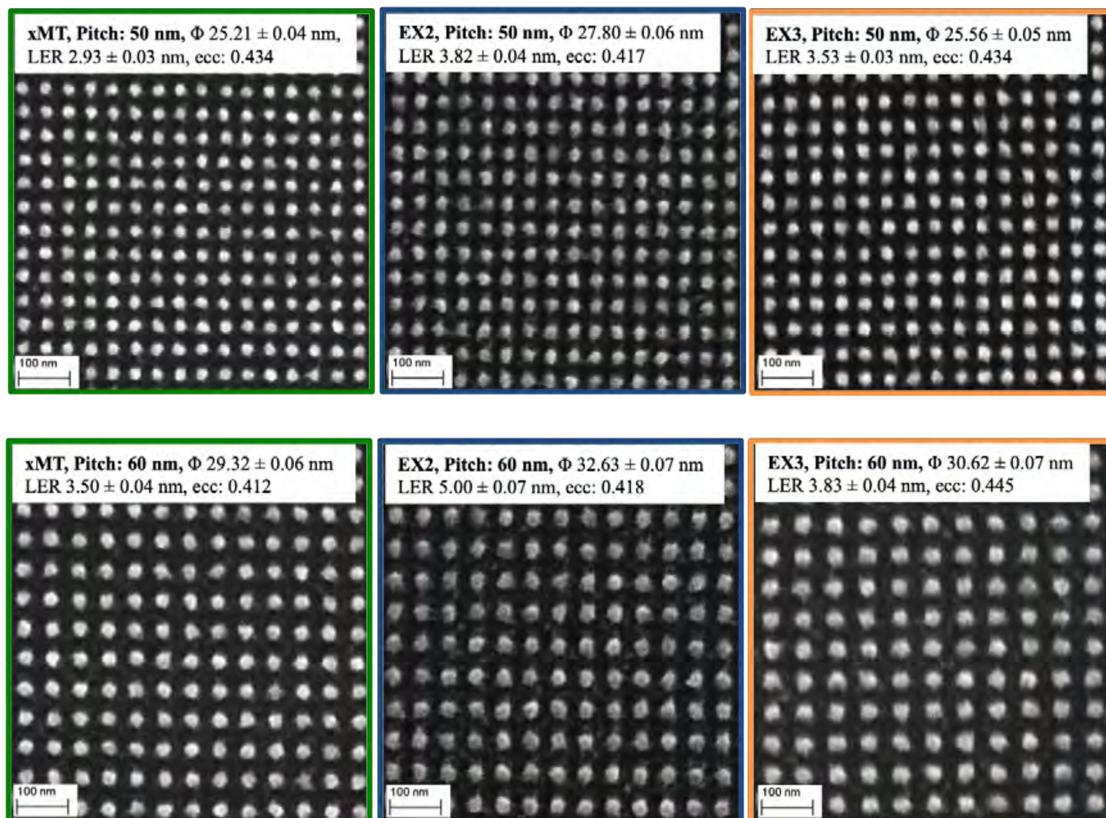

FIGURE 3.11: SEM images of pillars on 50 nm and 60 nm pitch patterned with EBL at 100 kV on xMT, EX2 and EX3 resist formulations. Dose is 515 μC/cm^2.

For both pitch sizes, 50 nm and 60 nm it can be seen in table 3.3 that the sensitivity of the EX2 resist is superior to EX3 and xMT. At pitch 50 the same exposure dose

will render pillars with an average diameter which on EX2 is 10.3% larger than on xMT and 8.8% larger than on EX3. At pitch 60, the average diameter of pillars on EX2 is 11.3% larger than the ones on xMT and 6.6% larger than the ones patterned on EX3.

Resin	ϕ **(nm)**	**LER (nm)**	**LER %**	**Eccentricity**	**Eccentricity%**
P 50 nm					
xMT	25.21 ± 0.04	2.93 ± 0.03	**11.62 ± 0.12**	0.434	1.72 ± 0.16
EX2	**27.80 ± 0.06**	3.82 ± 0.04	13.74 ± 0.15	0.445	**1.6 ± 0.22**
EX3	25.56 ± 0.05	3.53 ± 0.03	13.81 ± 0.12	0.434	1.69 ± 0.20
P 60 nm					
xMT	29.32± 0.06	3.50 ± 0.04	**11.94 ± 0.14**	0.412	1.41 ± 0.21
EX2	**32.63 ± 0.07**	5.00 ± 0.07	15.32 ± 0.22	0.418	**1.28 ± 0.22**
EX3	30.62 ± 0.07	3.53 ± 0.04	11.53 ± 0.13	0.417	1.45 ± 0.23

TABLE 3.3: Diameter (ϕ), LER and Eccentricity of pillars at 50 nm and 60 nm pitch patterned on xMT, EX2 and EX3 with EBL

The eccentricity of the pillars decreases with the diameter and is minimum for the EX2 resist with a value of 0.418 at 32.63 ± 0.07 nm diameter and 0.445 at 27.80 ± 0.06 nm. The xMT and the EX3 have similar eccentricity values for pillars with an average diameter of ∼ 25 nm and ∼ 30 nm.

This set of experiments showed that small changes in the resin structure have a notable effect on the lithographic performance of the resist formulation with effects on sensitivity and line edge roughness. The performance of the resist formulations is different from lines to pillars and from EUV-IL to EBL. Hence, for lines patterned with EUV-IL the xMT is the most sensitive material, but the lowest LER is given by the EX3. On the other hand, for pillars patterned with EBL EX2 is the most sensitive material and shows the best eccentricity but the lowest LER is exhibited by the xMT. Therefore, when choosing the resist to use for a given application these results should be taken into consideration.

3.4 Metal Hybrids

Metal-based resists are currently receiving much attention. Metals often have a higher absorption at 13.5 nm wavelength radiation compared to organic resist materials, primarily due to their higher Z number [123]. Figure 3.12 adapted from [124] shows the different atomic absorption cross-sections for elements in the periodic table plotted against Z-number.

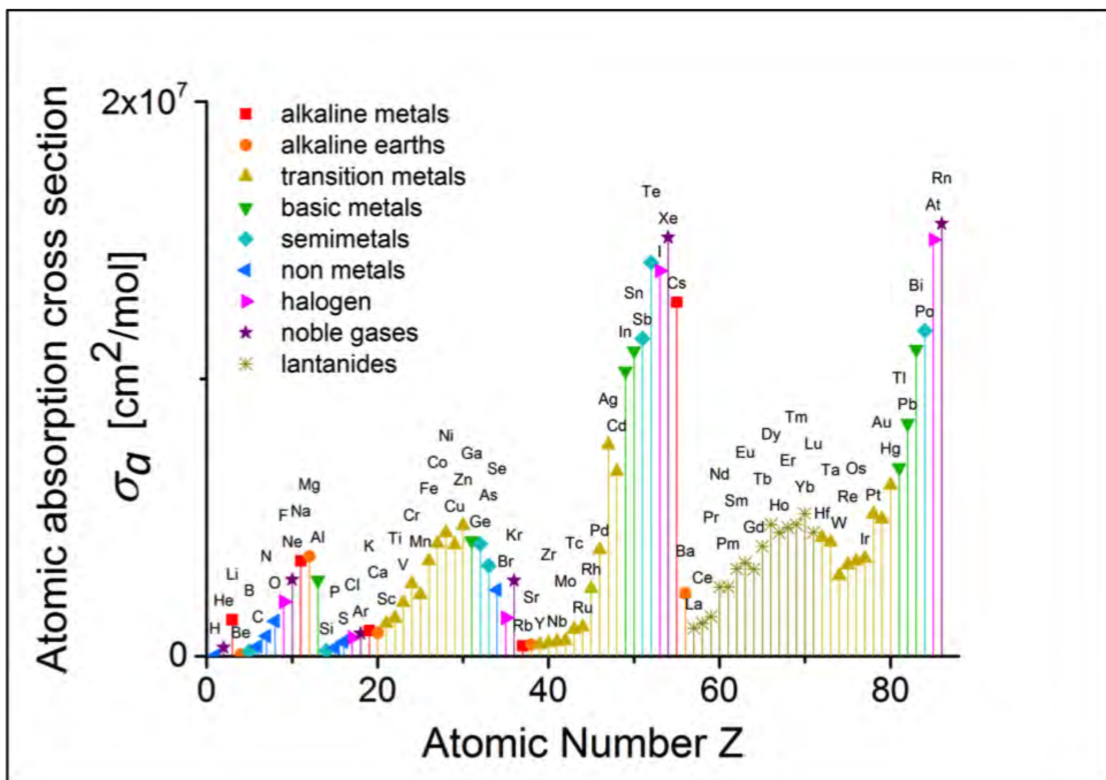

FIGURE 3.12: Atomic absorption cross-section as a function of the atomic number of the element, from [124]

Increased photo-absorption is a possible strategy to overcome the photon shot noise limit in EUV lithography as well as to significantly improve sensitivity to enable high volume manufacturing. However, it is not just the high absorption that drives lithographers attention towards metals. High-Z elements exhibit electron scattering properties, which are important in the interaction between EUV photons

and resist materials. Therefore, hybrid resists were created by blending high-Z additives into standard formulations of xMT, EX2 and EX3. The change in sensitivity was monitored and the effect on the roughness of the features was investigated.

Several metal containing molecules and coordination complexes were introduced into the resist formulations. SnI_2 added to the resist formulations in concentrations of 1% and 2% and its influence on the sensitivity in EUV lithography was analysed. Figure 3.13 shows the images obtained when adding 1% SnI_2 to xMT in comparison to the standard resist formulation.

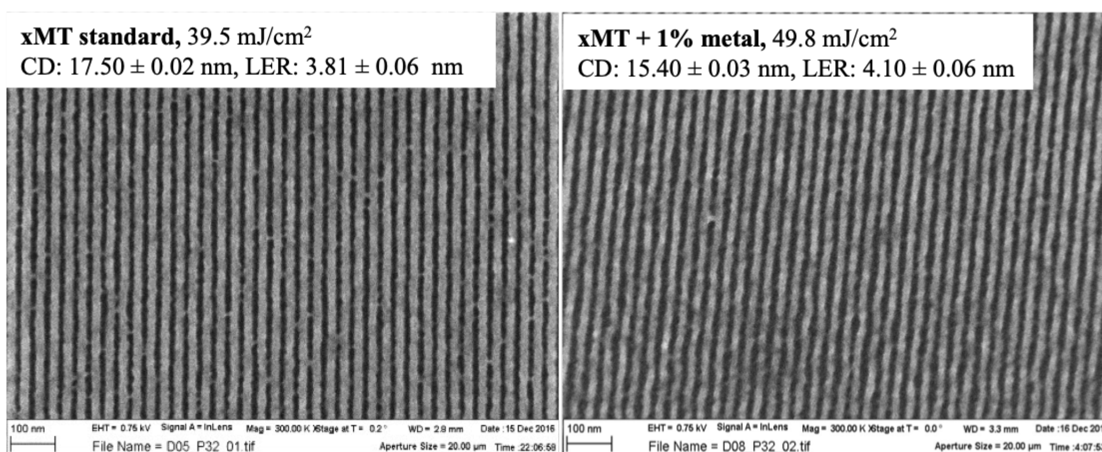

FIGURE 3.13: SEM images of dense lines at 32 nm pitch size patterned in EUV-IL on xMT resist standard formulation (left) and metal complex added formulation

The expected sensitivity increment is not observed, instead a 42.92% dose increase is required to pattern the same CD. This could be an indication that the SnI_2 is interfering in an unfavourable way with the chemistry of the resist mechanism. Since the chemistry of the exposure mechanism is not different between xMT, EX2 and EX3 systems it is expected that all three systems will show the same reaction to the addition of SnI_2.

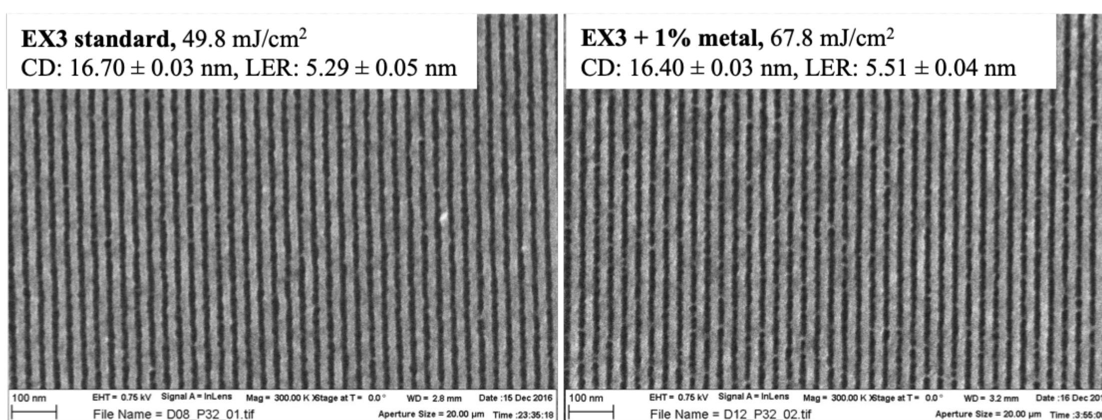

FIGURE 3.14: SEM images of dense lines at 32 nm pitch size patterned in EUV-IL on EX3 resist standard formulation (left), and metal complex added formulation (right)

When added to the EX3 formulation, it is observed again that there is no boost in the sensitivity and a significant increase in the LER occurs as can be seen in figure 3.14.

The addition of SnI_2 makes the formulation 38.64% less sensitive to EUV. Furthermore the LER increases by 3.68% on features patterned using the formulation that contains 1% SnI_2. Figure 3.15 summarises the effect the metal complex addition has on the xMT and EX3 resists.

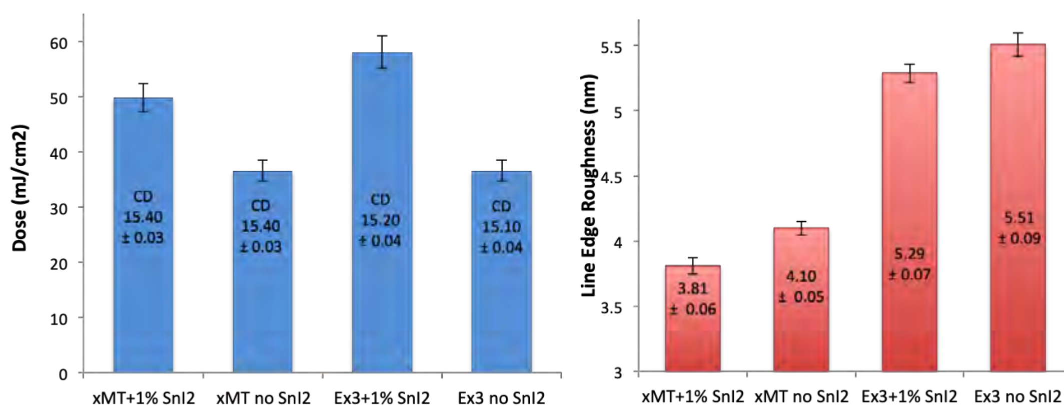

FIGURE 3.15: Comparison of dose required by xMT and EX3 and the metal hybrids to pattern 32 nm pitch dense lines with EUV and LER value obtained

For EX2 the number of Sn and I_2 atoms added was varied in two experiments in order to observe the effect. In the first experiment the EX2 formulation contains

2.5% quencher and 1% of SnI_2 is added. The lithography results are shown in the figure below.

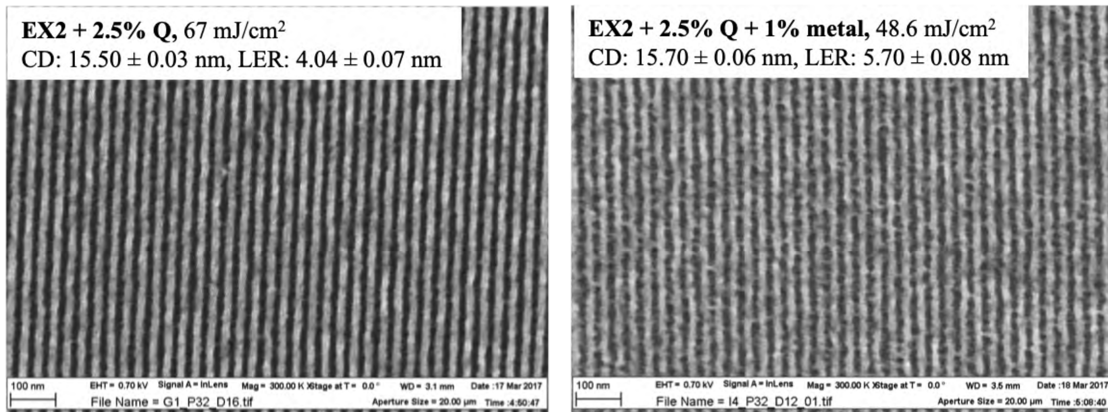

Figure 3.16: SEM images of dense lines at 32 nm pitch size patterned in EUV-IL on EX2 + 2.5% quencher resist formulation (left), and metal complex added formulation (right)

The LER values measured on images from figure 3.16 show that the sensitivity of EX2 resist with 2.5% Q is increased by 28.39% when 1% SnI_2 is added to the formulation. The LER, however is increasing by 10.24%.

The EX2 formulation used in the second experiment contains 3% quencher added to improve the resolution.

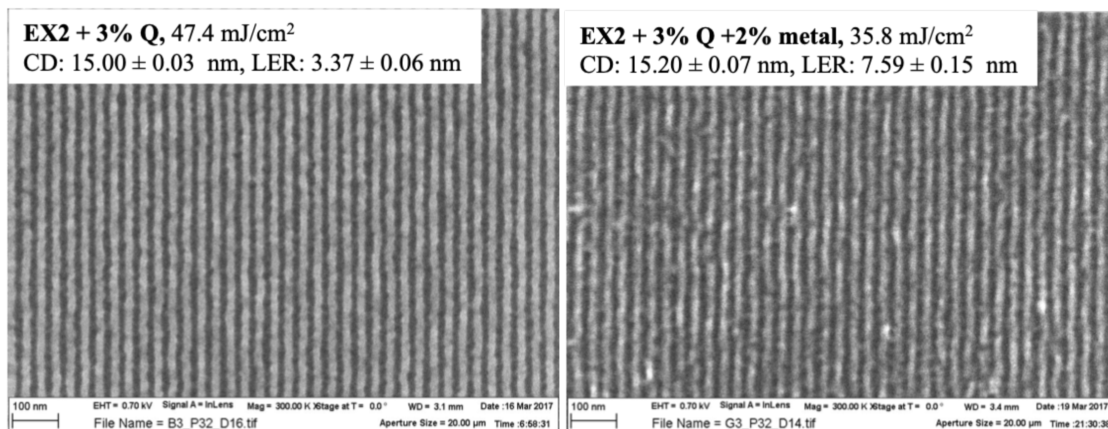

Figure 3.17: SEM images of dense lines at 32 nm pitch size patterned in EUV-IL on EX2 + 3% quencher resist formulation (left), and metal complex added formulation (right)

The addition of 2% SnI_2 introduced in this formulation increased the sensitivity of the material by 25.47% but a significant degradation of the LER is observed with a value that is 2.25 times larger for the metal hybrid EX2 resist. This shows that the SnI_2 blended in the resist formulation is stopping the quencher molecules from reacting with the resist matrix and reduce the diffusion length of the photo-acid. Therefore the sensitivity will improve but the roughness will increase significantly since the spatial distribution of the metal atoms in the solution is unknown and random.

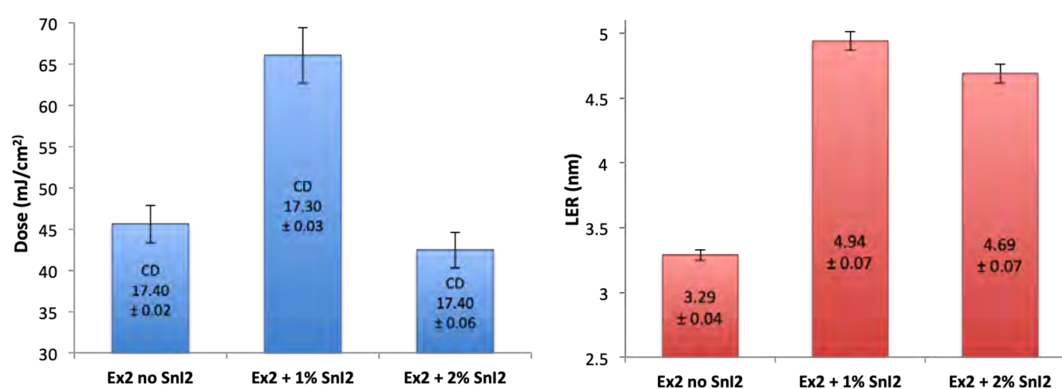

FIGURE 3.18: Dose and LER for 32 nm pitch size on EX2 + 3% quencher resist formulation and metal complex added formulations

In order to evaluate whether the change in sensitivity takes place in the EX2 only, a new EX3 formulation was used in the next experiment, where the EX3 resin went through a metal ion removal process and the resist formulation contains 3% Q and 2% SnI_2. Figure 3.19 shows the SEM images of the 32 nm pitch dense lines obtained on this formulation in comparison to the same formulation with no SnI_2 added.

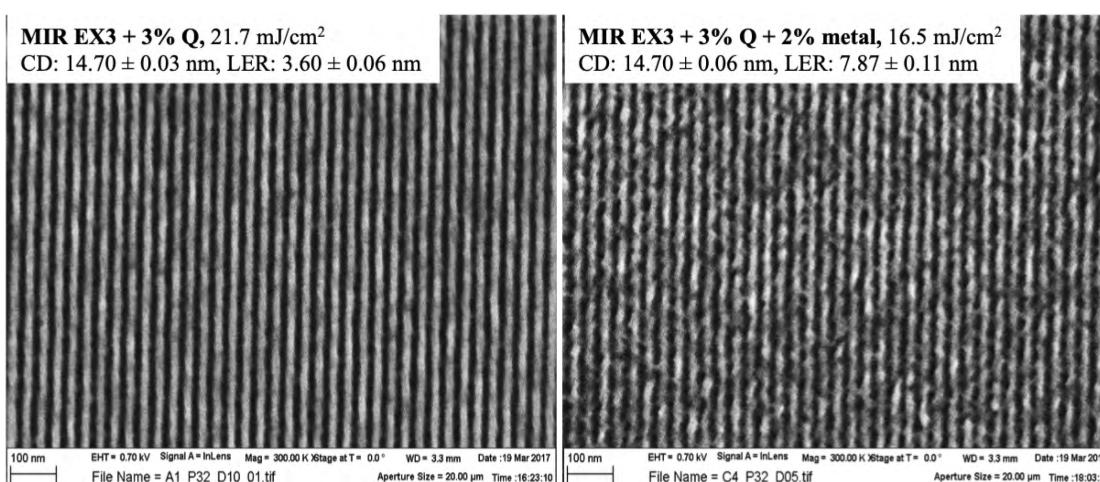

FIGURE 3.19: SEM images of dense lines at 32 nm pitch patterned on MIR EX3 resit formulation with 3% Q (left) and 2% SnI_2 added (right)

Similarly to the EX2 resist a sensitivity improvement of 32% is obtained by adding 2% SnI_2 in the MIR EX3 formulation containing 3% Q. The images of lines at 32 nm pitch patterned on MIR EX3 formulation with and without the metal added can be seen in figure 3.19. The LER degradation is by a factor 2.2 when the metal complex is added to the MIR EX3 resist. Therefore the addition of SnI_2 has the same effect on all three resist systems evaluated in this experiment. When quencher is not present in the formulation, the sensitivity is not improved by the metal addition and the LER is significantly increased. When quencher is present in the system a boost in sensitivity can be observed but the LER is again dramatically worsened by a factor of 2.2.

In electron beam the xMT and EX3 resists were evaluated in comparison and lines and pillars were patterned on formulations containing 3% Q and the images analysed in Summit. Figure 3.20 shows pillars patterned at 50 nm pitch and 350 μC/cm^2.

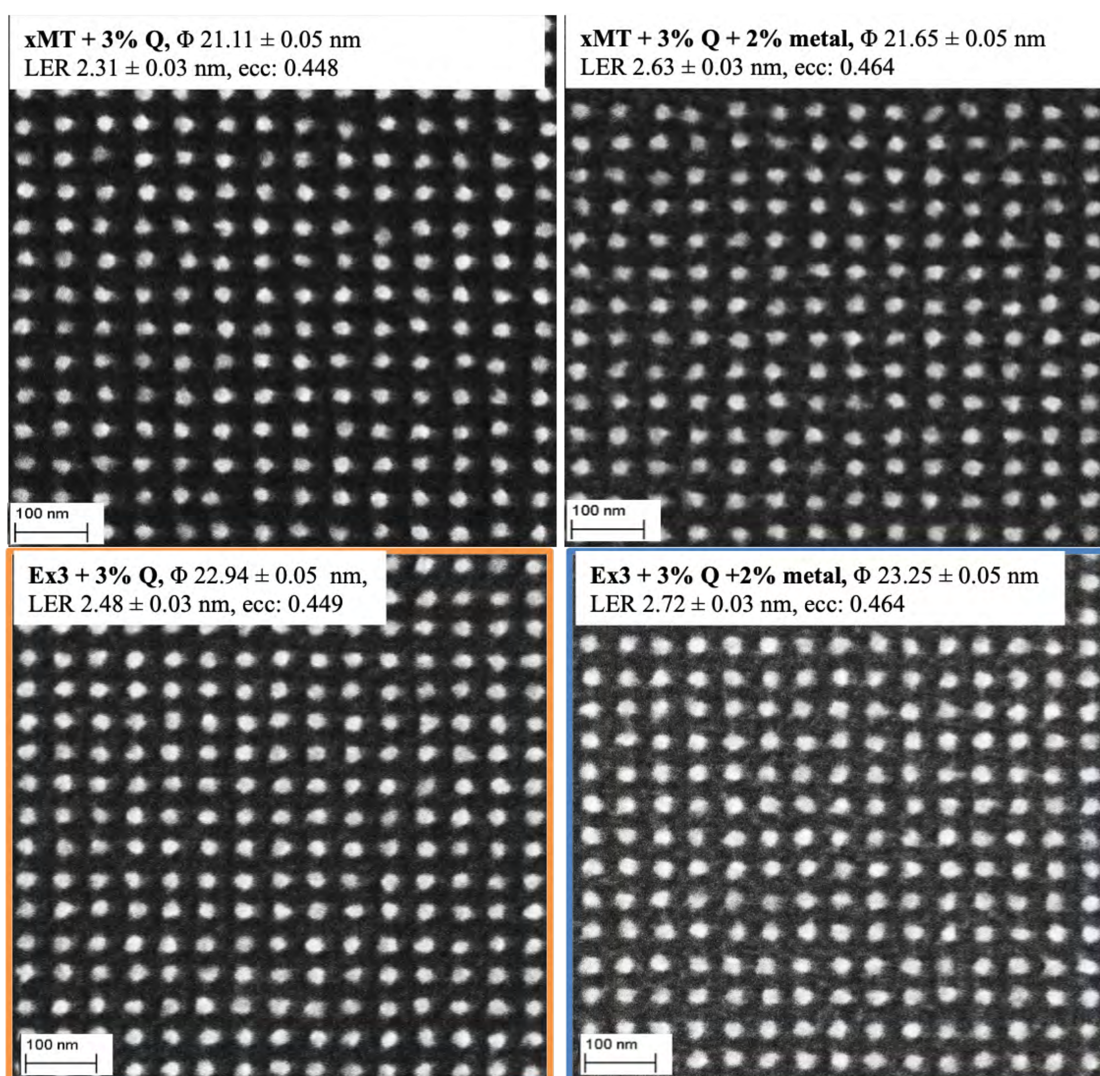

FIGURE 3.20: SEM images of pillars at 50 nm pitch patterned with EBL on xMT and EX3 resit formulation with 3% quencher and with 2% SnI_2 added. Dose is 350 μC/cm^2

Analysing the data shown in the above figure, it was concluded that the EX3 is more sensitive than the xMT, and patterns pillars with an average diameter 8.7% larger than the xMT at the same dose. However this sensitivity is increased further by 1.35 % with addition of the metal complex. The xMT formulation is also sensitised when metal is added by 2.6%. In terms of pillar uniformity, the best formulation to render pillars is the EX3 without metal with an eccentricity value of 1.95% of the critical dimension patterned. When metal is added the EX3 still outperforms both the standard xMT and the metal added xMT formulations with

a value of 1.9% as opposed to 2.12% and 2.14%. Therefore, EX3 + 3% Q loading looks like the best resist formulation to pattern pillars with in Ebeam lithography at 100 keV.

Dense lines at 36 nm pitch were also patterned with 100 keV electron beam and are shown in figure 3.21.

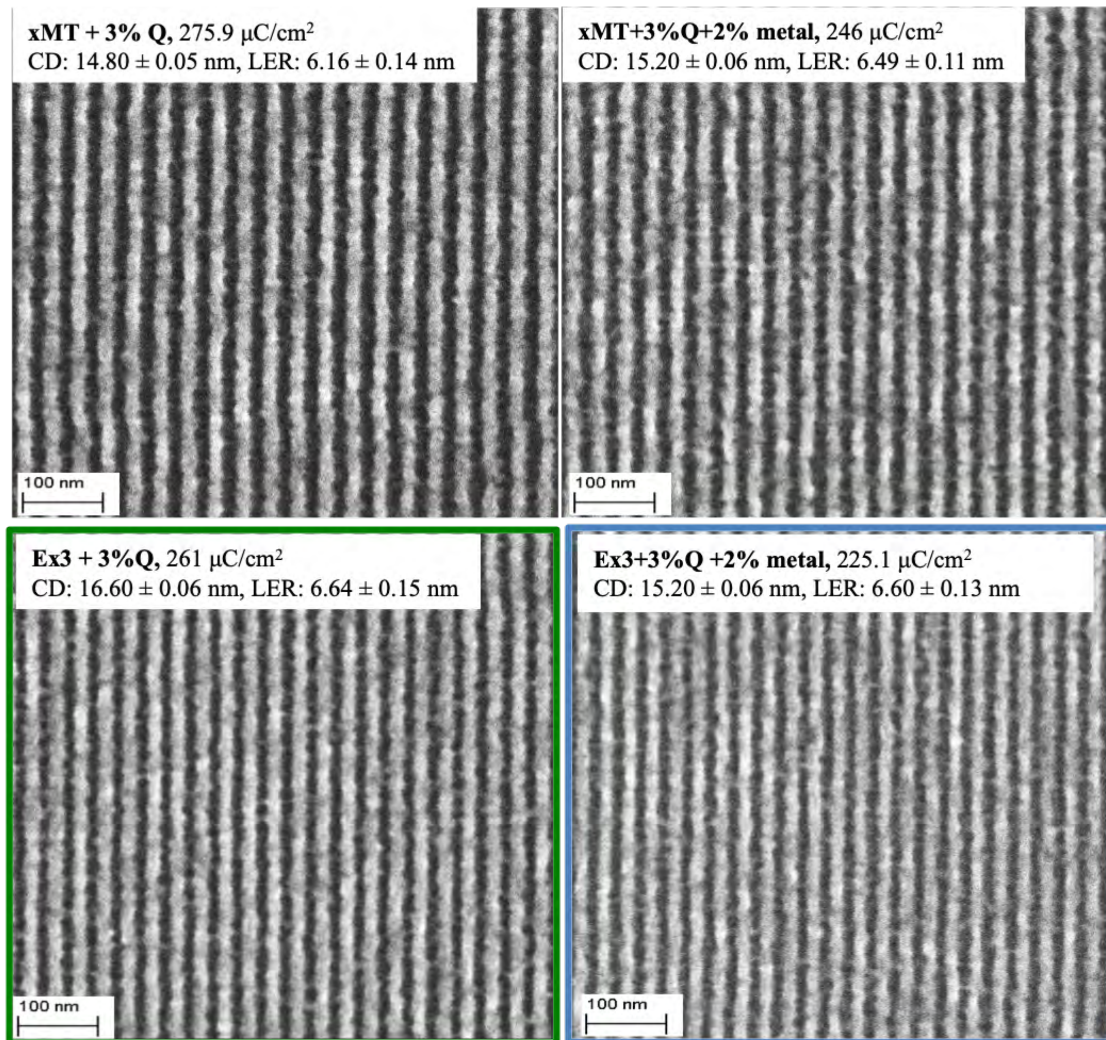

Figure 3.21: SEM images of dense lines at 32 nm pitch patterned with EBL on xMT and EX3 resit formulations with 3% quencher and with 2% SnI_2 added.

Analysis of the results above showed that when adding metal to the resist both xMT and EX3 become more sensitive than the standard version. Moreover, metal hybrid EX3 formulation is 9.3% more sensitive than metal hybrid xMT formulation. The best LER is shown on the lines patterned on EX3 without metal with

a value of 40% of CD of 16.6 nm. Table 3.4 summarises the lithographic performance of the four formulations evaluated in this experiment. Just as in the case of pillars, in terms of dose required and LER the best formulation to pattern lines with 100 keV electron beam is the EX3 formulation with 3% Q without metal added.

Resin	Dose(μC/cm^2)	CD (nm)	LER (nm)	LER %
xMT	276.85 ± 5.54	14.80 ± 0.05	6.16 ± 0.14	41.62 ± 0.94
xMT + SnI_2	246 ± 4.92	15.20 ± 0.06	6.49 ± 0.11	42.70 ± 0.73
EX3	261 ± 5.22	16.60 ± 0.06	6.64 ± 0.15	**40.00 ± 0.91**
EX3 + SnI_2	**225.10 ± 4.51**	15.20 ± 0.06	6.60 ± 0.13	43.42 ± 0.86

TABLE 3.4: Dose, CD and LER of lines at 36 nm pitch patterned on xMT, EX3 and corresponding metal hybrid formulations with EBL

Figure 3.22 demonstrates alternative structures such as isolated lines and elbows patterned with EBL on xMT and EX3 formulations with and without metal. The measured CD and LER are listed in the caption of the figure but they will not be discussed in comparison as the magnification of the analysed images was different.

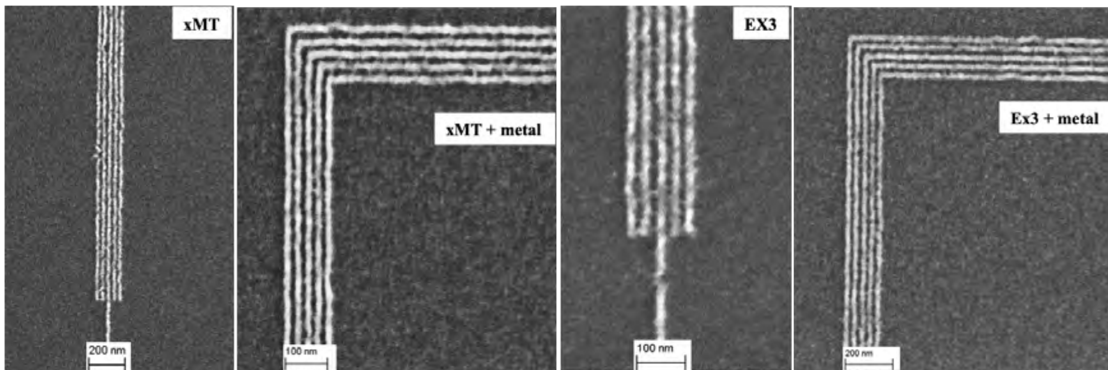

FIGURE 3.22: SEM images of lines and ellbows patterned with EBL on xMT and EX3 resit formulation with 3% Q and with 2% SnI_2 added.

3.5 Metal Ion Removed Resist

After synthesis metal contaminants can be present in the resist formulations and they can interfere with the exposure mechanism. In this section a comparison between results obtained using standard resist formulation and formulation that has received metal ions removal purification treatment is presented.

Metal ion reduction of the xMT base molecule and the xMT + crosslinker solution was undertaken by Irresistible Materials and their partner Nano-C Inc. This was done by passing the formulation through a 3M Zeta Plus 4OQ membrane six times. The ionic PAG and quencher were incompatible with this process, so were purchased certified clean, and added to formulation after. Figure 3.23 shows an example of data on the metal levels before and after metal ion removal process. Note that the symbol " $<$" indicates below detection limit, with the following number indicating the limit. In the past purification samples, a larger quantity of formulation was used to improve the detection limits.

Metal ion contamination levels were measured by sending samples of the formulated resist to a semiconductor industry certified testing laboratory (Chem Trace) where inductively coupled plasma mass spectrometry (ICP-MS) was used to evaluate the samples.

Contaminant	Pre-Purification (ppb)	Post-Purification (ppb)
Aluminum (Al)	30	10
Barium (Ba)	< 10	< 1
Beryllium (Be)	< 10	< 5
Bismuth (Bi)	< 10	< 5
Cadmium (Cd)	< 10	< 1
Calcium (Ca)	125	6.5
Chromium (Cr)	339	3.5
Cobalt (Co)	< 10	< 1
Copper (Cu)	< 10	< 5
Gallium (Ga)	< 10	< 1
Iron (Fe)	< 10	39
Lead (Pb)	< 10	< 1
Lithium (Li)	< 10	< 1
Magnesium (Mg)	507	4.3
Manganese (Mn)	< 10	< 1
Molybdenum (Mo)	< 10	< 1
Nickel (Ni)	< 10	< 5
Potassium (K)	21	< 20
Sodium (Na)	1040	21
Strontium (Sr)	< 10	< 1
Thallium (Tl)	< 10	< 5
Tin (Sn)	< 10	< 1
Titanium (Ti)	< 10	3.8
Zinc (Zn)	38	5.2
Zirconium (Zr)	< 10	< 1

Figure 3.23: Example of metal levels detected before and after metal ion removal purification process

EUV-IL results show that the MIR formulation of xMT is 18% more sensitive than the non-MIR formulation. However, the LER is 3% larger in the MIR formulation increasing from 4.62 ± 0.05 nm for CD 16.30 ± 0.04 nm to 4.92 ± 0.08 nm for CD 16.00 ± 0.05 nm. Figure 3.24 shows the SEM images of the patterned features on the standard xMT and MIR xMT.

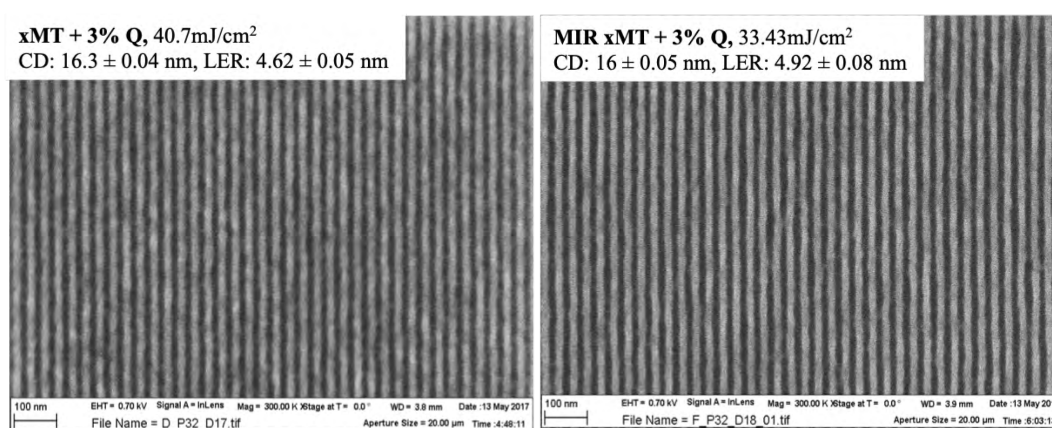

Figure 3.24: SEM images of dense lines at 32 nm pitch size patterned in EUV-IL on non-MIR and MIR xMT formulation

EX2 behaves similarly to xMT when metal ions are removed from the resist formulation. Figure 3.25 demonstrates SEM images of 32 nm pitch dense lines patterned in EUV-IL and shows an increase in the sensitivity of the MIR formulation by 55%. The LER on the other hand increased by 10.5% of CD from 3.37 ± 0.06 nm to 4.95 ± 0.06 nm for 15.00 ± 0.03 nm CD.

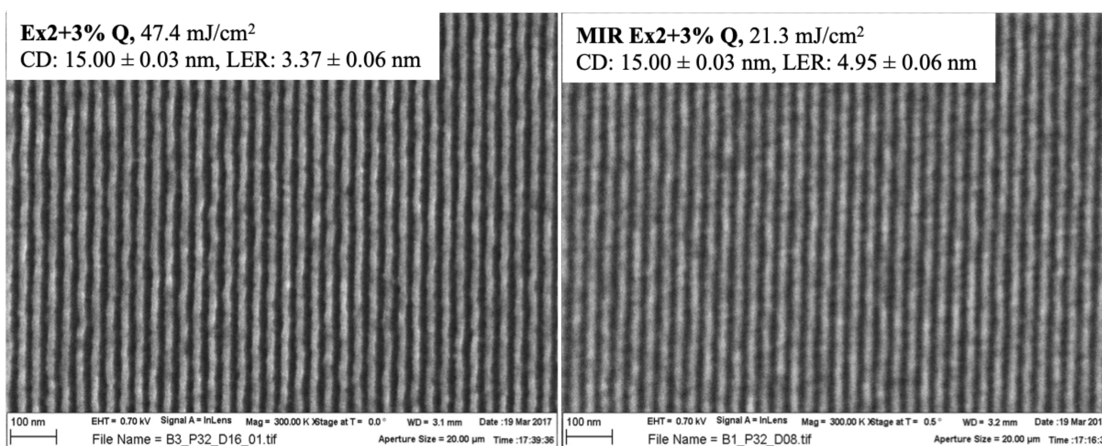

Figure 3.25: SEM images of dense lines at 32 nm pitch size patterned in EUV-IL on non-MIR and MIR EX2 formulation

However, it should be taken into account that the MIR EX2 SEM image is of slightly worse quality than the EX2 SEM image, which contributes to the higher LER value. Unfortunately, a better image could not have been obtained at the time of the experiment due to the instability of the electron beam in the SEM.

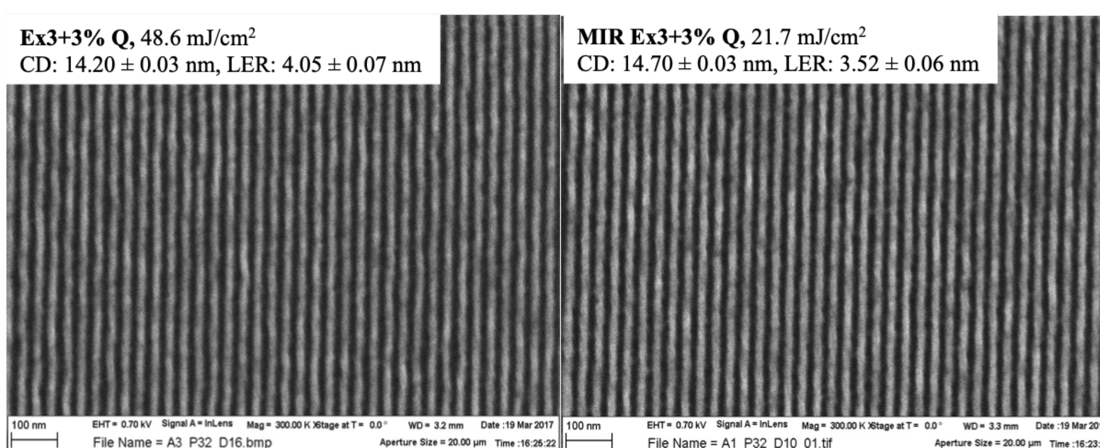

FIGURE 3.26: SEM images of dense lines at 32 nm pitch size patterned in EUV-IL on non-MIR (left) and MIR EX3 (right) formulations

When using the EX3 resist, the MIR formulation shows a higher sensitivity than the non-MIR formulation as observed in the first two resists. The dose required to pattern MIR EX3 is 55.3% lower than the dose required for patterning non-MIR EX3. The LER on the other hand is improved in the MIR EX3 by 4.6% from 4.05 ± 0.07 nm for 14.20 ± 0.03 nm CD to 3.52 ± 0.06 nm for 14.70 ± 0.03 nm CD. Figure 3.26 shows the SEM images of the dense lines patterned on the EX3 and MIR EX3 resist formulations.

Resin	**Change in Sensitivity**	**Change in LER**
xMT	+16.32 ± 1.66%	+2.41 ± 0.97 %
EX2	+55.06 ± 1.45%	+10.53 ± 0.45%
EX3	+55.35 ± 1.45%	-4.58 ± 1.01 %

TABLE 3.5: MIR vs non-MIR formulations - Change in Sensitivity and LER

MIR filtration affects all three resins in the same fashion as far as the sensitivity parameter is concerned which increases in all three resists with a boost of 55% in EX3. The LER on the other hand increases in xMT and EX2 but decreases by 4.6% in EX3. This can be observed in table 3.5.

3.6 Organic High-Z Compounds for Increased Optical Density

The results obtained using metal hybrid resists showed that the sensitivity of the resist increases with the addition of SnI_2. What is not clear from the analysis is whether the tin atoms or the iodine atoms contribute towards this effect. These two elements have comparable Z numbers and very similar absorption cross-sections for EUV photons and they could each or both be responsible for the increased photoabsorption of the resist and therefore the improvement of the sensitivity.

As described by De Simone et. al. in [125] this effect can only occur when the chemistry in the system is favourable and the only way to find the right additive that enhances the secondary electron response of the resist is to incorporate each individual additive and analyse the lithographic performance of the resulting materials. Since there are a number of metal containing resist (MCR), and metal oxide resists are well studied, our attention focused on the non-metal high-Z containing resist.

Therefore, presented in this section are the results obtained by blending a non-metal iodinated compound in the resist formulation. C_6H_5I was used for this study and three different cases were investigated. The first case (1) uses EX2 formulation with C_6H_5I solution added in the amount to match the number of iodine atoms to the number of iodine atoms in the 1% metal hybrid formulation.

In the second case (2) C_6H_5I was added to match the number of iodine atoms to the number of iodine and tin atoms in the 1% metal hybrid formulation. Finally, the last case (3) used C_6H_5I in the same molar ratio as the SnI_2 in the metal hybrid formulation.

Figure 3.27 shows the EUV-IL results obtained using the three formulations described above in comparison with the MIR EX2 formulation without additives.

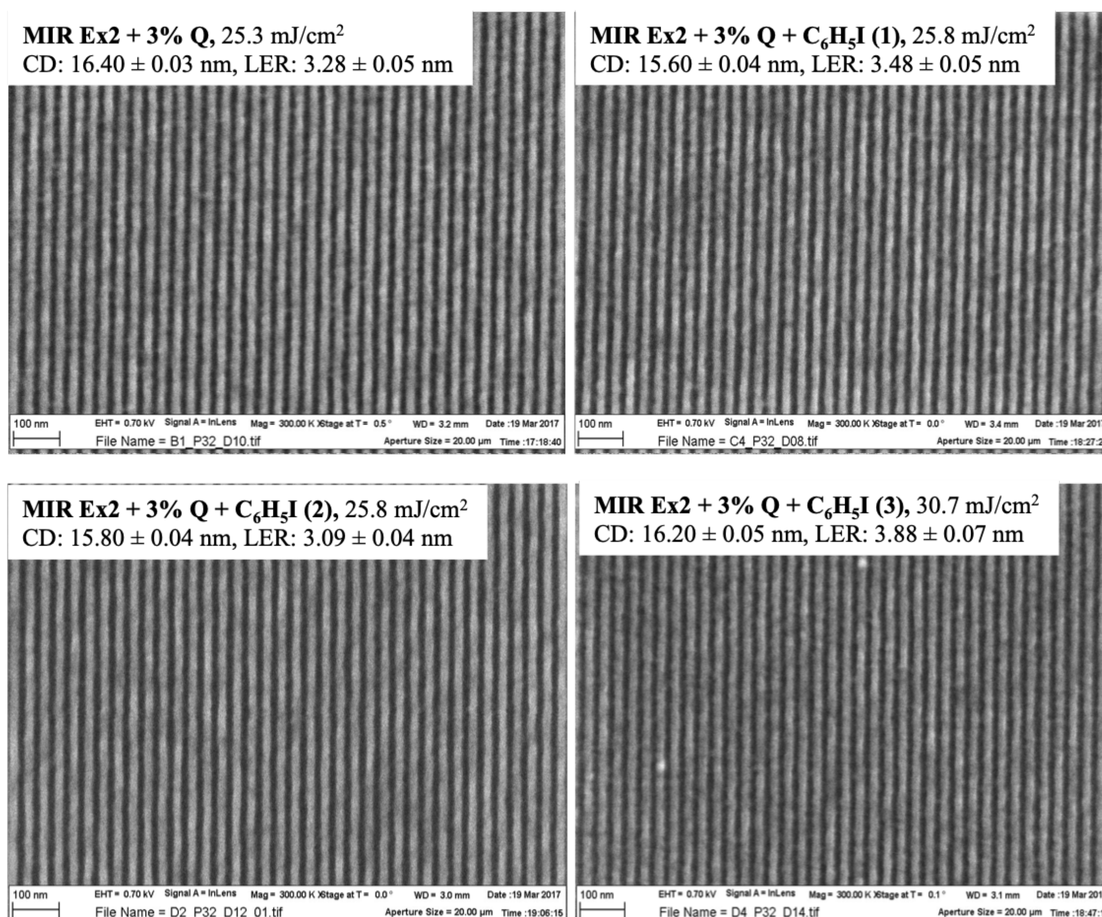

FIGURE 3.27: SEM images of dense lines at 32 nm pitch size patterned in EUV-IL on standard formulation of MIR EX2 resist and formulations containing C_6H_5I in various concentrations. (1) - number of iodine atoms from C_6H_5I match the number of iodine atoms added in metal hybrid formulation; (2) - number of iodine atoms from C_6H_5I match the number of iodine atoms plus the number of tin atoms added in metal hybrid formulation; (3) the number of C_6H_5I molecules match the number of SnI_2 molecules

From the images presented in figure 3.27 it can be observed that formulation 1 gives a slightly larger LER value and the sensitivity is lower than the standard formulation. Formulation 2, although it is also less sensitive than the standard formulation gives a smaller LER value whereas formulation 3 is even less sensitive and exhibits an even larger LER value than all the other formulations.

Table 3.6 presents the results obtained from analysing the SEM images in figure 3.27.

Sample	**Dose (mJ/cm^2)**	**CD (nm)**	**LER (nm)**
MIR EX2	25.30 ± 1.27	16.40 ± 0.03	3.28 ± 0.05
MIR EX2+C_6H_5I (1)	25.80 ± 1.29	15.60 ± 0.04	3.48 ± 0.05
MIR EX2+C_6H_5I (2)	25.80 ± 1.29	15.80 ± 0.04	3.09 ± 0.04
MIR EX2+C_6H_5I (3)	30.66 ± 1.53	16.20 ± 0.05	3.88 ± 0.07

TABLE 3.6: Dose required to pattern dense lines at 32 nm pitch size and LER obtained in EUV using MIR EX2 + C_6H_5I. (1) - number of iodine atoms from C_6H_5I match the number of iodine atoms added in metal hybrid formulation; (2) - number of iodine atoms from C_6H_5I match the number of iodine atoms plus the number of tin atoms added in metal hybrid formulation; (3) the number of C_6H_5I molecules match the number of SnI_2 molecules

The control sample in this experiment, which is the MIR EX2 resist with 3% Q loading demonstrates the highest sensitivity and unlike the case of metal hybrids there is no boost in sensitivity observed when C_6H_5I is added to the resist. The LER of 3.28 nm on the control sample represents 20% of the CD. For formulation (1), in which the volume of C_6H_5I added to the resist formulation is measured so that the iodine atoms added match the number of iodine atoms that were added in the corresponding hybrid formulation, the LER increases by 2.3%. For formulation (2), where the number of iodine atoms represent the number of iodine and tin atoms from EX2 metal hybrid, the LER decreases slightly by 0.5% to 19.5% of CD. For formulation (3), where the number of C_6H_5I added to the resist formulation is equal to the number of SnI_2 molecules in the EX2 metal hybrid, the LER increases by 3.9% compared to the control sample.

MIR EX3 was also evaluated in a similar experiment and the images obtained after patterning the control formulation and formulations that contain C_6H_5I are shown in figure 3.28.

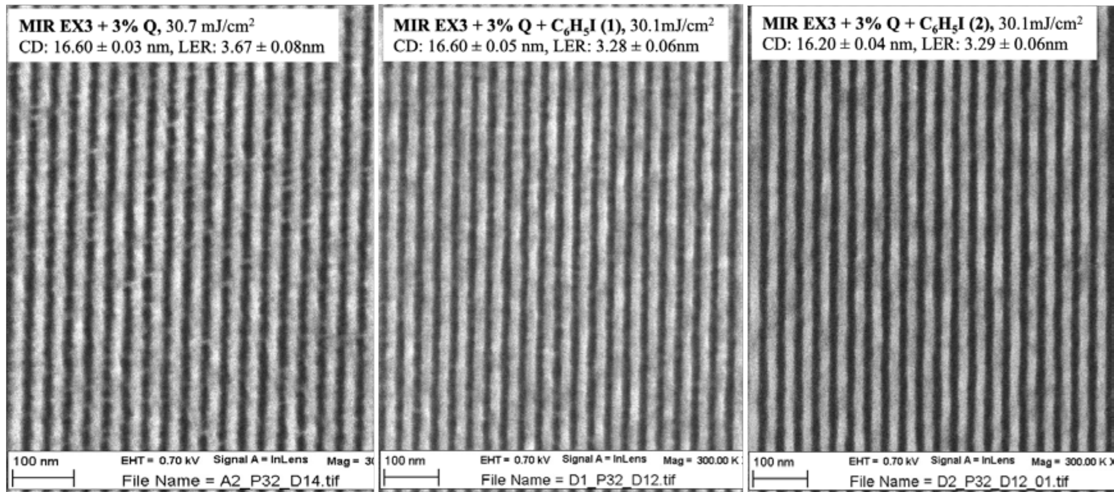

FIGURE 3.28: SEM images of dense lines at 32nm pitch size patterned in EUV-IL on MIR EX3 resist and formulations containing C_6H_5I in various concentrations. (1) - number of iodine atoms from C_6H_5I match the number of iodine atoms added in metal hybrid formulation; (2) - number of iodine atoms from C_6H_5I match the number of iodine atoms plus the number of tin atoms added in the metal hybrid formulation

The formulation containing as many molecules of C_6H_5I as SnI_2 in the metal hybrid formulation was not tested in this experiment as it was shown in the case of MIR EX2 that the sensitivity is not enhanced and a significant increase in LER will take place. Table 3.7 summarises the results obtained after analysing the SEM images on these samples.

Sample	**Dose (mJ/cm^2)**	**CD (nm)**	**LER (nm)**
MIR EX3	30.70 ± 1.54	16.60 ± 0.03	3.67 ± 0.08
MIR EX3+C_6H_5I (1)	30.10 ± 1.51	16.60 ± 0.05	3.28 ± 0.06
MIR EX3+C_6H_5I (2)	30.10 ± 1.51	16.20 ± 0.04	3.29 ± 0.06

TABLE 3.7: Dose required to pattern dense lines at 32 nm pitch size and LER obtained in EUV using MIR EX3 + C_6H_5I. (1) - number of iodine atoms from C_6H_5I match the number of iodine atoms added in metal hybrid formulation; (2) - number of iodine atoms from C_6H_5I match the number of iodine atoms plus the number of tin atoms added in the metal hybrid formulation

In the case of the MIR EX3, formulation (1) is more sensitive by 1.83% than the control sample. This is also the formulation which exhibits the lowest LER

of 18.10% of CD at CD of 16.60 ± 0.05 nm. This is 4% lower compared to the control sample. Formulation (2) is not more sensitive but it also demonstrates a LER which is lower than the control sample by 1.8% at CD 16.20 ± 0.04 nm.

Resin	**Change in Dose**	**Change in LER**
MIR EX2		
MIR EX2 + 3% Q (control)	-	-
MIR EX2+ 3% Q + C_6H_5I (1)	+ 7.20 ± 0.11%	+ 2.31 ± 0.72 %
MIR EX2+ 3% Q + C_6H_5I (2)	+ 5.85 ± 0.11%	- 0.44 ± 0.14%
MIR EX2+ 3% Q + C_6H_5I (3)	+ 22.68 ± 0.13%	+ 3.95 ± 0.84 %
MIR EX3		
MIR EX3+ 3% Q (control)	-	-
MIR EX3+ 3% Q + C_6H_5I (1)	- 1.83 ± 0.10%	- 2.35 ± 0.94%
MIR EX3+ 3% Q + C_6H_5I (2)	+ 0.59 ± 0.10%	- 1.80 ± 0.94%

TABLE 3.8: Change in sensitivity and LER in MIR EX2 and MIR EX3 when C_6H_5I is added to the resist formulation compared to the control samples

From these two experiments it is seen, that for the EX2 system the addition of organic high-Z compounds does not improve the sensitivity, but it can slightly improve the LER when added in a specific concentration (that is formulation 2). For the EX3 system, on the other hand, the addition of the organic high-Z compound has a very beneficial effect, improving the sensitivity and reducing the LER (formulation 1). As this is similar to the pattern seen for SnI_2 the conclusion that can be drawn from this experiment is that the changes in sensitivity and LER are introduced by the interaction of the iodine atoms with the EUV photons and their interference with the exposure mechanism.

3.7 Organic High-Z Cross-linker

It has been shown in the previous section that when added in a specific concentration the organic high-Z atoms can have a beneficial effect on the lithographic performance of the resist material. The next step in the process of improving the sensitivity and LER by making use of high opacity atoms is to synthesise resist components in which these atoms already are chemically bound to the structure instead of blending them in the formulation, which reduces the likelihood of them interfering with the photochemistry. Therefore, this section presents results obtained using resist formulations that contain cross-linker molecules synthesised with high-Z atoms in the molecules (by Dr. Greg O'Callaghan, Irresistible Materials Ltd). Iodine was the first choice of high-Z organic element to be introduced in the crosslinker considering the results obtained in the experiments with SnI_2 and C_6H_5I.

Figure 3.29 shows the chemical structures of the high opacity CL molecule employed in this experiment.

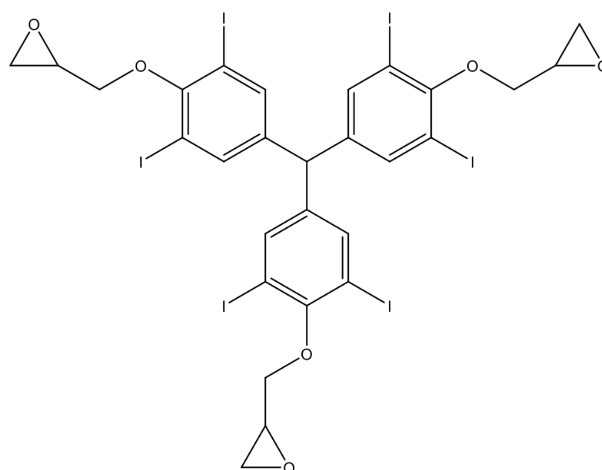

FIGURE 3.29: Chemical structure of high opacity iodinated CL molecule synthesised with 6 iodine atoms to increase its opacity and the sensitivity of the resist material

3.7.1 Iodinated Cross-linker

The resist used in these experiments is EX2 and no quencher is added to the formulation, so that the exposure mechanism is not altered by any factor other than the newly introduced iodinated cross-linker (ICL). Initial tests performed with this novel resist formulation used the ICL in the same ratio by weight as the standard cross-linker used in all previous experiments. This equates to 5.7 epoxide groups for every tBOC group and every 2.5 PAG. Figure 3.30 shows dense lines at 32 nm and 28 nm pitch patterned on resist with ICL.

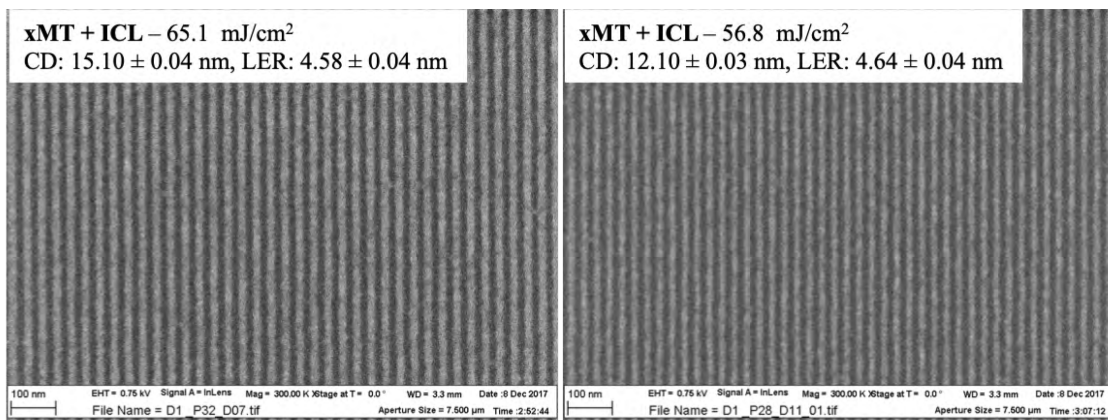

FIGURE 3.30: SEM images of 32 nm pitch (left) and 28 nm pitch (right) dense lines patterned with EUV-IL on resist formulation with the ICL

When the ratio of the ICL in the resist formulation is adjusted to bring the number of epoxides to 15, which is equal to the number of epoxides in the standard resist formulation ([0.2:2:1] by weight with the standard cross-linker), rather than 5.7, the lines shown in figure 3.31 are obtained.

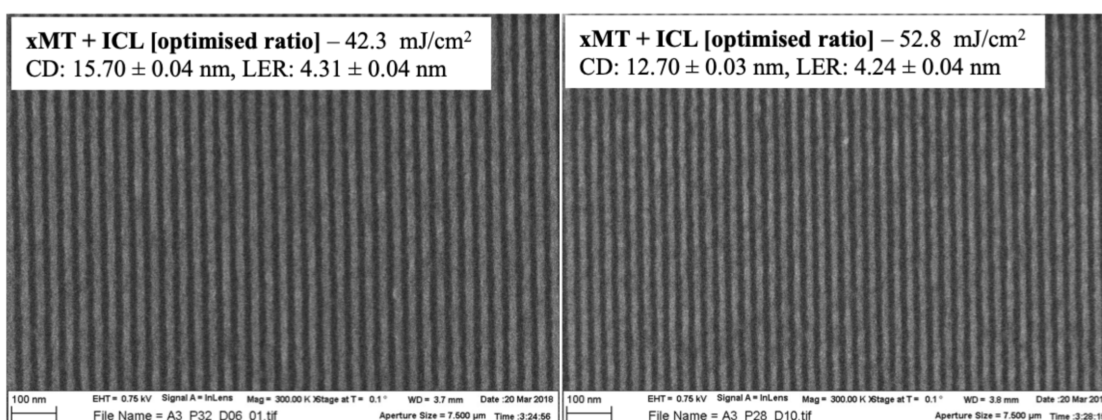

Figure 3.31: SEM images of 32 nm pitch (left) and 28 nm pitch (right) dense lines patterned with EUV-IL on resist with ICL in optimised formulation

It can already be deduced from the above two figures that the second formulation is more sensitive and produces lines with lower LER. For further investigation, a series of CDs and LER were measured on multiple SEM images and the results are shown in figures 3.32 and 3.33. Error bars in these graphs are between ± 0.03 and ± 0.05 and are not very well visible on the CD scale.

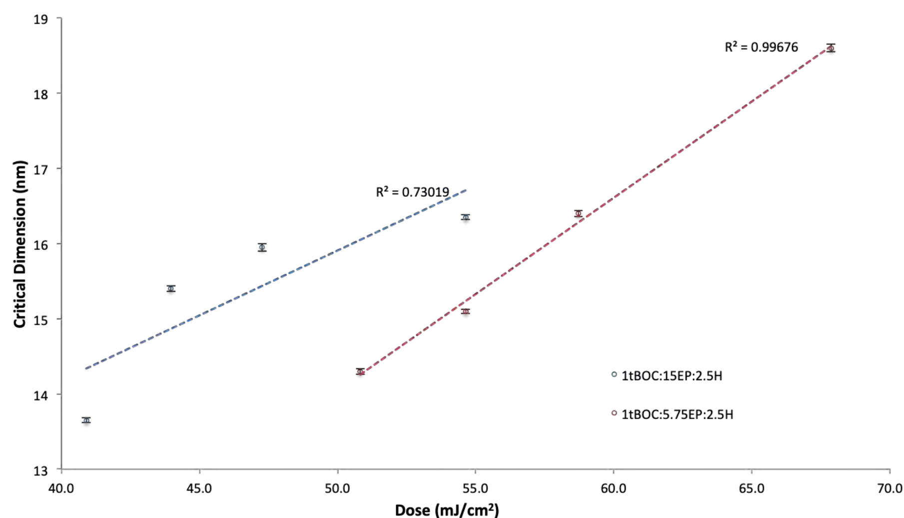

Figure 3.32: CD as a function of dose measured on dense lines patterned with EUV-IL on resist formulations with the iodinated CL. Red - standard formulation by weight; Blue - optimised formulation for number of molecules of each component in the resist system

Figure 3.32 shows that the formulation containing more epoxide groups is more sensitive than the one containing less epoxides. This means that, when the number of epoxides in the material is low more photons are required to generate more

photo-acid generators to increase the probability of one acid to trigger the reaction between one epoxide and one tBOC group or between two epoxides. When the number of epoxides increases the probability of one acid to trigger a reaction is higher, and fewer photo-acids are required to be generated, therefore less EUV photons are needed for the exposure to happen.

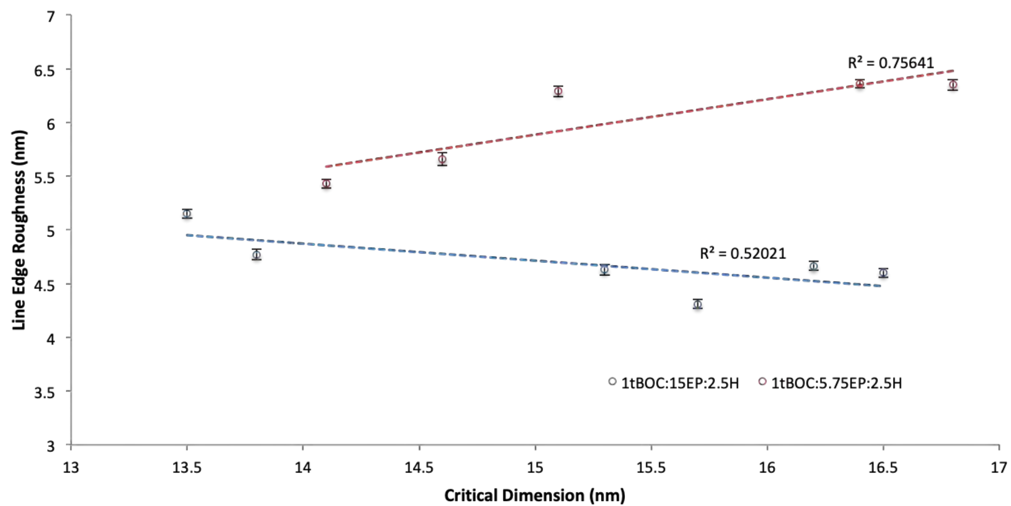

FIGURE 3.33: LER as a function of critical dimension on dense lines patterned with EUV-IL on resist formulations with the iodinated CL. Red - standard formulation by weight; Blue - optimised formulation for number of molecules of each component in the resist system

From figure 3.33 it can be easily seen that the formulation where the number of tBOC groups and PAG molecules is adjusted to make up the standard formulation of 1 tBOC : 15 Ep : 2.5 H, demonstrates lower LER values than the formulation where the ratios are calculated by weight. This is probably due to the reduced number of photo-acids generated in the resist film, and the overall reduced acid diffusion length.

3.8 Overview

Resist		Improvements	Disadvantages	Observations
xMT standard (0.2 resin + 2.5 % Q)				
xMT high + 2.5 % Q		LER very slightly improved	Sensitivity decreased by 17%	
xMT high resin no Q		LER value similar to standard xMT + 2.5% Q	Sensitivity similar to standard xMT + 2.5% Q	Proof of self-quenching behavior in the xMT system, in the absence of additive quencher
EX2 standard		LER improved by 2% compared to xMT	Sensitivity decreased by 23.50%	Stiffer structure of resin designed to reduce LER
EX3 standard		LER improved by 3% compared to xMT	Sensitivity decreased by 50%	-
xMT + 1% SnI_2		No improvement	Sensitivity decreased by 42.92% LER increases by 4.85%	-
EX3 + 1% SnI_2		No improvement	Sensitivity decreased by 38.64% LER increases by 3.68%	-
EX2	+ 1% SnI_2	Sensitivity increases by 28.39%	LER increases by 10.24%	This material exhibits a different response (in terms of sensitivity) to metal additive than xMT and EX3. Increasing the metal concentration increases the LER
	+ 2% SnI_2	Sensitivity increases by 25.46%	LER increases by 27.47%	
MIR xMT		Sensitivity improved by 16.32%	LER increased by 2.41%	Removal of contamination metals reduces scattering of secondary e^- in xMT
MIR EX2		Sensitivity significantly improved by 55.06%	LER increased by 10.53%	LER of EX2 largely impacted
MIR EX3		Sensitivity improved by 55.35% LER improved by 4.58%	-	Roughness is reduced in MIR EX3 as opposed to the other 2 materials
MIR EX2 + C_6H_5I		Sensitivity is improved by 5.85% LER slightly improves by 0.5%	-	At optimum concentration of C_6H_5I added
MIR EX3 + C_6H_5I		LER is improved by 2.35%	Sensitivity slightly decreases by 1.83%	Different concentrations of C_6H_5I render slightly higher sensitivity but LER improvement is smaller
xMT + Iodinated CL		Resolution improved (down to 12 nm dense lines)	LER values are not improved	This material has no added quencher

FIGURE 3.34: Summary of lithographic performance improvements and disadvantages in various resist systems tested in this chapter

3.9 Conclusions

This chapter presented the xMT negative tone molecular resist system with a study of formulation optimisation for both EUV-IL and EBL. It was found that increasing the resin ratio from 0.2 to 0.5 in the xMT formulation with 2.5% quencher decreases the sensitivity of the material by 17% and improves the LER by a small percentage of 0.24%. The most interesting finding in this experiment was the fact that the formulation containing high resin concentration but no quencher added exhibited the same performance as the formulation containing standard resin concentration but 2.5% quencher added. This shows that the xMT material manifests a self-quenching mechanism as the resin concentration increases, which

also explains the higher dose required for the 0.5 formulation compared to the 0.2 formulation. This property is very useful for further tailoring of the xMT resist system.

The evaluation of enhanced variants of the xMT resin molecule was also conducted in this chapter and the results showed that out of the three resins, the xMT remains the most sensitive to EUV with EX2 requiring $\sim 24\%$ more dose and EX3 requiring $\sim 50\%$ more dose. However the LER values are lower in EX2 and EX3 than in xMT by 0.27 ± 0.09 nm in EX2 and 0.5 ± 0.09 nm in EX3. Whereas these changes are of a small magnitude, they show that minor changes in the molecular structure of the resin trigger differences in the lithographic performance of the material.

The study of the effect metal additives have on the lithographic performance of the xMT resist system provided interesting results. Whereas the expectation was that the addition of metals in the resist formulations would improve their sensitivity, this was not case for xMT and EX3. In EUV the addition of 1% SnI_2 decreased the sensitivity of both xMT and EX3 resists by ~ 43 % and ~ 39 %. Moreover, the LER was also increased by 4.85 % and 3.68 % respectively. However, when added to EX2, SnI_2 increased the sensitivity of the material by over 25%, but the LER was impacted in a negative way, at a higher level than both the xMT and EX3, with an increase of over 10%. When the concentration of SnI_2 increased to 2% the change in LER increased to ~ 28 %. It is as yet unclear what it is about the metal addition process that interferes with the exposure mechanism of the resist, therefore it is difficult to explain why the sensitivity of EX2 benefited from SnI_2 addition in EUV exposures, whilst xMT and EX3 did not. One remark that could be made here is that the SnI_2 was added so that the number of Sn atoms represented 1% of the number of molecules in the system. Given the differences in the molecular structures of xMT, EX2 and EX3 the number of Sn might be better matched with the number of functional groups in the system or the entities that

are known to trigger or participate in the reaction mechanism. This could be a subject of further investigation.

The EBL exposures performed on xMT and EX3 and patterning pillars showed that the EX3 material is more sensitive than the xMT by 8.7%. When 2% SnI_2 is added to the two materials EX3 is still more sensitive by 7.4%. A slight sensitivity increment is observed in both materials. For lines patterned with EBL, the EX3 metal hybrid is more sensitive by 9.3% than the xMT metal hybrid. Again, a slight boost in the sensitivity is observed with the addition of metal in xMT and EX3 when patterning in EBL.

The lithographic performance of xMT, EX2 and EX3 offered by an extra-purification procedure - the metal ion removal process - was also evaluated. It was shown that in all three materials the MIR process brings a benefit over the sensitivity with EX3 being the most responsive to the process with an improvement of $\sim$ 54%. The LER is negatively impacted by the MIR process in xMT and EX2 but an improvement of $\sim$ 5% was found in the EX3. The different molecular structures of the three resins might fold differently and during the MIR filtration process different metal ions might be retained or removed, depending on their sizes, their charge, and their mobility. It is uncertain which metals are responsible for the sensitivity change upon their removal from the resist materials, and which ones are responsible for roughness changes, but the results of this experiment showed that the EX3 material has improved in both of these categories after the MIR process.

When iodine in organic compounds such as iodobenzene was added to the EX2 system it was found that the LER was reduced by 0.5% at the cost of sensitivity which increased by $\sim$ 6% . This could mean that iodine atoms have a more controlled range of scattering in the organic high-Z EX2 system compared to the metal hybrid systems, where tin atoms could overcome this effect by manifesting

larger range scattering of secondary electrons that would produce exposures further away from the designed area, thus introducing roughness, however further examination of the exact mechanism is required.

Furthermore, novel formulations with high-Z cross-linker molecules were tested and analysed in this chapter. Whereas neither the sensitivity of this new material nor the roughness are improved compared to the standard xMT it was shown that a resolution as low as $\sim$ 12 nm can be obtained when patterning lines in EUV using this material. Optimising the ratio that is used in the formulation can have benefits on the sensitivity as well as the LER obtained. Thus, a LER reduction of $\sim$ 3% was obtained in features of $\sim$ 15 nm and $\sim$ 5% in features of $\sim$ 12 nm when the formulation was tailored for the optimum number of functional groups of each component to match with all the other components.

Chapter 4

Multi-trigger Resist

Introduction of the EUV tools in industry require a lot of effort and with the large improvements on the tools, the resist manufacturers had to meet the expectations and develop new platforms suitable for this new generation of lithography. The multi-trigger resist (MTR) concept [59, 126, 127], is a new concept introduced to define the new mechanism of interaction of EUV photons with a newly developed resist system. This system has been tailored and build to address the trade-off relationship between sensitivity, resolution and LER. The MTR mechanism enables the system to exhibit high sensitivity and manifests an intrinsic dose dependent quenching behaviour for improved resolution while reducing the material stochastics. In the previous chapter I looked primarily at changes to the xMT materials to optimise performance. In this chapter I will explain the multi-trigger resist (MTR) mechanism and investigate optimisation of the effect.

4.1 Mechanism

The multi-trigger material is composed of a resist matrix, formed by a MTR resin molecule and a cross-linker molecule, and a PAG entity. At the interaction with

the EUV photons secondary electrons will be generated followed by photo-acid generation. So far, the process is similar to the one encountered in a traditional CAR, but the novelty of the MTR system is the response of the resist matrix to the interaction with photo-acids. The response is an implementation of a logic-type function and is shown in figure 4.1: photo-acids will activate matrix molecules but the reaction will only proceed further if an MTR molecule and a cross-linker are simultaneously activated in close proximity to each other. Upon reaction, both photo-acids will be released and free to activate new molecules.

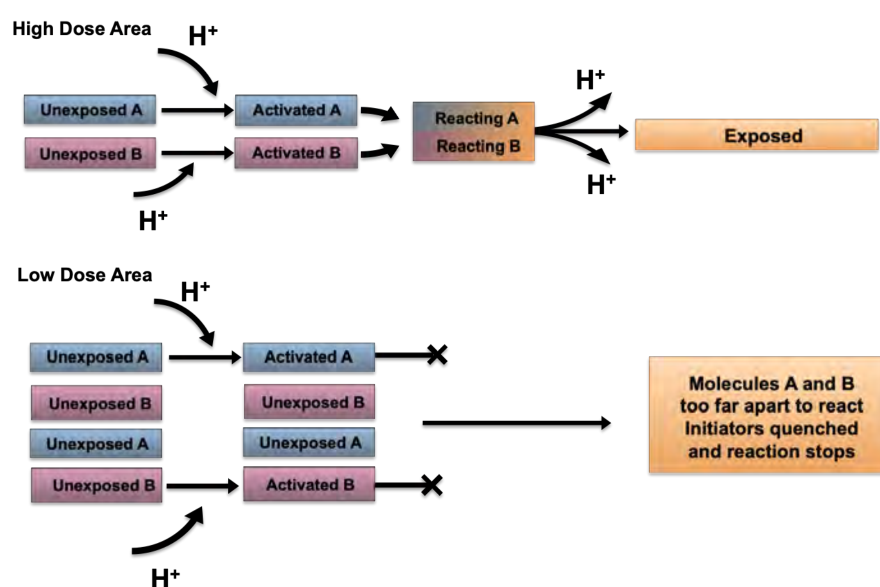

FIGURE 4.1: Schematics of the MTR mechanism

Matrix molecules can be activated at larger distances from each other, as can be seen in the low dose area case in figure 4.1, where there are non-activated molecules neighbouring activated molecules, in which case the exposure reaction will not proceed and the acid will not be released and be free to activate other molecules. The removal of the photo-acid from the system introduces a self-quenching behaviour which is highly dependent on the dose. Therefore the MTR material exhibits high sensitivity at a certain dose window, outside of which the exposure is quickly quenched, leading to sharp lines and low LER values [126, 128]. In effect the resist chemistry is approximately first reaction order in the high dose regions, and

second reaction order in the low dose regions.

4.2 Optimised Component Ratio

In order to investigate to what extent one is able to control the MTR behaviour we have varied the concentration of the MTR component in various formulations and observed the effect. Figure 4.2 shows the standard MTR formulation demonstrating 16 nm half-pitch patterns with LER of 4 nm at a dose of 43 mJ/cm^2. The effect of increasing the proportion of the MTR component is seen in the right image where LER is reduced significantly to 2 nm at the same pitch and similar dose.

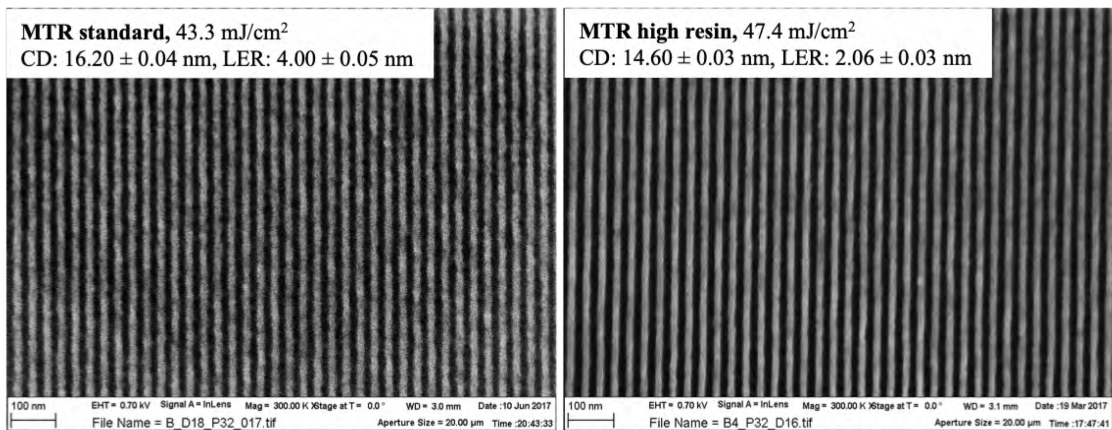

FIGURE 4.2: MTR standard formulation (left) and high resin ratio (right) from [126]

A total of 4 ratios have been tested and figures 4.3 and 4.4 show the trend of the dose when increasing the MTR component concentration. Table 4.1 presents the effect of increasing the MTR component on the LER. MTR1, MTR2 and MTR3 feature slight differences in the resin molecule, therefore their lithographic performance is expected to differ in some ways. MTR3 is faster (more sensitive) than MTR2, as designed, and has a better LER with the most difference at higher MTR ratios. The best LER occurs at 0.45 ratio for MTR2 and at 0.69 for MTR3.

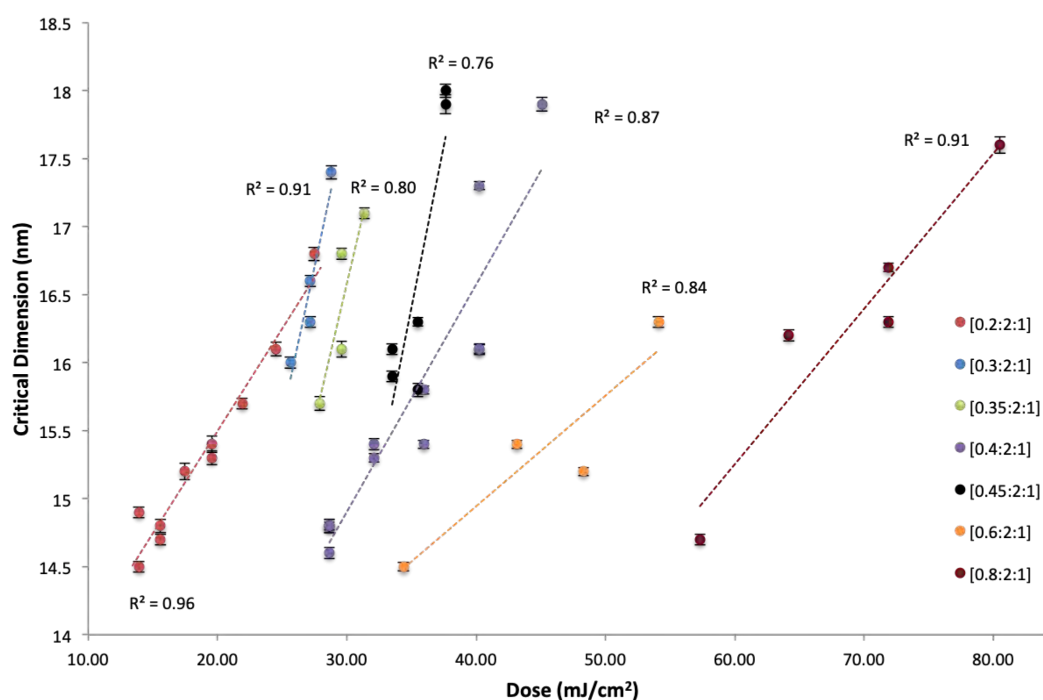

FIGURE 4.3: Critical dimension patterned as a function of dose when increasing the MTR ratio in MTR2

Figure 4.3 demonstrates the increase in the dose required to pattern features widths in the range 14 to 18 nm on 32 nm pitch as the MTR2 ratio increases from 0.2 to 0.8. It can be seen that the dose range required to achieve critical dimensions in the range 14.5 $\pm$ 0.03 nm – 16.5 $\pm$ 0.03 nm for the 0.2 formulation lies between 14 $\pm$ 0.7 mJ/cm^2 and 29 $\pm$ 1.5 mJ/cm^2; this range is shifted to 30 $\pm$ 0.2 mJ/cm^2 – 40 $\pm$ 0.2 mJ/cm^2 for the 0.4 formulation and even towards 80 mJ/cm^2 range for 0.8 formulation.

The reason for which the higher MTR ratio formulations require more dose is because there are more tBOC protected molecules in the system that need to be deprotected for the exposure to take place, therefore in order to pattern a specific critical dimension more photons will be required to generate more acid that activates the resist matrix for the exposure reaction.

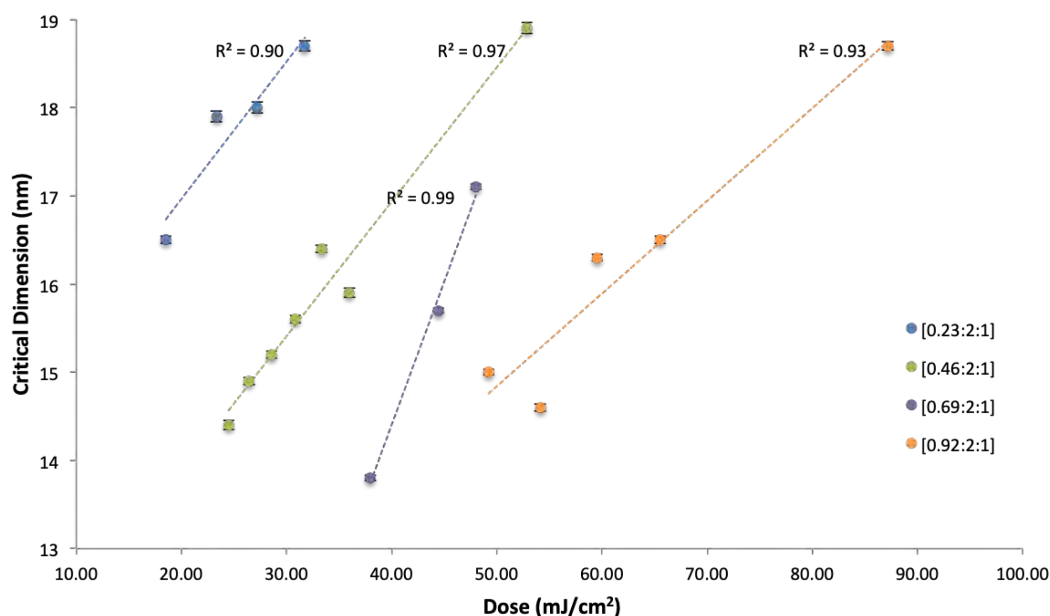

FIGURE 4.4: Critical dimension patterned as a function of dose when increasing the MTR ratio in MTR3

For MTR3 the same trend can be observed as in the case of MTR2, the dose required to pattern features in the range 14 nm to 18 nm increases with the MTR3 concentration in the system. Hence it can be seen in figure 4.4 the shift in the dose range on the x axis from 16 ± 0.1 mJ/cm^2 – 3 0 ± 0.2 mJ/cm^2 for 0.23 formulation towards 30 ± 0.2 mJ/cm^2 – 50 ± 0.3 mJ/cm^2 for 0.46 formulation and the trend continues as the MTR ratio increases. It is observed that MTR3 is more sensitive than the MTR2 at all ratios, which means that the MTR3 molecules are not necessarily required to be completely tBOC deprotected in order to be activated and participate in the exposure mechanism. This is another advantage of the MTR3 system, aside from the improved LER.

MTR2 has a lower molecular mass than MTR, which is the reason why the ratios are not identical for the two systems, but they are calculated to allow for the same number of molecules of each of the resins (MTR2 and MTR3) to be added in the resist formulation.

Resin	Ratio	Dose(mJ/cm^2)	CD (nm)	LER (nm)
MTR2	0.2	24.50 ± 1.22	16.10 ± 0.05	6.66 ± 0.07
	0.3	27.20 ± 1.36	16.30 ± 0.04	5.48 ± 0.06
	0.35	29.60 ± 1.48	16.10 ± 0.06	5.47 ± 0.07
	0.4	40.30 ± 2.02	16.10 ± 0.03	5.08 ± 0.06
	0.45	35.50 ± 1.78	16.30 ± 0.03	4.33 ± 0.05
	0.6	54.10 ± 2.71	16.30 ± 0.04	5.18 ± 0.05
	0.8	71.90 ± 3.60	16.30 ± 0.04	5.89 ± 0.06
MTR3	0.23	18.5 ± 0.93	16.50 ± 0.04	5.42 ± 0.07
	0.46	29.6 ± 1.48	16.40 ± 0.02	4.35 ± 0.05
	0.69	44.4 ± 2.22	15.70 ± 0.03	4.93 ± 0.06
	0.92	51.85 ± 2.59	15.60 ± 0.03	5.26 ± 0.05

TABLE 4.1: Dose and LER for four different MTR ratios in MTR2 and MTR3 evaluated with EUV-IL

In EBL three ratios have been tested. Figure 4.5 shows lines patterned in EBL on MTR2 resist in formulations containing 0.2, 0.4 and 0.8 resin.

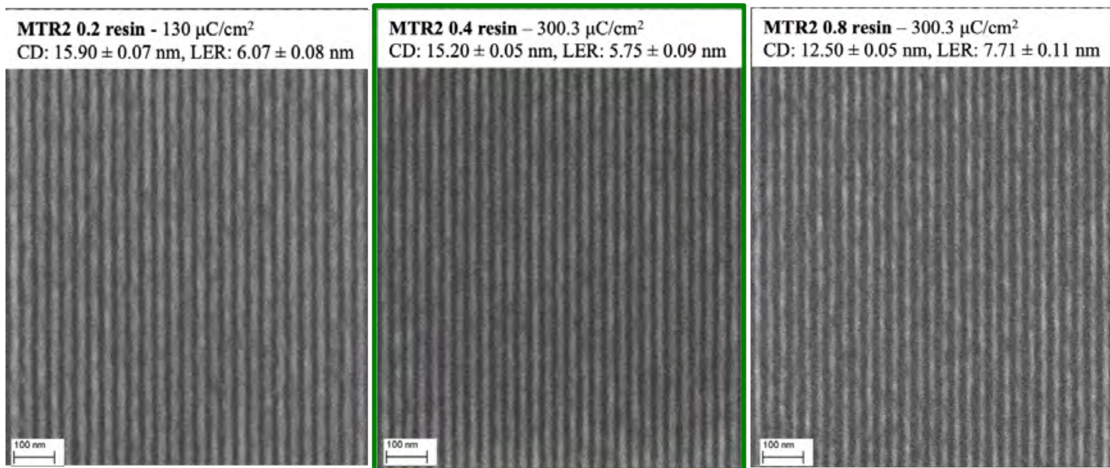

FIGURE 4.5: Dense lines at 36 nm pitch patterned with EBL on MTR2 formulations at standard and higher resin ratios

The immediate observation that can be made after completing this experiment is that the dose required to pattern resist formulations containing higher ratios of MTR component (resin) increases significantly. For MTR2 0.2 to obtain a CD of 15.90 ± 0.07 nm a dose of 8.18 μC/cm^2 per every nanometre of CD patterned was required. This dose increased by a factor of 2.41 in the MTR2 0.4. The LER

slightly improved from 38.18 ± 1.14% at 15.90 ± 0.07 nm to 37.83 ± 1.80% at 15.20 ± 0.05 nm.

Figure 4.6 shows the same lines patterned on MTR3 resist in formulations containing 0.23, 0.46 and 0.92 resin.

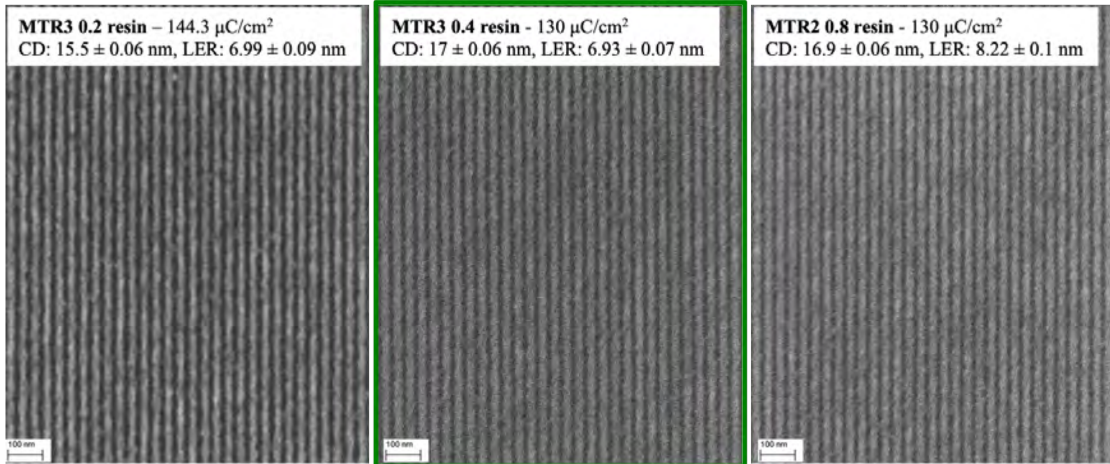

FIGURE 4.6: Dense lines at 36 nm pitch patterned with EBL on MTR3 formulations with standard and higher resin ration

In MTR3 the situation is very similar with the dose in MTR3 0.23 increasing by a factor of 2.23 compared to the dose required in MTR3 0.46 where 7.27 ± 3.64 μC/cm^2 is required for each nanometre patterned in a feature with CD of 15.50 ± 0.06 nm. This increased even further by a factor of 2.46 in MTR3 0.92 relative to MTR3 0.46 and by 5.5 relative to MTR3 0.23. The LER in MTR3 0.46 decreased by 5% compared to MTR3 0.23 but increases in MTR3 0.92, which is not surprising after conducting the experiment in EUV and achieving the same results.

Figure 4.7 shows sparse lines patterned at pitch 28 nm. These lines were designed to be double-spaced so that the proximity effect can be minimised and the effect on the dose change can be attributed to the MTR component variation entirely.

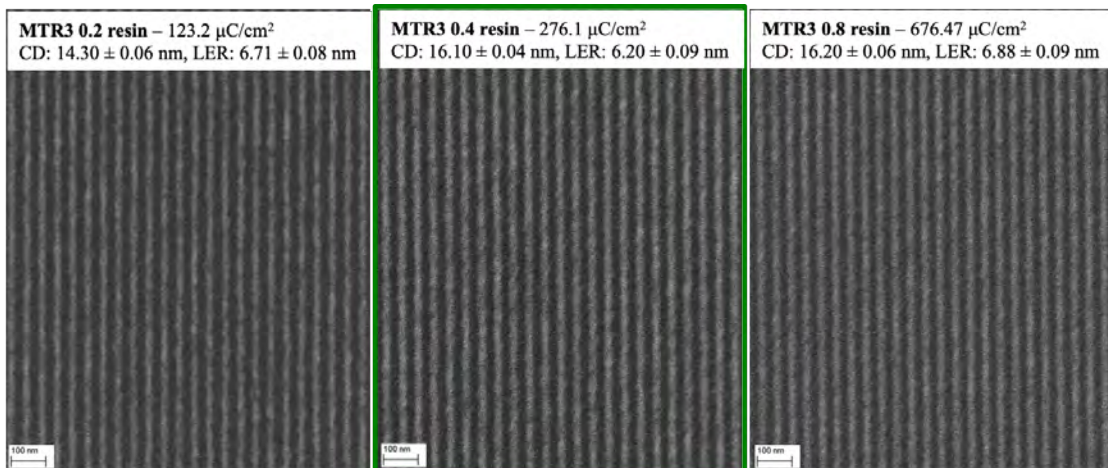

FIGURE 4.7: Sparse lines patterned with EBL at 28 nm pitch on MTR3 formulations with standard and higher resin ratio

When patterning lines on a sparse pitch using MTR3, the dose factor between MTR3 0.23 and MTR3 0.46 is 2 and increases up to 4.85 when patterning MTR3 0.92. As seen previously, when patterning dense lines, the 0.46 formulation demonstrates the best LER which is 8.4 ± % lower than MTR3 0.23 and 3.95 ± % lower than the LER in MTR3 0.92.

Figure 4.8 shows sparse lines patterned on an even larger pitch, 36 nm. With a weaker proximity effect, at this pitch, for MTR3 0.23 the dose required to pattern one nanometre in the 16.40 nm CD is 6.87 μC/cm^2. When the resin ratio is increased to 0.46 the dose/nm increases by a factor of 2.08. In MTR3 0.92 the dose/nm increases by a factor of 5.2 relative to MTR3 0.23. The LER in MTR3 0.46 improves by 11.20 ± % and 15.50 ± % in MTR3 0.92 compared to MTR3 0.23.

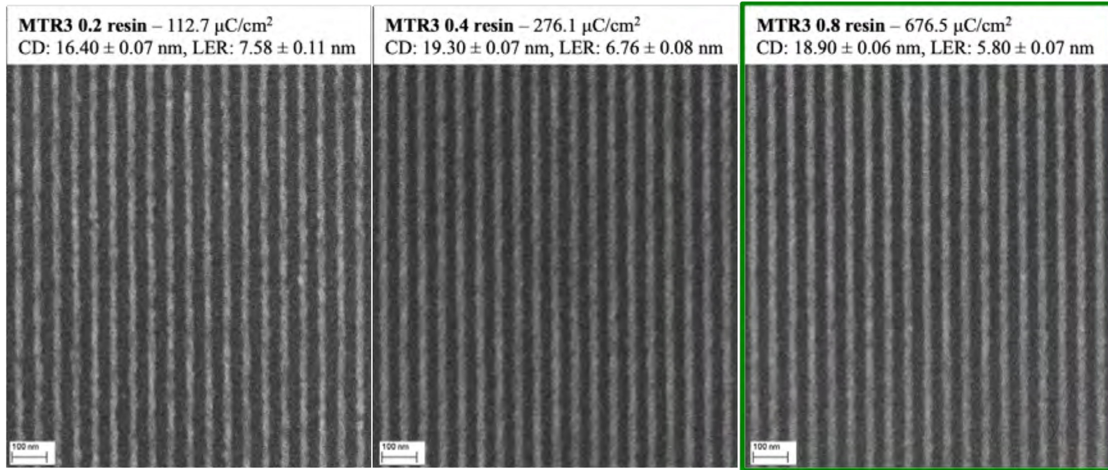

FIGURE 4.8: Sparse lines patterned with EBL at 36 nm pitch on MTR3 formulations at standard and higher resin ratio

Table 4.2 summarises the results obtained after analysing the SEM images presented in figures 4.5, 4.6, 4.7 and 4.8.

Resin	Ratio	CD/nm	Dose/nm ($\mu C/cm^2$)	LER/CD(%)
	0.2	15.90 ± 0.07	8.18 ± 0.20	38.18 ± 0.50
MTR2	0.4	15.20 ± 0.05	19.74 ± 0.46	37.82 ± 0.60
	0.8	12.50 ± 0.05	24.00 ± 0.58	61.68 ± 0.88
		14.30 ± 0.06	6.87 ± 0.17	46.22 ± 0.68
	0.23	16.40 ± 0.07	8.61 ± 0.21	46.92 ± 0.56
		15.50 ± 0.06	7.27 ± 0.17	45.10 ± 0.59
		16.10 ± 0.04	14.31 ± 0.32	35.03 ± 0.42
MTR3	0.46	19.30 ± 0.07	17.15 ± 0.41	38.51 ± 0.56
		17.00 ± 0.06	16.24 ± 0.38	40.77 ± 0.42
		16.90 ± 0.06	41.75 ± 0.98	48.64 ± 0.60
	0.92	16.20 ± 0.06	35.79 ± 0.85	42.47 ± 0.60
		18.90 ± 0.06	40.01 ± 0.93	30.69 ± 0.37

TABLE 4.2: Dose and LER for three different MTR component ratios in MTR2 and MTR3 evaluated with EBL

Both EUV-IL and EBL showed that when increasing the MTR component ratio the sensitivity decreases and the LER improves for an optimum formulation. Above the threshold ratio the addition of MTR component in the formulation leads to degraded LER. The optimum ratio is 0.4 for MTR2 and 0.69 for MTR3 as obtained from EUV-IL experiments. In EBL only three ratios were experimented for each

system. The optimum ratio that gives the best LER in this case was found to be 0.4 for both MTR2 and MTR3.

4.3 Quencher Effect on Resist Stochastics

Reduction of LER is an issue that is constantly being addressed for both CAR and non-CAR, resist materials designed to be used for EUV. Unlike the inorganic materials, which suffer from different issues such as poor sensitivity or instability, in organic resists in order to allow for further technological advancement and for implementation of EUV lithography in industrial use the stochastic issue has to be solved. The very few photons available in EUV lithography introduce stochastics into the exposure mechanism, and the material stochastics on top of this is a matter that has to be investigated and controlled as best as possible. In traditional CARs in order to increase resolution and decrease LER a small percentage of quencher is added to the resist to control the acid diffusion length. This will decrease the sensitivity but most of the time this will still be superior to inorganic resists. However, due to the fact that the introduced quencher is present in such a small amount, and the fact that we can not control the spatial distribution of it, the quenching process will take place at random sites in the resist so that the stochastics of the material affects the roughness of the features patterned. Recently, many groups have focused on understanding and tuning materials stochastics. Naulleau et al. have undertaken simulations to calculate the contribution of multiple factors in the EUV lithographic process to the LER [129]. In figure 4.9 it can be observed that the contribution due to the quencher is comparable to the photon shot noise, and outweighs other material considerations.

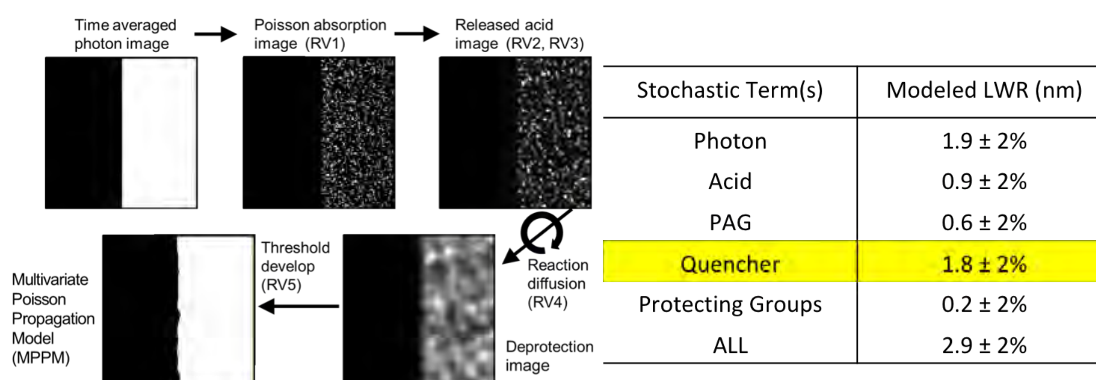

Stochastic Term(s)	Modeled LWR (nm)
Photon	1.9 ± 2%
Acid	0.9 ± 2%
PAG	0.6 ± 2%
Quencher	1.8 ± 2%
Protecting Groups	0.2 ± 2%
ALL	2.9 ± 2%

FIGURE 4.9: Contribution of quencher to total LER value in EUV lithography, from [129]

In order to understand the effect an additional quencher has on the MTR system the MTR level was varied and an external quencher was added in two different concentrations. The samples obtained were exposed to 100 kV electron beam and patterns featuring lines of 14 and 18 nm at relaxed pitches were analysed. The results are summarised in figure 4.10 where the relative dose and LER are plotted as a function of the MTR ratio and the additional quencher concentration.

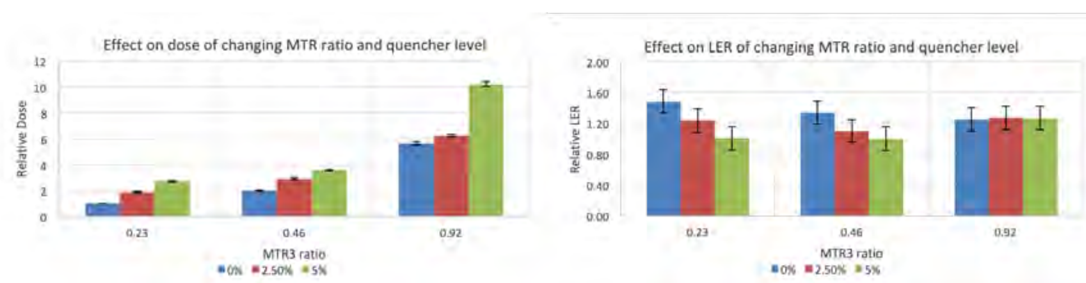

FIGURE 4.10: Effect of quencher level on the dose and LER of features patterned on MTR3 resist formulations with various MTR ratios

It can be seen in figure 4.10 that the additional quencher has a larger effect on the LER at 0.23 and 0.46 MTR ratio but this becomes negligible at 0.92 MTR ratio. The resist matrix is limiting the action of the external quencher, not necessarily through active chemical interaction but by competitive self-quenching of the material. Thus, when the MTR ratio is increasing more photoacid will be used in activating the molecules in the matrix. When the exposure reaction is

not taking place, in areas with low density of activated molecules, the photoacid is locked in the activated chains, therefore the quencher can not chemically react with the molecules in the matrix. This means that regardless of the increasing level of quencher, there will not be a reaction of the quencher happening in the MTR matrix.

The MTR system depends on a carefully balance of the ratio of the crosslinker and the resin in the formulation. The hypothesised mechanism is as follows. When a photoacid is generated it diffuses slowly through the resist film. If it reaches a resin molecule first then on of the crosslinkable functional group of the resin will be protonated, activating it for reactions with an activated crosslinker but causing no other changes. The resin is believed to be stable in the protonated state, and thus the acid is removed from activity in the resist film for the moment. On the other hand, if an acid reaches a crosslinker molecule first, then the crosslinker will undergo catalytic reactions with any surrounding crosslinker molecules. If this growing catalytic chain reaches an unactivated resin molecule then the chain growth will stop, but the chain will remain active ie with the potential to react should the unactivated resin become activated. The practical consequence of this is that the proton that started the crosslinker catalytic chain is also now removed from activity in the resist film for the moment. If the active catalytic chain reaches an activated resin (or a previously unactivated resin is protonated nearby) then a chain transfer reaction will occur, wherein the catalytic chain will crosslink with the resin molecule and both photoacids will be released. There are several consequences to this hypothesised mechanism, the most important of which are that the diffusion of the acid is severely limited as it will form stable protonated compounds with either component, leading to the quenching effect, and suppression of stochastic events in the low dose regions due to the second order nature of the reaction, and that by controlling the ratio of resin to crosslinker, one can control the average volume that catalytic chain growth can propagate before a chain

transfer reaction is required, which allows for tuning of the level of quenching and the sensitivity of the resist.

The best LER value is obtained at 0.46 MTR ratio and 5% additional quencher but this is very similar to 0.23 MTR ratio with the same loading of quencher.

4.4 Conclusions

The MTR system was introduced in this chapter and a study of the exposure mechanism was attempted by varying the MTR component in the formulation and measuring the CD and LER obtained after exposures to EUV-IL and EBL were performed.

It was already shown in the previous chapter that increasing the resin ratio introduces a self-quenching effect, which was proven in this chapter. Increasing the resin ratio in the resist system enriches the resist matrix in the MTR system with molecules that can be activated by photoacids produced in the film. As the number of resin molecules in the matrix increases, more photoacids are required to activate them, which has a negative impact on the sensitivity.

Results in this experiment shown that for MTR2 from 0.2 to 0.8 resin ratio the dose required to pattern 32 nm pitch lines with EUV-IL increased from 24.5 mJ/cm^2 to 71.9 mJ/cm^2. In MTR3 from 0.23 to 0.92 resin ratio the dose changed from 18.5 mJ/cm^2 to 51.9 mJ/cm^2. In terms of LER the lowest value in MTR2 was found to be at resin ratio 0.45 but a constant decrease was observed as the resin ratio increased from 6.66 nm in MTR2 (0.2) to 5.48 nm in MTR2 (0.3) to 5.08 nm in MTR2 (0.4) to 4.33 nm in the MTR2 (0.8) formulation. This is due to the photoacids being retained by the molecules they have activated in the MTR matrix (resin molecules or cross-linker molecules) which were not in the interaction volume of another activated molecule, therefore could not complete the exposure reaction

but consumed the photoacid. In this fashion the unnecessary acid diffusion is reduced as the resin ratio increases, decreasing the LER.

This trend is then followed by an increasing trend as the resin ratio is further increased to 0.6 and 0.8. The same trend is found in MTR3 with the lowest LER value found at MTR3 (0.46).

The effect of additional quencher in the MTR system was also investigated in EUV-IL where the stochastics are more accentuated than in EBL mainly due to photon shot noise. It has been shown that the quencher can improve the roughness of the features patterned on MTR only up to some extent when introduced in high MTR ratio systems, and there is a point where increasing the quencher loading only affects the dose required to pattern but not the LER. It was found that adding quencher in the MTR 0.23 formulation decreases the LER value from 7.15 ± 0.06 nm in the formulation without quencher to 6.14 ± 0.05 nm in the formulation with 2.5% quencher and 4.96 ± 0.04 nm in the formulation with 5% quencher. Similarly, an improvement in the LER was observed when adding quencher in the MTR 0.46 formulation from 6.30 ± 0.06 nm to 4.83 ± 0.04 nm when 2.5% quencher was added, but when 5% quencher was added the improvement wasn't as significant as in the MTR 0.23, LER decreased to 4.71 ± 0.04 nm. For MTR ratio of 0.92 adding quencher in the formulation has no impact on the LER.

This experiment showed that the MTR system features an internal self-quenching behaviour and by adjusting the composition of the resist matrix the lithographic performance of the material is changed in the same manner as by adding external quenchers.

Chapter 5

Achieving Ultimate Resolution

This chapter will present experimental methods that have been evaluated to push the ultimate resolution of the MTR system. The focus will be on the roughness and pattern collapse of the features obtained by exposures to EUV-IL and EBL. A range of variations in the process conditions was investigated with regards to PEB temperature, film thickness of resist to be patterned, underlayer to be used, and post-lithography process variation such as UV assisted rinse and active rinse.

5.1 Post Exposure Bake Variation

In a traditionally chemically amplified resist the PEB is necessary for the exposure to take place. After exposure the photo-acids need thermal energy to diffuse in the resist film and trigger reactions between resist molecules and cross-linker molecules. It is then easy to understand that for a new resist system the PEB time and temperature need to be evaluated and optimum conditions have to be found, which when applied render high performance lithographic patterning.

In the MTR system, however the PEB is not required for the exposure reaction to take place. The exposure chemistry is complete by the time the silicon wafer is

taken out of the exposure tool so then the effect of the PEB on the lithographic features is an interesting study as it is clear that heat is not involved in the exposure process, its contribution should be interesting to investigate.

An initial experiment was performed where two sets of xMT, EX2 and EX3 resist samples were exposed to EUV-IL. The first set received a 90 °C PEB for 1 minute, and the second set didn't receive PEB treatment. The LER was then measured on the 32 nm pitch lines obtained. Figure 5.1 presents the results. The PEB increases the LER value in all cases with the most dramatic change taking place for EX2 where the non-PEB sample demonstrates a value which is 2.03 times lower than the LER on the sample which received PEB. For xMT the difference in the LER between the no PEB sample and the 90 °C PEB sample is 27.64%. In EX3 the difference is 18.42%.

This effect can be easily explained if we start with the hypothesis that the exposure reactions were terminated before even applying the PEB. The heating process would then cause the unnecessary diffusion of acids at random locations in the resist film, triggering undesired cross-linking and increasing the roughness.

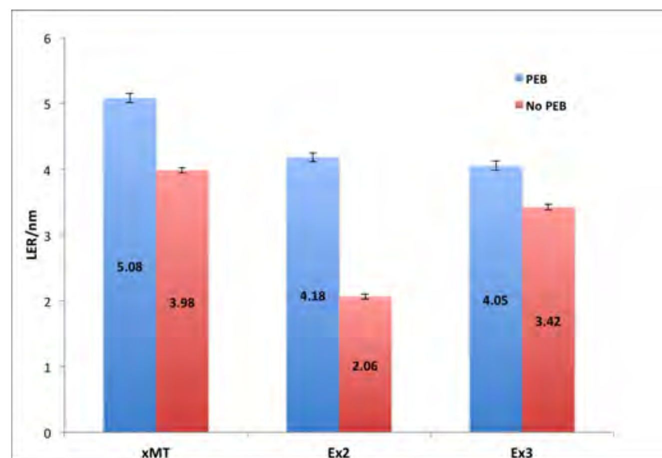

FIGURE 5.1: LER measured on xMT, EX2 and EX3 resist samples that have been treated with post-exposure bake at 90 °C for 1 min and samples that have not received post-exposure bake

Out of the 3 resist materials evaluated EX3 resin is least affected by the PEB, therefore an extended study was performed on this resist. A new experiment was performed where a range of temperatures were employed. For this experiment MIR MTR3 resist samples were exposed in the usual fashion and then a PEB was applied at a range of temperatures varying from 20 °C (not baked) to 90 °C for 1 minute. Figure 5.2 presents the CD and LER as a function of the PEB temperature. Errors on the measured critical dimension are within 0.02 and 0.06 nm. They are visible on the graph.

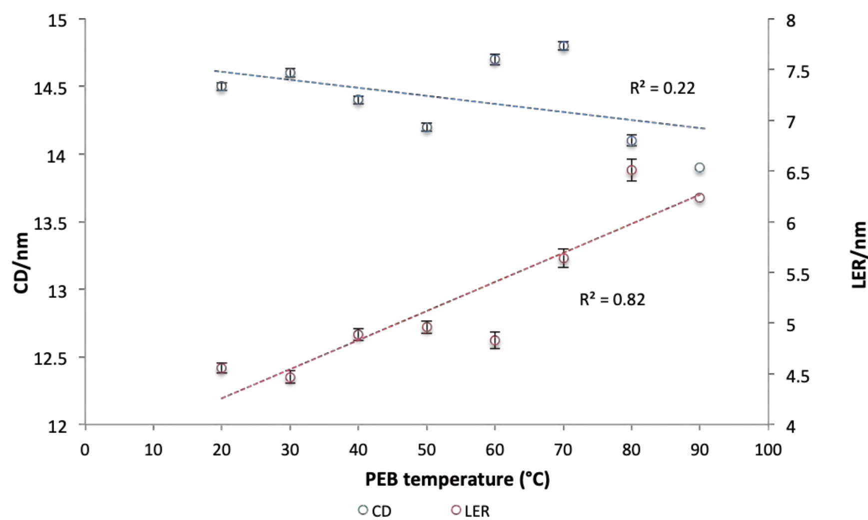

FIGURE 5.2: CD and LER measured on MIR MTR3 resist samples that have been treated with post-exposure bake at temperatures between 20 °C to 90 °C for 1 min

From this experiment it can be seen that a minimum LER can be obtained with a PEB of 30 °C and above this temperature the LER increases reaching a maximum value at 80 °C but it is not clear what happens above 90 °C. Figure 5.3 shows an example of 32 nm pitch lines obtained by exposing the MIR MTR3 resist to EUV light and baked at 60 °C and 90 °C. The left image is the sample without PEB.

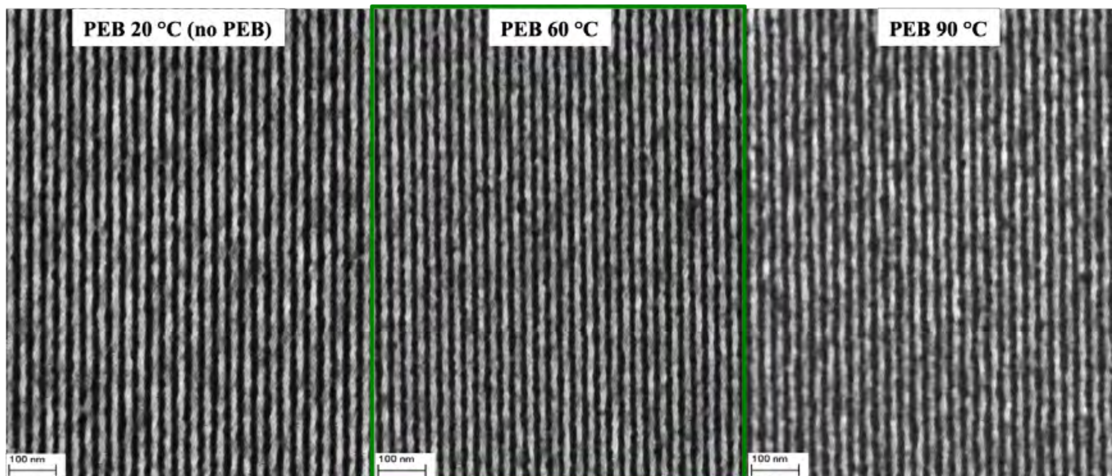

FIGURE 5.3: SEM images of lines patterned at 32 nm pitch on MIR MTR3 resist samples that have been treated with post-exposure bake. left: 20 °C, center: 60 °C, right: 90 °C for 1 min

Also the sensitivity of the resist is slightly reduced with the increasing of the PEB temperature. This is most likely due to the fact that during baking molecules of solvent that might have been trapped inside the film (which produce swelling of features as seen in CAR systems) are now evaporated and there is some rearrangement and reorientation of the resist molecules in the exposed areas. As sensitivity has been expressed as a "dose to size" line, thinning in post processing is equivalent to a sensitivity drop.

Further experiments should be conducted on this basis and more work could be done in the synthesis of a material which can withstand baking temperatures that exceed 90 °C in order to further evaluate the trend of LER.

5.2 Resist Film Thickness Variation

The primary failure mode for resists at high resolutions is through aspect ratio driven pattern collapse. Thick films are required for post-lithography processing of the resist, such as etching. High aspect ratio features are etched into the silicon

substrate, therefore the resist film has to withstand long etching times in order to render these kind of aspect ratios.

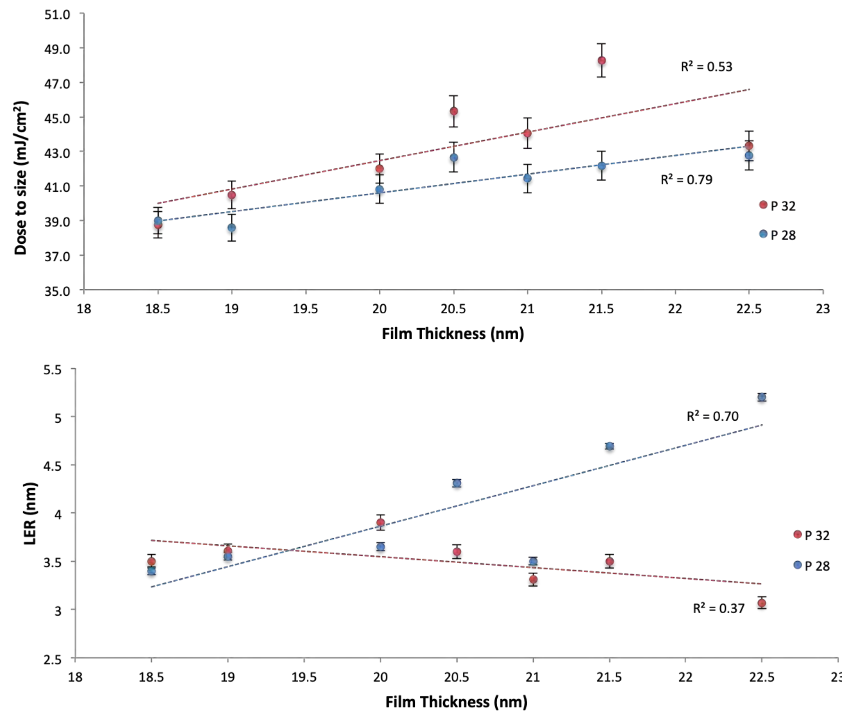

FIGURE 5.4: Dose required to pattern pitches 32 and 28 nm at different thicknesses of the resist. LER measured at various thicknesses for 32 and 28 nm pitch size

However, in general, for most of the resist materials the thickness of the resist film can not be increased as much as would be preferred due to pattern collapse issues. On the other hand, for a resist with very high etch selectivity thinner films should be safe to use for lithography as long as they can experience long etching times without losing any thickness. However, especially in the case of organic resists, thin films generally show a low mechanical strength, introducing line 'wiggling' and poor contrast in SEM imaging.

In the next experiment the MTR2 resist film was spin coated at thicknesses ranging from 18 ± 1 nm to 22 ± 1 nm and the results were analysed in order to find the optimum thickness that mitigates the most commonly encountered failure mode in patterning, namely "wiggling" of lines, see figure 5.4. It was observed that even

half a nanometer difference in the film thickness has an impact on the sensitivity of the material but also on the LER of the features patterned. The conclusion of this experiment was that the optimum thickness required to pattern dense lines at different pitches varies as follows: 22 ± 1 nm for 16 nm lines and 18 ± 1 nm for 14 nm lines.

5.3 Pattern Collapse Mitigation. Active Underlayers

The idea of silanes implementation as adhesion promoters has been around for a long time with studies focused on semiconductor manufacturing [130] in 1991, as well as other disciplines such as biochemistry [131] in 1994 and photochemical deposition of thin polymer films on a silane monolayer formed on solid surfaces [132] in 1999.

The Si surface was hydroxylated by piranha treatment and then treated with triethoxy vinyl silane (TEVS) solution in order to form a silane layer on the surface and facilitate the adhesion of the organic resist film that is to be deposited on the Si silanized surface.

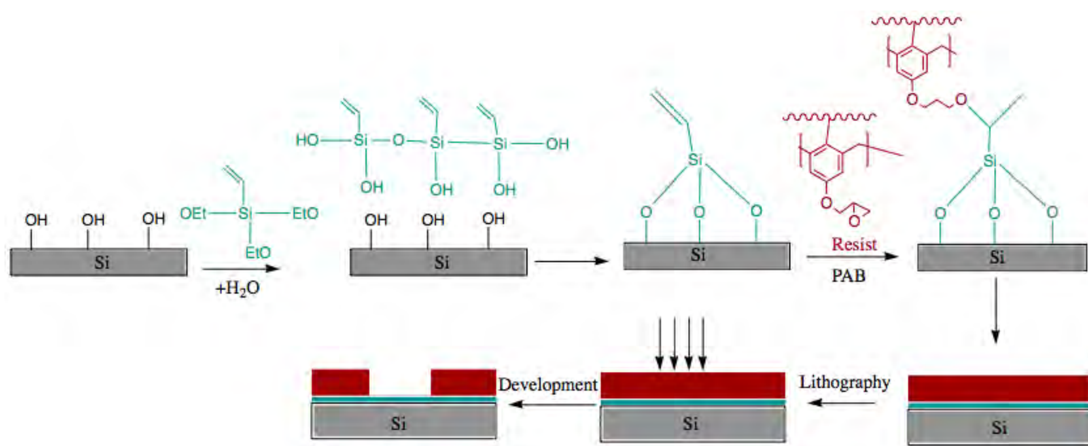

FIGURE 5.5: Scheme of the silanization and lithography process

The triethoxy vinyl silane monomer hydrolyses in the presence of residual water which remains on the substrate after the rinsing process, the ethyl groups are lost and hydroxyl groups are produced instead, which will react with the hydroxyl groups on the Si surface. The hydroxylated monomers then cross-link each other and polymerize into silicon gels forming Si-O-Si covalent bonds, with the vinyl moieties remaining stable on the Si surface. Once the silicon substrate was silanized the resist was deposited on top of it. During the post application bake procedure, the vinyl groups thermally cross-link to epoxy groups in the resist. In figure 5.5 the process is shown.

5.3.1 Contact Angle Measurements

The contact angle on the silanized Si substrates was measured in order to observe the changes in wetting behaviour. For this purpose, the contact angle was measured at the end of each step in the silanization process. Figure 5.6 shows an example of droplet shape on the untreated Silicon wafer, hydroxylated wafer and silanized wafer.

FIGURE 5.6: Water droplet on bare (left), hydroxylated (center) and silanized (right) silicon. The change in shape of the droplet demonstrates surface modification. The hydroxylated silicon is very hydrophobic, therefore the contact angle was very small (∼ 5 °) and not easily detected by the software at the moment when the image was taken

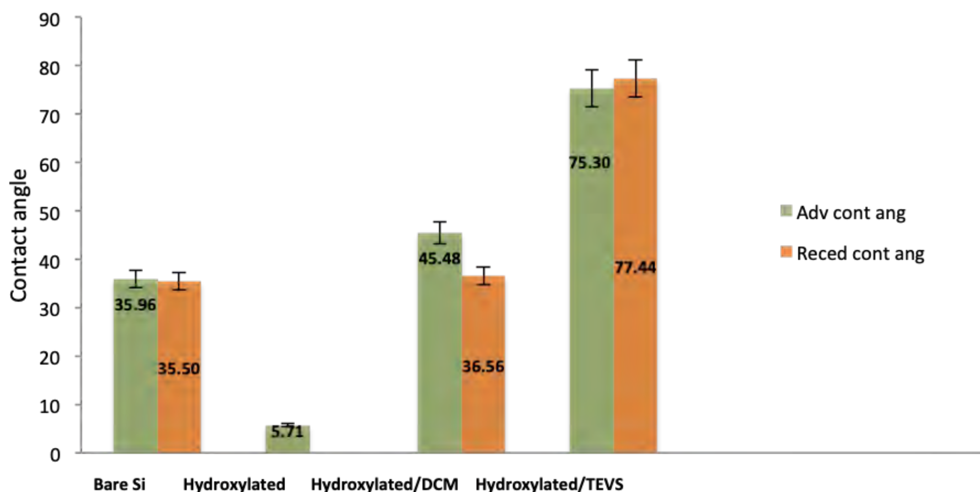

FIGURE 5.7: Dynamic contact angle measurements on differently treated Si substrates. The change in the wetting behaviour of the substrate demonstrates surface modification

As it can be seen in the figure 5.7, the contact angle of the substrate decreased to a value below 10 ° after piranha treatment as a consequence of the hydroxyl groups formed on the surface. After hydroxylation, the substrate was immersed in the 0.1% silane solution in DCM. The surface became hydrophobic after one hour of immersion as shown by the contact angle value of 75 ° ± 2 ° , indicating that the surface chemistry of the sample is dominated by the silane increasing its compatibility with an organic material. A control sample was also prepared, which was immersed in DCM for 1 hour. The control sample was also measured in order to establish if the solvent used would affect in any way the surface modification. The results show that after immersing the Si substrate in DCM, the contact angle does not increase significantly above the value measured for the bare Si sample.

Once it is established that the silane molecules attach to the Si substrate changing its wetting behaviour, the next question is the homogeneity (in terms of the contact angle hysteresis) of the silane layer formed. Therefore different times of

immersion, between 1 and 4 hours, were tested in order to see how the immersion time influenced the homogeneity of the silane layer formed on the Si substrate.

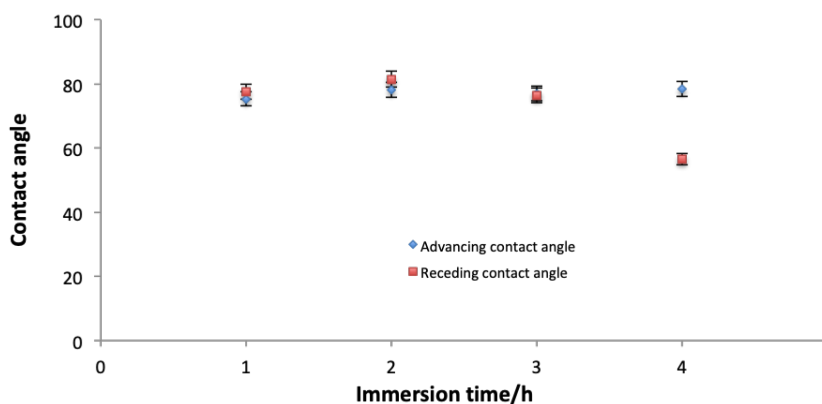

FIGURE 5.8: Dynamic contact angle variation with the immersion time

Figure 5.8 shows that there was not much variation in the contact angle of the four samples tested at different immersion times. However, there is homogeneity alteration, indicated by the increased hysteresis, for the sample immersed in the silane solution for four hours. This would probably be due to cross-linking occurring between silane monomers from the solution and the silane polymer already attached to the surface, after one complete layer was formed. The large hysteresis suggests that the additional silane layer does not fully cover the entire substrate. Figure 5.9 shows the contact angle hysteresis for the four samples immersed for 1, 2, 3 and 4 hours respectively in the silane solution. It can be observed that the sample immersed in the silane solution for 3 hours shows the smallest hysteresis, which suggests that the silane layer formed on this substrate has the best quality within the four samples tested.

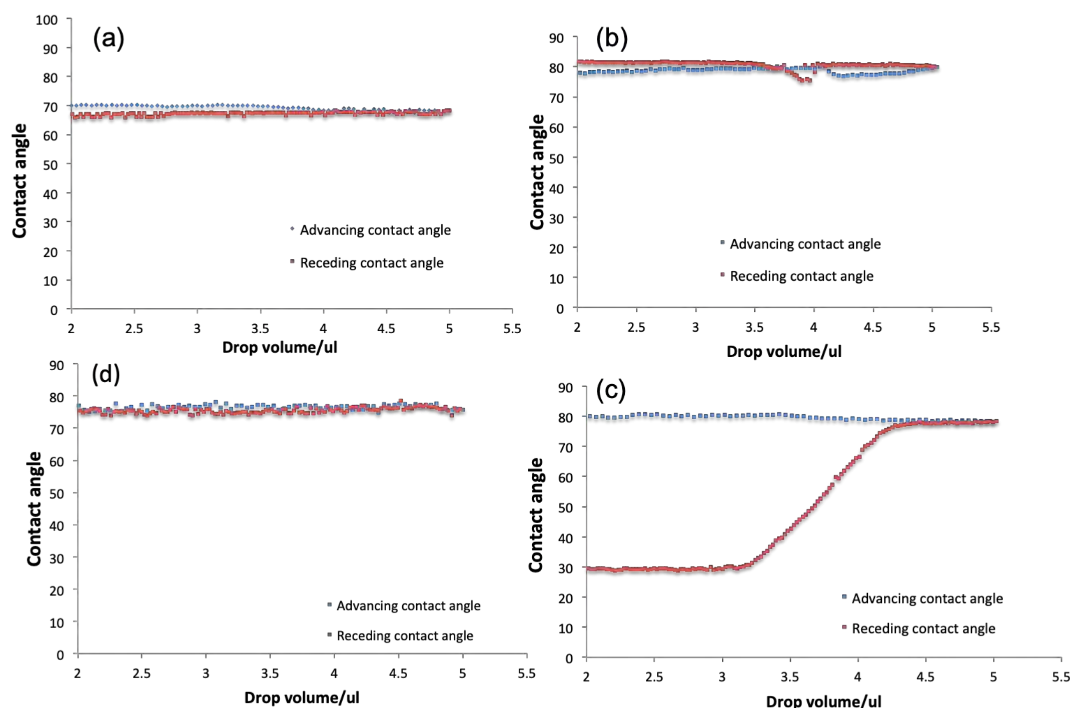

FIGURE 5.9: Hysteresis of the dynamic contact angle of the silanized Si substrate for (a) 1 h, (b) 2 h, (c) 3 h and (d) 4 h immersion in the TEVS solution. The highly inhomogeneous layer can be seen after 4 h

However between 3 and 4 hours of immersion the inhomogeneity of the silane layer increases significantly and a large hysteresis is measured on the last sample. The advancing contact angle varies slightly around 80 °± 2 °, whereas the receding contact angle decreases significantly towards 30 ° as the water droplet shrinks in size encountering uneven domains on the surface rendered by the growing layers of silane. This is probably due to incomplete layers being formed at various sites on a fully formed layer of silane. Once one such "island" is formed on the surface further inconsistencies on the overall surface will rapidly propagate through cross-linking of the silane monomers (which are now "miss-arranged"), compromising the homogeneity of the entire surface.

Apart from the immersion method, two other methods of deposition have been investigated: spin coating and vapour priming. The contact angle measured on

these samples is shown in figure 5.10. These results indicate that the immersion, as well as the vapour priming, methods generate a more hydrophobic surface, as opposed to the spin coating method. This could be due to the fact that in the spinning process there is not enough water involved in the hydrolysis of the silane monomers. Thus, less hydroxyl groups are produced in the silane, less monomers will bind to the Si substrate, resulting in a slightly more hydrophilic surface.

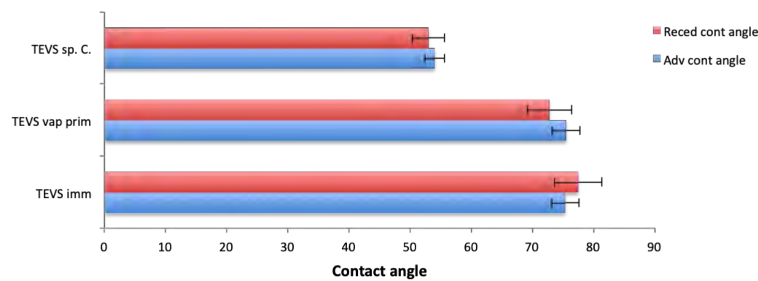

FIGURE 5.10: Dynamic contact angle for the silanized substrates, where the silane was deposited through immersion (imm), spin coating (sp c) and vapour priming (vap prim). Immersion and vapour priming methods result in the most hydrophobic surfaces

A few different silane molecules were deposited on silicon substrates and their contact angle was measured in order to find the suitable silane to be used as an underlayer for lithographic experiments. TEVS and APTES were the two underlayers chosen for lithography experiments. The APTES monomer hydrolyses first when water is presented, its ethyl part is lost and then hydroxyl is produced. They cross-link each other and polymerize into silicon gels. The exposed hydroxyl reacts with the hydroxylated silicon surface, forming Si-O-Si but the amino moieties remain stable on the substrate and will be available for covalently binding with the resist [133].

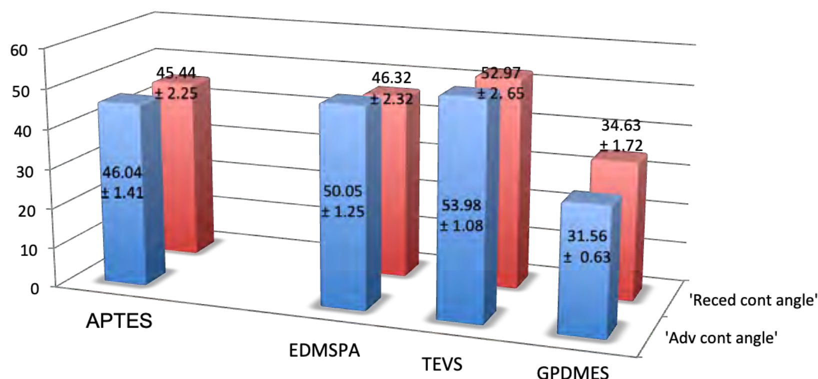

FIGURE 5.11: Comparison of the dynamic contact angle measured on silanes deposited on silicon substrate; Amino propyl triethoxy silane, triethoxy vinyl silane, 3-(ethoxydimethylsilyl) propyl-amine and 3-glycidyloxypropyl (dimethoxy) methylsilane

5.3.2 Lithography on Silanized Substrates

Lithographic experiments were conducted in order to optimise the silane deposition method. The film thickness was deliberately increased to drive pattern collapse on the bare Si samples. The silane molecule to be deposited was TEVS and the same resist formulation is used for all four samples, so that the lithographic performance can only be altered by the underlayer. In figure 5.12 the EUV exposure results are shown where the uderlayer used is TEVS deposited by immersion, spin coating and vapour priming.

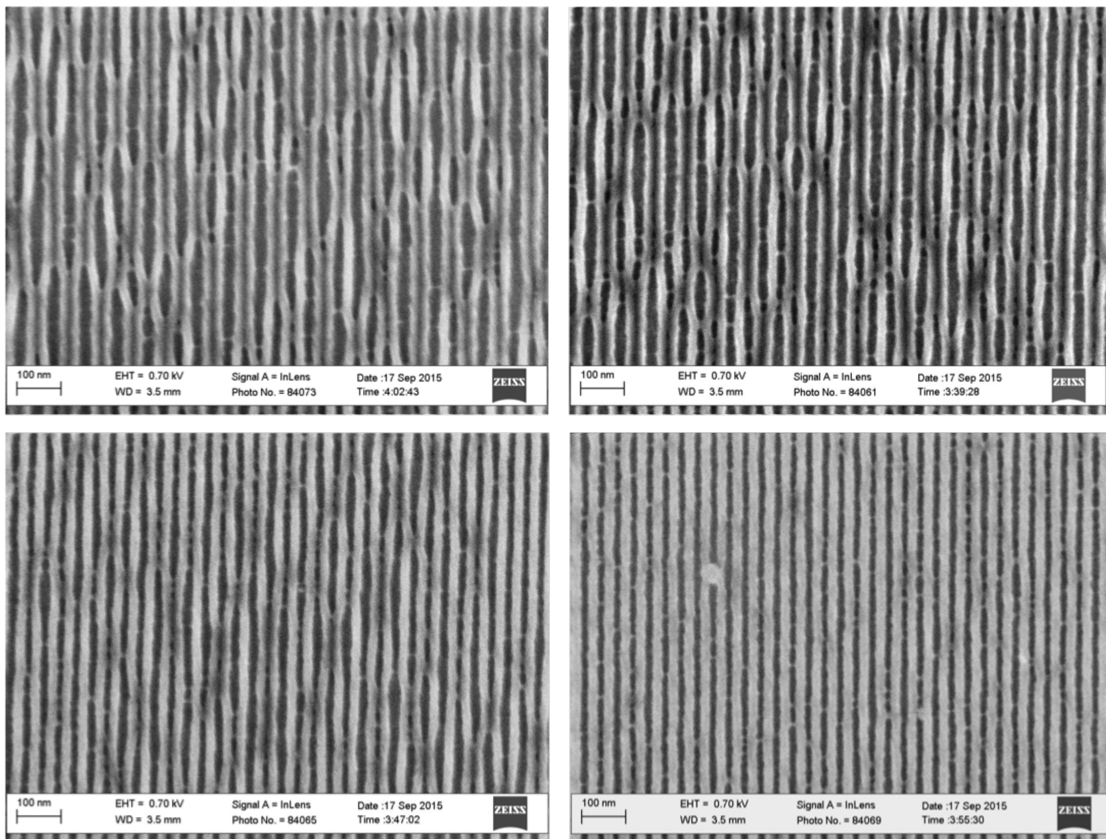

FIGURE 5.12: SEM images of 36 nm pitch dense lines patterned with EUV-IL on control sample - bare Si substrate, silane UL (immersion), silane UL (spin coating), silane UL (vapour priming)

All samples were covered with the same resist thickness, hence the vapour primed sample shows no pattern collapse and higher sensitivity as opposed to the other three samples. Nevertheless, there are small defects on the pattern which could be due to the inhomogeneity of the underlayer but could also be air-borne contamination on the sample.

Apart from the contact angle, which was measured and is illustrated in figure 5.11, other important factors were also monitored such as the capability to form a continuous and homogeneous monolayer and the compatibility of the silane monolayer with the resist. Dichloromethane as a non-polar solvent is not miscible with the standard casting solvent for the resist - ethyl lactate, therefore other casting solvents had to be used to form a resist film on top of the silanized substrates.

PGMEA and cyclohexanone were the two solvents found to be compatible with the resist and with the silane underlayer. Figure 5.13 shows the EUV exposure images obtained using PGMEA and cyclohexanone. In this experiment TEVS and APTES were tested.

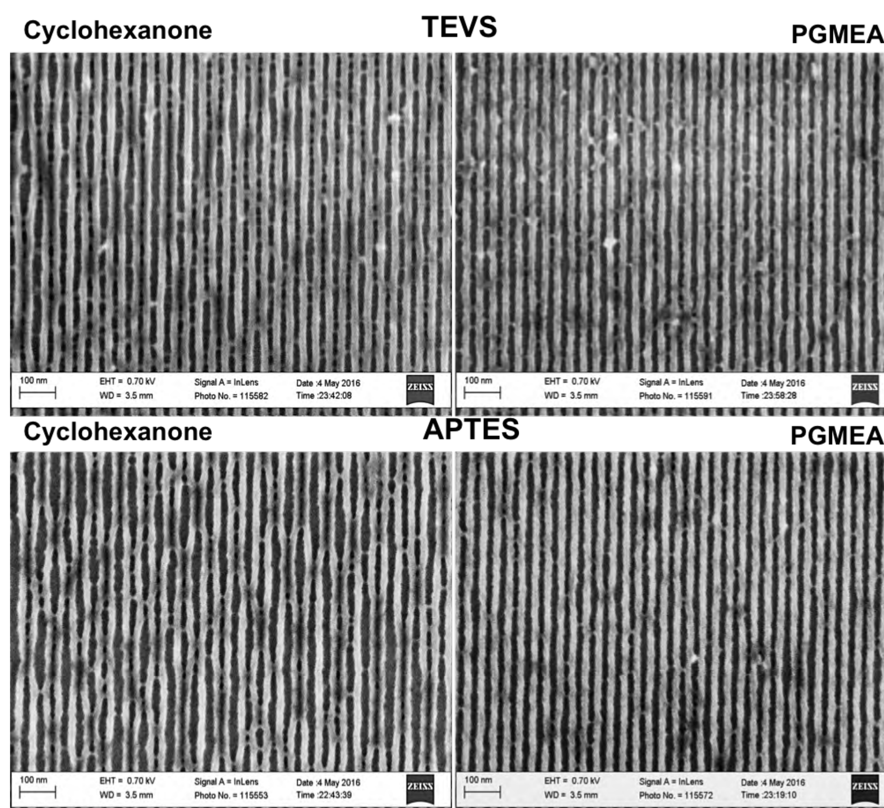

FIGURE 5.13: SEM images of 36 nm pitch dense lines patterned with EUV-IL on resist coated from cyclohexanone and PGMEA on top of TEVS and APTES UL

Although the initial spinning test showed a good compatibility of both resist formulations in cyclohexanone and PGMEA with the silanized silicon wafer, features patterned on the resist dissolved in cyclohexanone are more likely to collapse. Both TEVS and APTES underlayers show no pattern collapse when the resist film is spin coated from PGMEA rather than cyclohexanone. This is not due to the difference in the film thickness generated by the two solutions in the two different solvents. In fact, PGMEA spins a 30 $\pm$ 1 nm film thickness while the cyclohexanone solution spins 21 $\pm$ 1 nm films at the same spin speed and formulation concentration

which was used in this experiment and still the taller features of resist coated from PGMEA are less likely to collapse than the ones from cyclohexanone.

5.3.3 Mechanical Stress on Lithographic Features

The second part of the pattern collapse test consisted of patterning features at various aspect ratios and various spacings on four different silane underlayers and finding the critical stress that can be put on the features patterned on each of the silanes investigated. In order to achieve this two resist film thicknesses were used 34 ± 1 nm and 28 ± 1 nm and the pattern design contained varying line and space widths as shown in figure 5.14. The large lines are kept at 200 nm distance but the inner lines are placed at various pitches and their width is varied to render different capillary forces from one pitch to another.

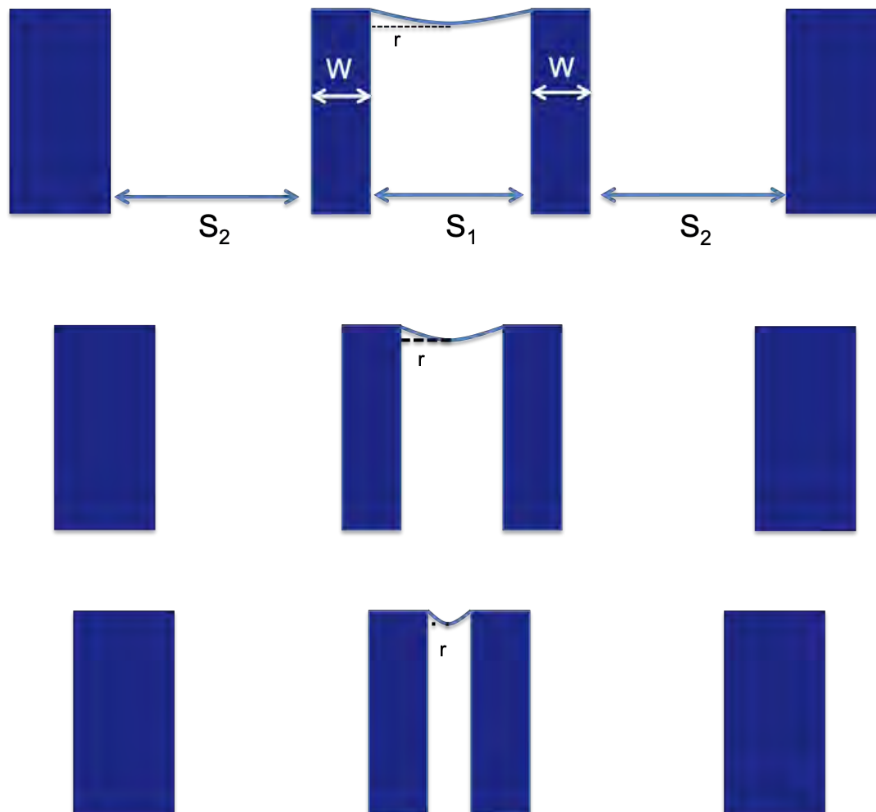

FIGURE 5.14: Pattern designed for EBL exposures with lines at different pitch sizes separated by various spacings in order to introduce different capillary forces during rinsing

In figure 5.14 it can be seen that decreasing the spacing S_1 between the lines, decreases the radius of the meniscus formed by the rinsing liquid. The pressure difference between the air on top of the resist lines and the liquid between the resist lines decreases as r increases according to $P = P_{air} - P_{liquid} = \frac{\gamma}{r}$.

Figure 5.15 shows an SEM image of 40 nm lines at two different spacings - 80 nm and 60 nm.

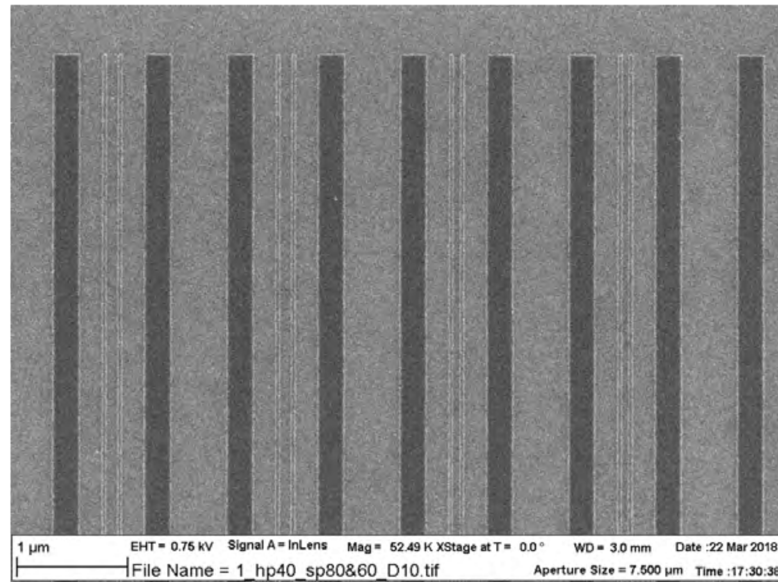

FIGURE 5.15: SEM images of 40 nm pitch lines patterned with EUV-IL on resist on top of silane UL

This pattern is adapted after [108, 134], where they found that features with aspect ratio of 1:2 patterned on a negative tone resist were withstanding a mechanical stress of up to 25 MPa before collapsing. The pattern used here is specifically designed to quantify the effect various underlayers have on the feature collapse when patterning the MTR1 resist at different film thicknesses. As mentioned in the literature review, the main causes of the pattern collapse are the capillary forces and adhesion failure. During the development process the mechanical stress induced by the capillary forces in the rinsing liquid forces the features to bend towards one another. As the stress increases in intensity the resist feature can start to peel off the substrate and collapse onto the neighbouring feature. Using this pattern

design allows one to probe pattern collapse by modulating the magnitude of the capillary forces (varying the spaces and line widths) and evaluate the adhesion of the resist features to the substrate by varying underlayers.

Figure 5.16 shows the features patterned using the MTR1 resist on APTES underlayer. The film thickness of the resist is 28 ± 1 nm and line widths from 36.90 nm to 16.90 nm have been measured on these images. The 28 ± 1 nm film thickness was chosen as a standard from the industry requirements for other commercial resist materials. This is higher than the standard film thickness the MTR resist was normally spin coated as, and pattern collapse is expected to occur in these experiments. As it was shown in the previous section the 22 ± 1 nm film thickness was ideal to pattern 16 nm dense lines, however the features in this pattern are especially designed to investigate the pattern collapse behaviour, and are not dense features, therefore the optimum value of the film thickness is not useful in this experiment.

A variation in the film thickness was also introduced (34 ± 1 nm) in the experiment in order to observe the effect the aspect ratio has on the mechanical stress at the point of collapse.

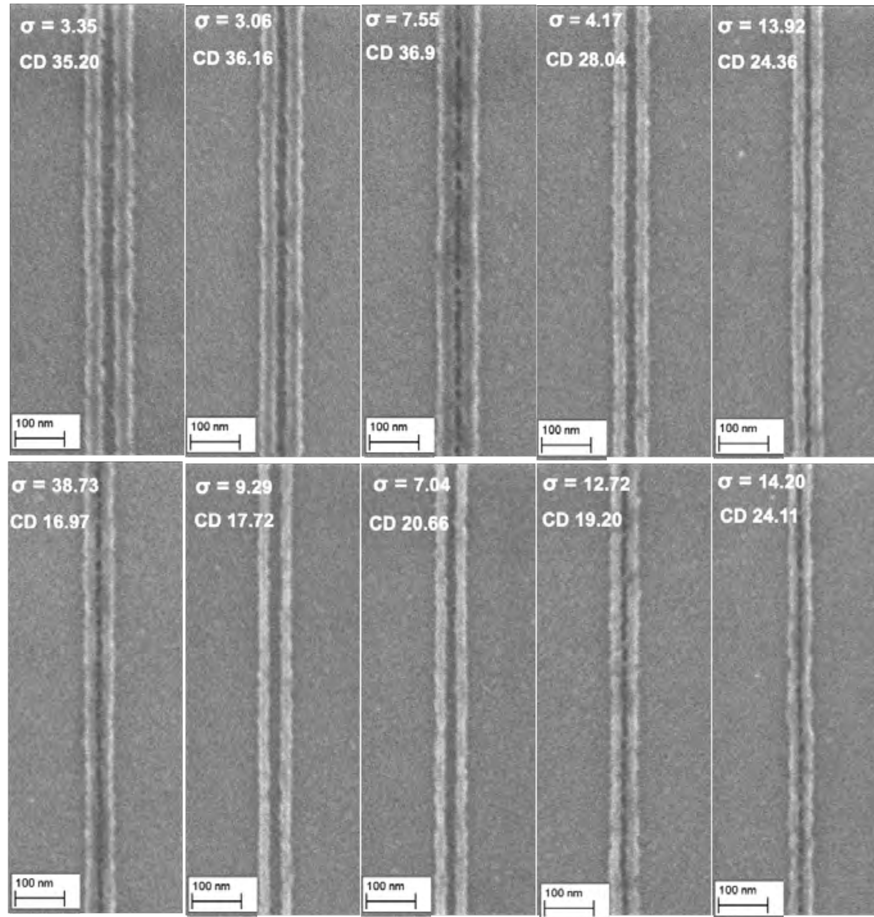

FIGURE 5.16: SEM images of various CDs at various pitch sizes patterned with EBL on 28 nm film thickness of resist on top of APTES UL

The mechanical stress applied by the MIBC rinsing liquid on each of these features was calculated using equation 5.1.

$$\sigma = 6\gamma cos\theta(\frac{H}{W})^2(\frac{1}{S_1} - \frac{1}{S_2}) \qquad (5.1)$$

where: σ is the mechanical stress applied on the feature,

γ is the surface tension of the rinsing liquid (MIBC),

θ is the contact angle of the rinsing liquid on the resist,

H is the height of the features, which is approximately equal to the film thickness if we consider that no significant top loss happens during development and rinse,

W is the width of the feature,

S_1 and S_2 are the inner and outer spacing between the features patterned.

W, S_1 and S_2 were measured on the SEM images acquired using the SuMMIT software.

By keeping the rinse liquid and all other experimental conditions fixed and only changing the interface between the resist and the silicon substrate, the change in the calculated mechanical stress can only be attributed to adhesion forces introduced by the interface.

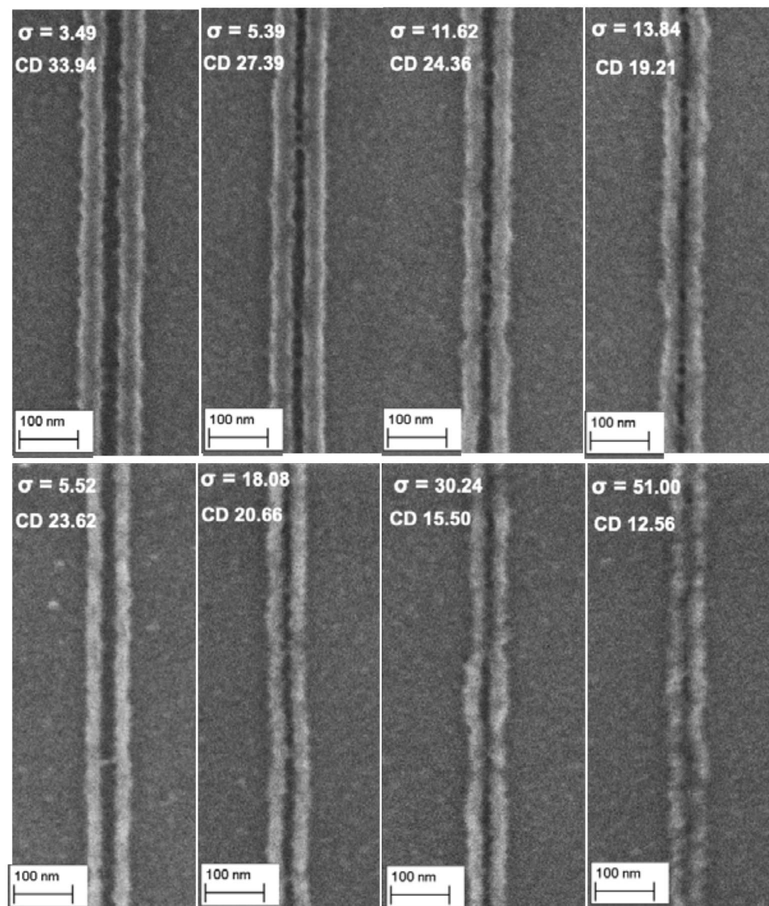

FIGURE 5.17: SEM images of various CDs at various pitch sizes patterned with EBL on 28 nm film thickness of resist on top of TEVS UL

Figure 5.17 shows the same features patterned using the same resist with the same film thickness on TEVS underlayer. It can already be seen from the image without

in depth analysis that smaller line widths could be achieved in this experiment before the pattern collapse occurred with features withstanding values of mechanical stress around 20 MPa. The features patterned on the EDMSPA underalyer are shown in figure 5.18. When this underlayer is used the features start collapsing when the mechanical stress increases above a value of 7.63 MPa.

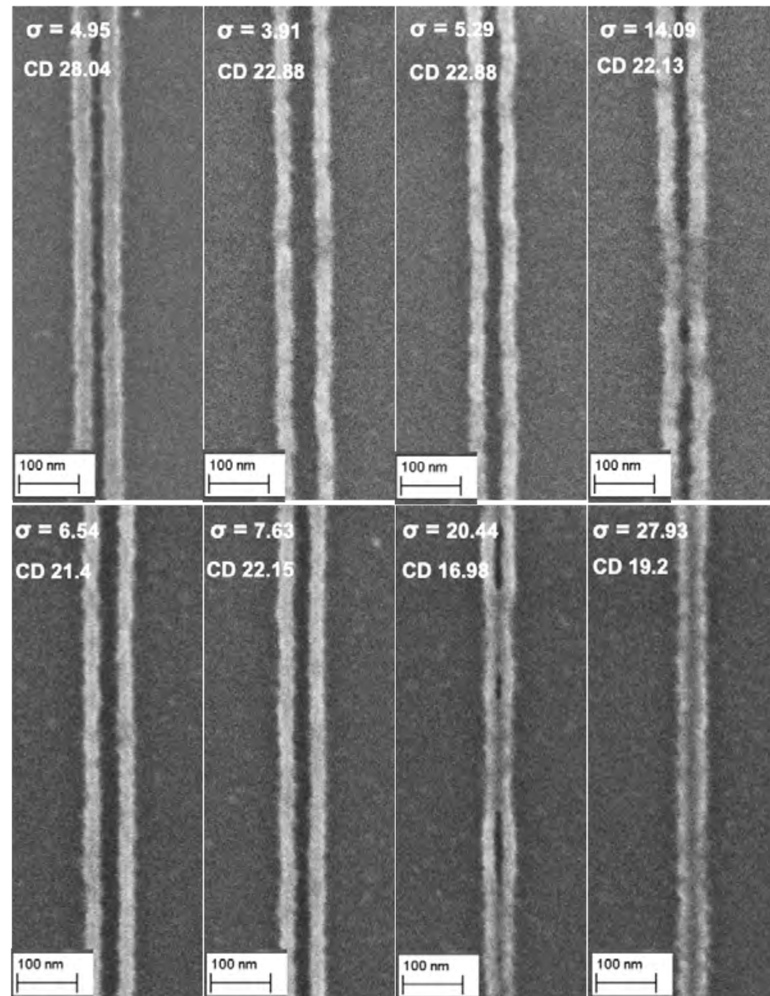

FIGURE 5.18: SEM images of various CDs at various pitch sizes patterned with EBL on 28 nm film thickness of resist on top of EDMSPA UL

When using the GPDEMS underlayer the first observation that can be made is that the roughness of the features increases and line roughness leads to increase in unbalanced the capillary forces, therefore the expectation would be for these features to be very easily collapsed at mechanical stress levels that are lower than on the other underlayers tested in this study. However, the range of values for the

mechanical stress the features on this underlayer withstand is not smaller than for the rest of underlayers.

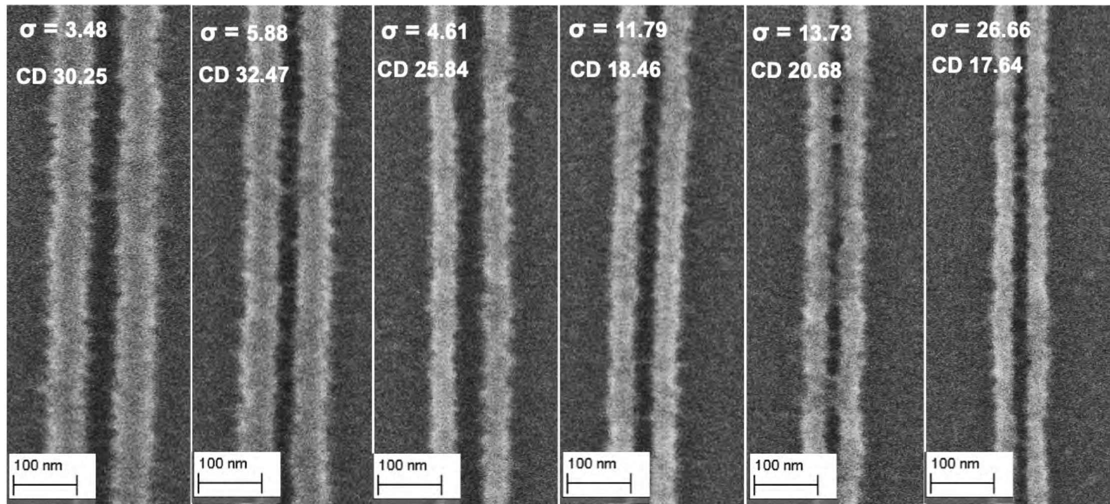

FIGURE 5.19: SEM images of various CDs at various pitch sizes patterned with EBL on 28 nm film thickness of resist on top of GPDEMS UL

Modulating the magnitude of the capillary forces through pattern design is one way of evaluating the mechanical stress on the resist features but there is a limitation on the pitch variation that can be used in order to significantly change the mechanical stress applied. Another way to further increase the mechanical stress on the features is to pattern with a higher aspect ratio. This is practically achieved by using a higher resist film thickness without changing the range of line widths in the pattern. In figure 5.20 the resist film thickness was increased from 28 nm to 34 nm and the TEVS underlayer was used. It can easily be noticed that the mechanical stress levels are significantly increased in this experiment with some of the features enduring as high as 88 MPa.

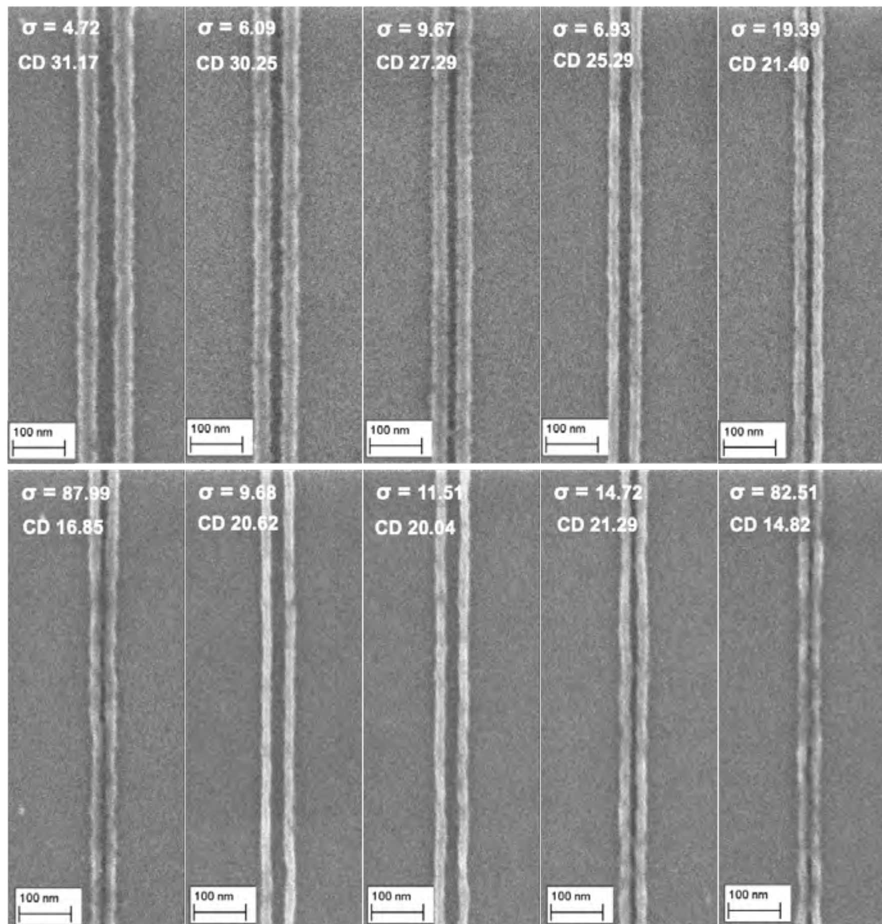

FIGURE 5.20: SEM images of various CDs at various pitch sizes patterned with EBL on 34 nm film thickness of resist on top of TEVS UL

Figure 5.21 shows lines patterned on the 34 nm resist thickness when using the EDMSPA as underlayer. As with the TEVS, here it can be seen that the range of values of the mechanical stress increases to a maximum of 80 MPa before the lines are completely collapsed.

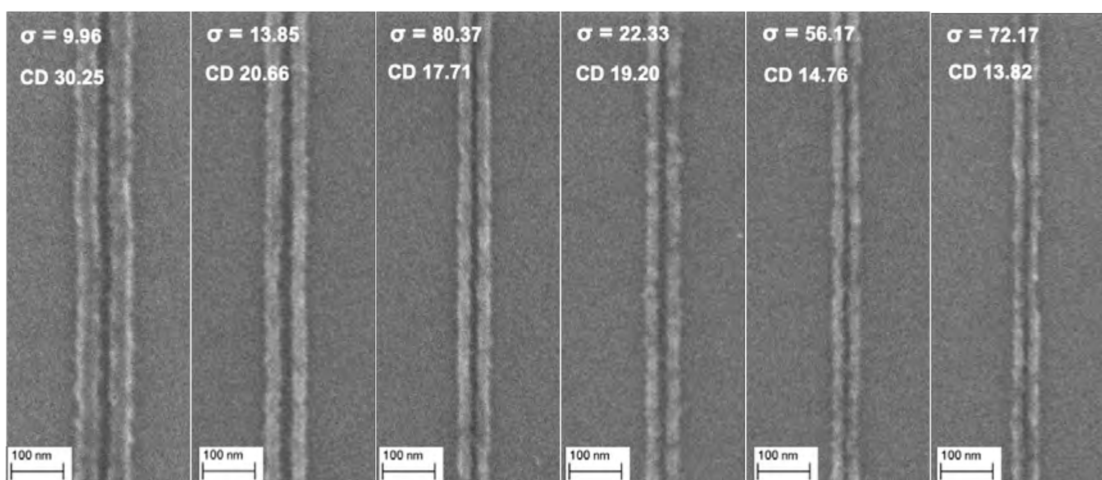

FIGURE 5.21: SEM images of various CDs at various pitch sizes patterned with EBL on 34 nm film thickness of resist on top of EDMSPA UL

On the other hand the contrast in the SEM images of the same resist material on the four different underlayers is different. This can be caused by a change in the line profile, with straight side walls giving better contrast. The orientation of the four different silane molecules in the self assembled monolayer seems to have an impact on the line profile as can be seen in the SEM images. However, the orientation of the silane molecules in the SAM is difficult to predict or control. There have been studies investigating the degree of order in the SAM organisation of a silane [135] but disorders can be easily introduced in these structures by defects on the surface of the substrate or by aggregation of the silane molecules in the solution to be deposited from.

Order could be introduced and imposed in the molecular orientation of the silane SAM formed on the substrate if the deposition is assisted by UV radiation as studied by Hacker et. al. [136].

However, Seeboth described in [137] by measuring the tilt of silane molecules in SAM and concluded that the perpendicular orientation increases with the deposition time up to a point where disorientation starts and a silane layer with homogeneous three-dimensional alignment could not be obtained.

The mechanical stress applied on features of different widths and at different pitches is graphically presented in figure 5.22 for all four underlayers evaluated in this study and for both thicknesses used to vary the aspect ratio of the features patterned. It is easily observed that for higher aspect ratios the calculated maximum mechanical stress applied on these features increased by a factor of ∼ 2.4. It can also be said that for features below 20 nm the stress range significantly increases for all four underlayers but most dramatically this effect is seen on EDMSPA and TEVS.

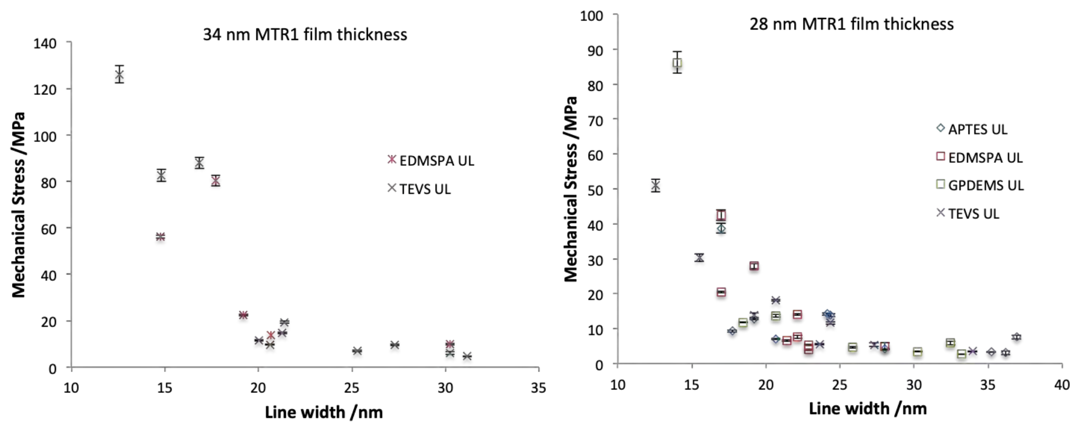

FIGURE 5.22: Mechanical stress in features patterned on 28 nm and 34 nm resist thickness on different silane underlayers

In figure 5.23 the mechanical stress at the collapse point is graphically presented as a function of the line width. It can be seen that for the lower aspect ratio features (28 nm) the stress at collapse point is situated below 50 MPa for all line widths and pitch sizes, whereas for the higher aspect ratio features patterned on the 34 nm thick resist film the stress at collapse point is situated mostly above 50 MPa.

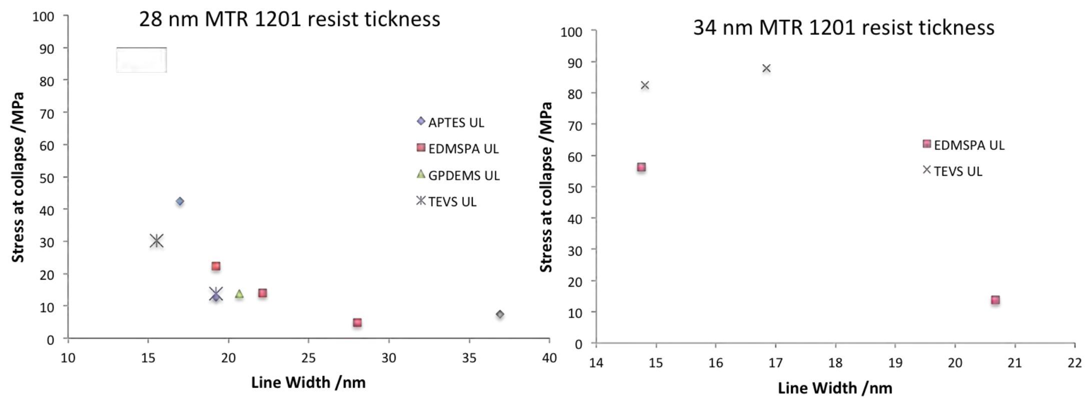

FIGURE 5.23: Mechanical stress in features patterned on 28 nm and 34 nm resist thickness on different silane underlayers at the collapse point

In order to further understand this relationship figure 5.24 shows the stress at the collapse point applied on features of very similar aspect ratio (same height, very similar width) which were patterned on the MTR1 on the four different silane underlayers.

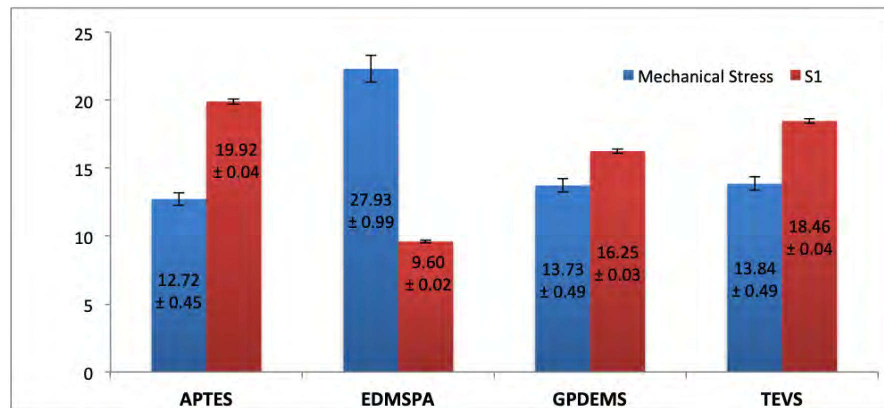

FIGURE 5.24: Mechanical stress and inner spacing (S_1) for 19 nm features patterned on 28 nm resist thickness on different silane underlayers at the collapse point

It was observed that for the same CD of the lines the collapse occurs at different spacings between the pair of lines. Therefore, although the mechanical stress values on the 19 nm width features patterned on the APTES UL, GPDEMS UL and TEVS UL are very close in value, it seems that the spacing, S_1 between these lines is different at the point of collapse. This indicates that the implementation

of different underlayers affects the adhesion of the features to the substrate differently and modulates the effect of different magnitudes of the capillary forces have on these features. Hence, at the collapse point the features on APTES UL experience higher capillary forces than features on TEVS UL and finally GPDEMS UL, which translates into: APTES UL is a better adhesion interface between the resist and the substrate than TEVS and GPDEMS are. With regards to EDMSPA the mechanical stress on 19 nm features is significantly higher than the other underlayers, therefore a fair comparison could not be made. Another interesting aspect that came out of this experiment is that the sensitivity of the resist seems to be affected by the underlayer used, but more interesting is the fact that this effect is different for each hp. For example, for designed hp 16 nm on TEVS UL a CD of 23.62 ± 0.03 nm was observed, 20.66 ± 0.03 nm on APTES, 22.70 ± 0.03 nm on EDMSPA and 17.64 ± 0.03 nm on GPDEMS. It would seem from here that the GPDEMS UL makes the resist the least sensitive. However at designed hp 30 nm the measured CD of features on EDMSPA UL is 28.04 ± 0.02 nm whereas the ones measured on GPDEMS UL are 33.20 ± 0.02 nm, therefore in this case the EDMSPA makes the resist less sensitive.

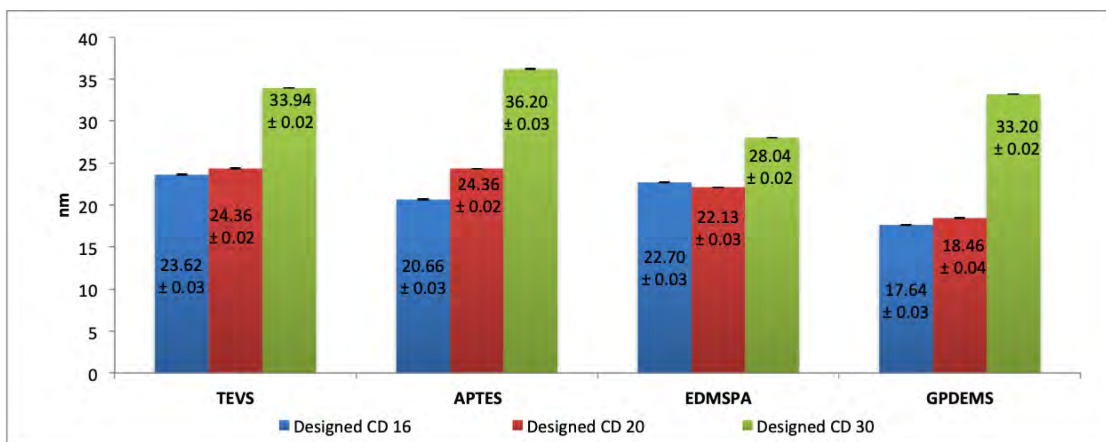

FIGURE 5.25: Measured CD of lines patterned at the same dose on the same resist at designed hp of 16 nm, 20 nm and 30 nm on different underlayers

This effect is most likely due to the difference in electronegativity of the molecules in the four different silane underalyers and their interaction mechanism with the

incident electrons during EBL. Larger CDs could be rendered by backscattered electrons from the UL.

5.4 UV Assisted and Active Rinse

Various post-lithography processes have been developed in the past decade to help with the reduction of resist features roughness. Chemical processes, ion-beam sputtering processes and plasma treatments [138, 139] have proved reductions in features roughness by 34% [140].

We have developed a new auxiliary process to suppress noise. MTR samples were exposed to UV flood exposure for 1 min during the rinse, strengthening the resist features against the capillary forces in the rinsing liquid. It was shown in chapter that exposure to light alone (without PEB) led to lower crosslinking density and in this chapter it was shown that applying a PEB increases LER. Higher doses of light can counteract this, but led to overexposure. However, if the resist is exposed to light after development, line broadening (overexposure) cannot occur, and the crosslinking density is increased making the resist stronger. If this is done after development but before the wafer is dried (ie during the rinse step) then the resist features should demonstrate less pattern collapse. This should render better defined features with lower LER. This experiment was designed to improve the contrast of the features patterned in the MTR resist and to reduce the defectivity encountered over large patterned areas.

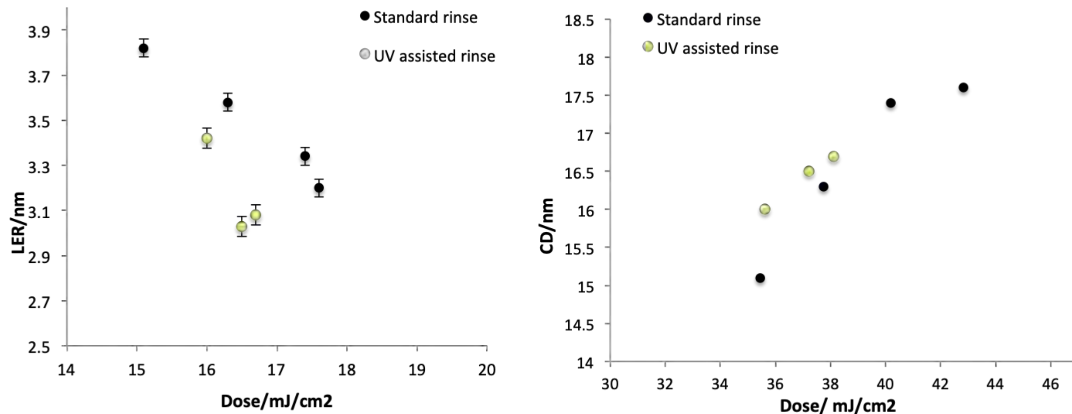

FIGURE 5.26: Line edge roughness and CD as a function of dose measured after rinse in standard rinse liquid, UV assisted rinse

When UV post-lithography exposure is applied during the rinse step the features are slightly larger as can be seen in figure 5.26. This is most likely due to the continuation of cross-linking reactions between active sites in the resist molecules leading to some broadening of features. The most important outcome from this experiment is the reduced LER obtained on the samples that received UV treatment during the rinse step. A drop of 12% was obtained after 1 min UV assisted rinse. Further experiments should be done where the rinse step time increases up to 3 min, which is the time interval when most of the resist thickness is retained in a flood exposure with UV light only.

Previous studies by the Henderson group showed that a reactive rinse enables the lines patterned in ESCAP-1 resist to withstand higher mechanical stresses, due to the fact that the silane containing rinse forms covalent crosslinks with phenols at the surface of the resist, improving its mechanical strength [134].

In the experiment presented below a similar principle was applied with the MTR chemistry, and the ability of achieving higher resolution when using reactive rinse was tested. In this case, instead of adding silane crosslinking agent to the rinse, additives that cause reactions in the MTR resist itself were used (ie the additives are not crosslinkers, but rather enable self crosslinking in the resist). Hydrochloric

acid, or acetic acid, were added to the rinse liquid at 1% concentration and the CD against dose and LER were then analysed. It can be observed in figure 5.27 that additional cross-linking occurs in acid containing rinse, since larger CDs are obtained in these samples.

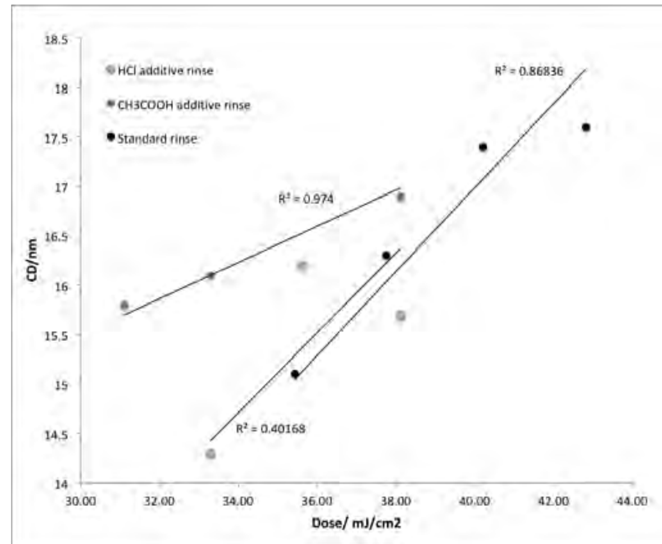

FIGURE 5.27: Line width as a function of dose measured after rinse in standard rinse liquid and acid additive rinse

The sensitivity gain is a plus for the industrial applications, however an enhancement in the resolution was the aim of this experiment. The LER as a function of the exposure dose is shown in figure 5.28. It appears that the lowest LER obtained in this experiment occurs on the sample in which the standard rinse was used. Below 35 mJ/cm^2 the HCl additive rinse shows the highest LER and the acetic acid gives LER values which are lower that the ones in HCl acid but higher than the ones obtained in the standard rinse. Above 35 mJ/cm^2 the acetic acid additive rinse gives LER values higher than the HCl additive rinse. Another observation that can be made after this experiment is that in the acetic acid additive rinse, the LER increases with the dose, which is opposite to the trend observed in HCl and in the standard rinse.

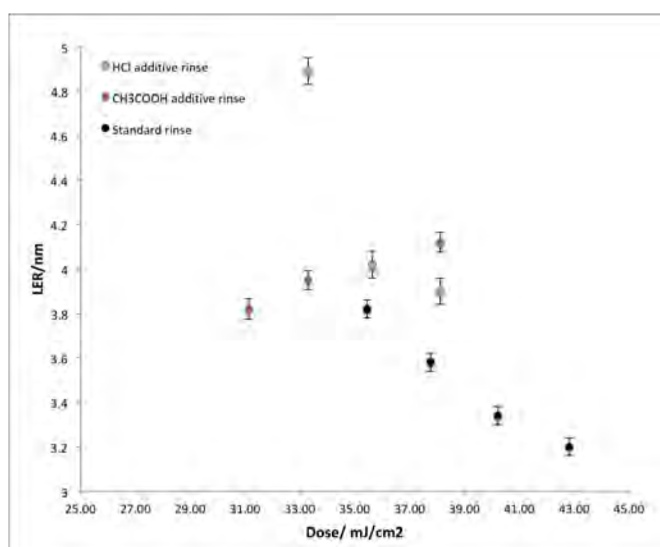

FIGURE 5.28: LER as a function of dose measured after rinse in standard rinse liquid, and acid additive rinse

In conclusion, although the surface cross-linking of the resist walls has occurred in the reactive rinse, the LER hasn't been reduced in these samples. On the other hand the dose for a specific CD decreased, which could be a good indicator that the photons stochastics and the secondary electrons blur are affecting the LER more than the intrinsic properties of the resist material do.

5.5 Conclusions

In this chapter different methods to achieve higher resolution in the MTR resist were evaluated. Unlike the previous chapters where the alteration of the MTR chemistry was discussed, this chapter evaluated modifications of the experimental conditions that can affect the roughness and ultimately the resolution of the MTR features in EUV lithography. Post exposure temperature variation was investigated and an optimum temperature of 30 °C was found to give the lowest LER in MTR3 system. Further experiments can be done with an improved resist where the protection groups can withstand temperatures higher than 90 °C, which was the limit of the range in this experiment.

Film thickness variation experiments were also performed in this chapter in order to find the optimal film thickness to be used in order to avoid pattern collapse. It was found that 22 ± 1 nm resist thickness is optimum to pattern 32 nm pitch lines and 18 ± 1 resist thickness for 28 nm pitch.

Pattern collapse was the next topic investigated in this chapter and the adhesion factor was analysed. The mechanical stress applied on features patterned on MTR resist was calculated for a series of different silane underlayers.

On TEVS, at highest aspect ratio tested in this experiment, 2.23, the mechanical stress applied on the lines which are ∼ 12 nm and separated by a distance equal to the linewidth has a magnitude of 51 MPa. At this point the lines are completely collapsed. If the spacing is kept constant and the lines slightly broaden from 12 nm to 15.50 nm, giving an aspect ratio of 1.81, the mechanical stress value decreases to ∼ 30 MPa and the lines are partially collapsed with sections which are bridged and sections which are standing. Keeping the spacing constant and further increasing the line width to ∼ 20 nm, giving aspect ratio of 1.36, decreases the mechanical stress on the lines to ∼ 18 MPa at which point, there is no collapse showing. It was observed that below 20 nm CD the lines are partially or completely collapsed if the spacing between them is equal to or less than the CD. However, for lines with CD larger than 20 nm, the spacing between the features can be decreased below the CD value with up to 10 nm without pattern collapse occurring. For example, lines with a CD of 24.36 ± 0.02 nm separated by 14 nm (1.7:1) can withstand a mechanical stress of 11.62 MPa without collapsing. On the other hand 19 nm lines with spacing of 18.46 nm are collapsing under a mechanical stress of 13.84 MPa.

Similarly, on APTES, lines with CD values lower than 20 nm can not be patterned at spacings equal to or less than the CD. Mechanical stress values of 12.72 MPa for 19 nm CD and 38.73 MPa for 17 nm CD are enough to induce pattern collapse in these features. However, 24 nm wide lines could be patterned without pattern collapse occurring at 12 nm spacing (2:1) on APTES.

On EDMPSA the line width to spacing ratio patterned without collapse was found to be lower than the one on APTES or TEVS, and 22 nm lines collapsed when the spacing between them was 14 nm. The spacing was increased to 32 nm to avoid pattern collapse. This is indication of the poor interaction of the silane underlayer with the resist film.

It was found that on GPDEMS, at collapse point, a mechanical stress as high as 87 MPa is applied on lines with aspect ratio of 2.35. A maximum stress of 13.73 MPa can be applied on lines patterned on this underlayer with an aspect ratio of 1.35 before collapse point. The mechanical stress doubles on features with slightly higher aspect ratio of 1.59 and spacing between the features increased by 3 nm.

Finally post-lithography conditions were also modified, and the rinse step was altered by the introduction of UV flood exposure and acid additives. Both methods proved beneficial for the sensitivity of the MTR. UV assisted rinsed features were $\sim$ 1 nm larger than the ones rinsed in standard solvent without UV at a given dose range.

On the other hand whereas UV post-litho flood exposures showed a decrease in the LER by 12%, the acid additives degraded the roughness of the features by more than 1 nm in comparison to standard rinse method.

Chapter 6

Final Conclusions and Future Work

In this thesis I presented the results obtained during my work on next generation lithography resists. Firstly, the lithographic performance of xMT negative tone molecular resist was presented together with variations of the system and their impact on the resist performance. It was shown that small modifications of the resin molecule affect the overall performance of the resist with EX2 and EX3 showing a lower sensitivity than xMT by 24% and 50% respectively. However, the EX2 showed lower 2% LER and EX3 showed 3% lower LER than the standard xMT.

Metal hybrid materials of xMT, EX2 and EX3 were also investigated with the goal of increasing the sensitivity of the resists, on the basis that metals have high EUV absorption coefficient than organic materials. For xMT and EX3 1% SnI_2 was added to the resist formulation and the sensitivity boost was not observed but sensitivity losses of 43% and 39% were found instead. Moreover the LER was significantly increased by 4.8% and 3.68%. In EX2 resist the SnI_2 was added in 1% and 2% concentrations. When added at 1% concentration the sensitivity of

the material increased by 25% but the LER was degraded by 10%. When the concentration of metal was increased to 2% the LER worsened by another 2%. This observation could mean that, whereas the metal in EX2 does absorb more photons, it also scatters more the secondary electrons produced in the exposed areas, producing more photoacids which diffuse uncontrollably in the film and increasing roughness.

Another experiment conducted with MIR xMT, EX2 and EX3 showed that extra-purification processes performed on the resin molecules have a large impact on the performance of the resist. MIR xMT was more sensitive than the non-MIR xMT by 16%, and the EX2 and EX3 sensitivity improved by over 55% after the MIR process.

Organic high-Z components such as Iodobenzene were also introduced in the resist systems and the lithographic performance monitored. In EX2, the iodobenzene showed a reduction of 0.5% at the expense of 6% of sensitivity compared to the standard EX2 material. Although the reduction in LER is not significant, it shows that iodine atoms from iodobenzene impact the resist chemistry differently to the way they impact the mechanism of exposure when added from SnI_2. This indicates that the range of scattering of iodine atoms is shorter than the range of scattering of tin atoms and therefore acid diffusion in this type of hybrid material is easier to control by customising the concentration of iodobenzene added to the resist formulation.

The last experiment presented in chapter 3 showed the best resolution achieved with xMT resist and presented in this thesis –12 nm lines patterned with EUV-IL on xMT resist with iodinated cross-linker.

The MTR concept was introduced in this thesis and the work conducted for elucidating the exposure mechanism of the MTR resist was presented. Investigating formulation optimisation in the MTR resist showed that there are optimum resin

levels to be used in MTR2 and MTR3 in order to obtain the lowest LER value. Increasing the resin ratio from standard to 4 times the standard resulted in both systems–MTR2 and MTR3–in a drop in sensitivity which was larger in MTR2 ($\sim$ 47 mJ/cm^2) than in MTR3 ($\sim$ 33 mJ/cm^2). The lowest LER value in MTR2 was found at resin ratio 0.45 and for MTR3 at resin ratio 0.46.

Performing EBL exposures on MTR formulations at various resin ratios with 3 different external quencher loadings showed that the MTR system hinders the effect of the external quencher at 0.92 MTR ratio. This indicates that there is an intrinsic quencher behaviour in the MTR system which can be adjusted by changing the MTR resin ratio in the formulation.

In the last chapter of the thesis I have presented approaches taken towards achieving better resolution in the resist materials herein presented by alteration of the process conditions pre- and post-exposure. The first approach was introducing a post-exposure bake and it was found that changing the temperature of the process, offered different results. The best LER obtained in this experiment was at 30 $^\circ$ C.

Film thickness variation experiments showed the optimum resist thickness for lowest LER value to be used when patterning 32 nm pitch lines was 22 $\pm$ 1 nm and 18 $\pm$ 1 nm when patterning 28 nm pitch lines.

The next approach taken towards increasing the resolution in the MTR system was addressing pattern collapse. For that purpose, 4 silane underlayers were introduced at the interface between the resist film and the silicon wafer. After calculating the mechanical stress applied on lines patterned on the different underlayers it was found that APTES provides a better adhesion interface than TEVS, EDMSPA and GPDEMS. Another interesting finding was that the underlayer affected the sensitivity of the resist. Thus, lines designed to have a CD of 20 nm for example were measured to have 24.35 $\pm$0.02 nm on TEVS, 24.37 $\pm$ 0.02 on APTES, 22.13 $\pm$ 0.03 on EDMSPA and 18.46 $\pm$ 0.04 nm on GPDEMS. This was attributed to

the difference in the elctronegativity of the silane molecules which constitute the underlayers.

Future work could be conducted with focus on designing and testing enhanced thermal stability xMT molecules, which can withstand PEB temperatures above 90°C and investigate how LER is affected.

Due to the iodine atom having a larger size than the other atoms in the iodinated cross-linker steric hindrance might limit the reaction of cross-linker molecules with each-other or with resin molecules during exposure. PEB studies could be further conducted using this material in order to investigate the effect that temperature has on the reaction. It is likely that a PEB applied to the exposed material would accelerate the motion/rotation of the cross-linker molecules, increasing the probability of reaction.

A new iodinated cross-linker could be synthesised with a longer spacer group between the epoxide group and the iodine atom in order to minimise steric hindrance. This type of material is expected to have higher sensitivity than the current iodinated cross-linker.

Combinational studies where each of the individual elements –such as high opacity, optimum MTR ratio, underlayer and post processing –are combined could then be undertaken.

Appendix A

Higher magnification-SuMMIT analysis

In figure A.1 the difference in the CD and LER values obtained from SuMMIT analysis on same sample imaged at different magnifications is shown. The 300000 magnification was used to image all the samples in the experiments presented in the thesis as a measure of consistency with all previous results and with other resist manufacturers. The 401380 magnification was chosen as alternative for this experiment.

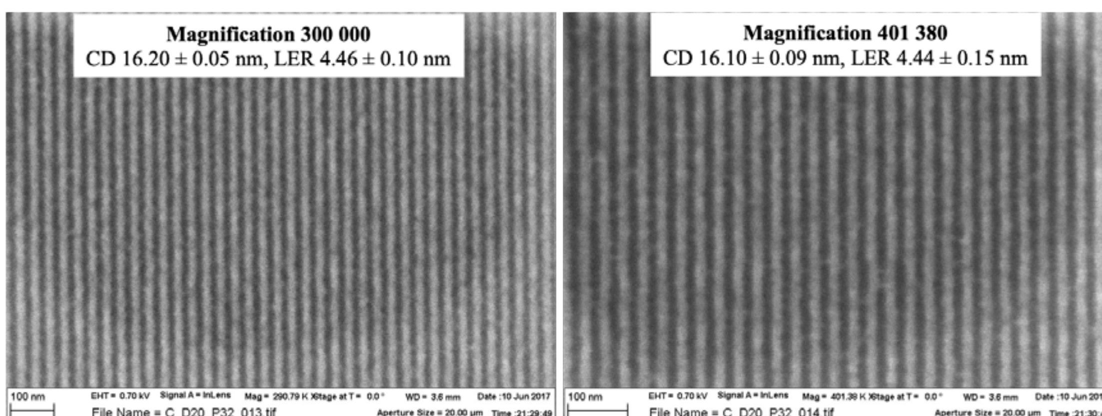

FIGURE A.1: Summit analysis results from lines imaged at 300k and 400k magnifications

The difference in CD between the two images is 0.1 nm, which is almost as low as the error measured on the CD in the image at 401380 magnification. The difference in the LER measured in the two images is of 0.02, this is 7.5 time lower than the error on the LER value measured in the higher magnification image.

It seems reasonable to use the lower magnification for the purpose of the experiments presented in this thesis since the information loss when using lower magnification is not significant. On the other hand, at magnification 300000 a physical area of the resist film of 1.08 mm^2 is being analysed in one image whereas at magnification 401380 the investigated area is 0.55 mm^2. In this case the lower magnification images offer more information about the resist performance than the higher ones.

However, for very small LER values, bellow 2 nm, higher magnification images should be taken to find any detail in the lines, but as it was shown in this thesis, LER is not very easy to improve, this might be a long while away.

Appendix B

Method used to calculate the efficiency of epoxide cross-linking from IR spectra

The epoxide peak at 894-944 cm^{-1} and the aromatic C-C peak at 1600-1650 cm^{-1} were monitored and used to calculate the cross-linking efficiency. Each peak was integrated and the area under the peak was calculated. Then the area of the epoxide peak was divided by the area of the C-C peak for each of the three spectra.

The graphs in figures B.1 and B.2 were re-plotted with data points from the original IR spectrum and extrapolated to define a complete peak. The area under the graphs was calculated using the original IR data, not using the extracted peaks. These peaks were plotted only to demonstrate the method.

Figure B.3 shows the original IR spectra containing all the peaks in the formulation.

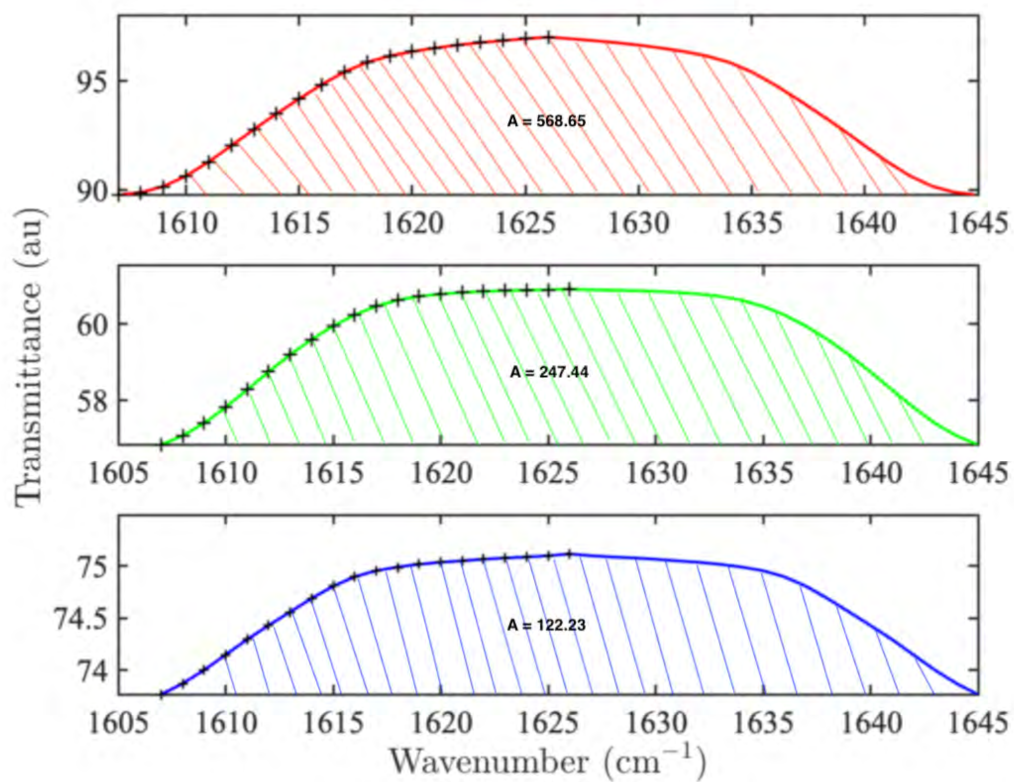

FIGURE B.1: Aromatic C-C stretch IR peak in formulations of cross-linker and photoacid generator: a) after drop casting, b) after 15 minutes exposure to UV light, c) exposed to UV for 15 minutes and received PEB

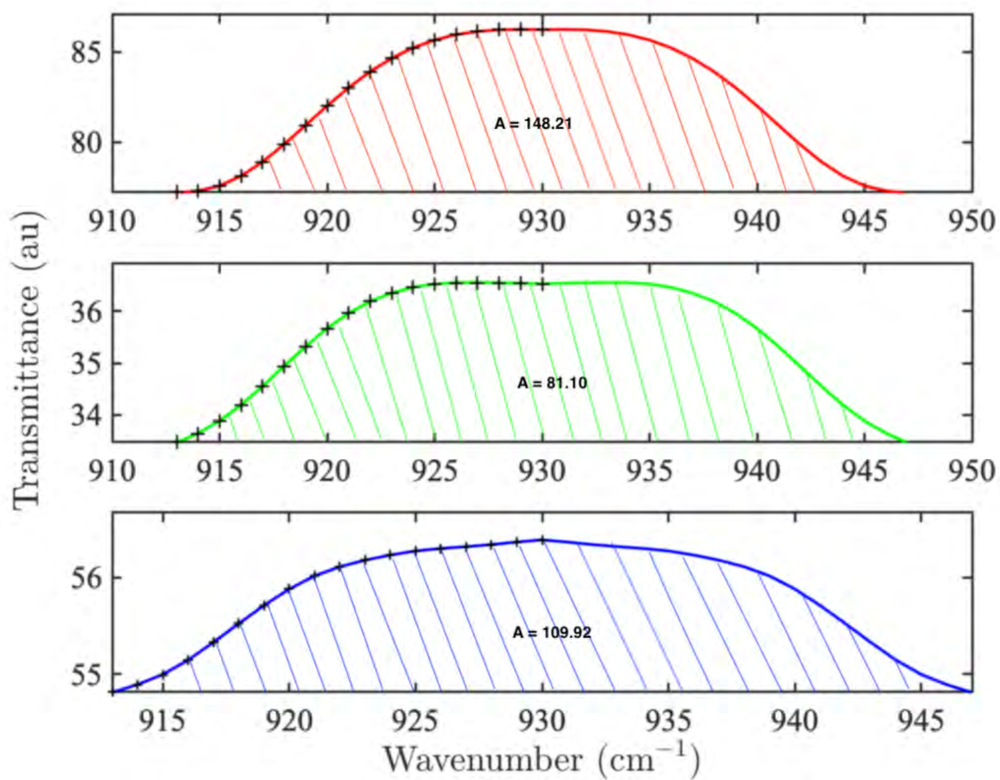

FIGURE B.2: Epoxide IR peak in formulations of cross-linker and photoacid generator: a) after drop casting, b) after 15 minutes exposure to UV light, c) exposed to UV for 15 minutes and received PEB

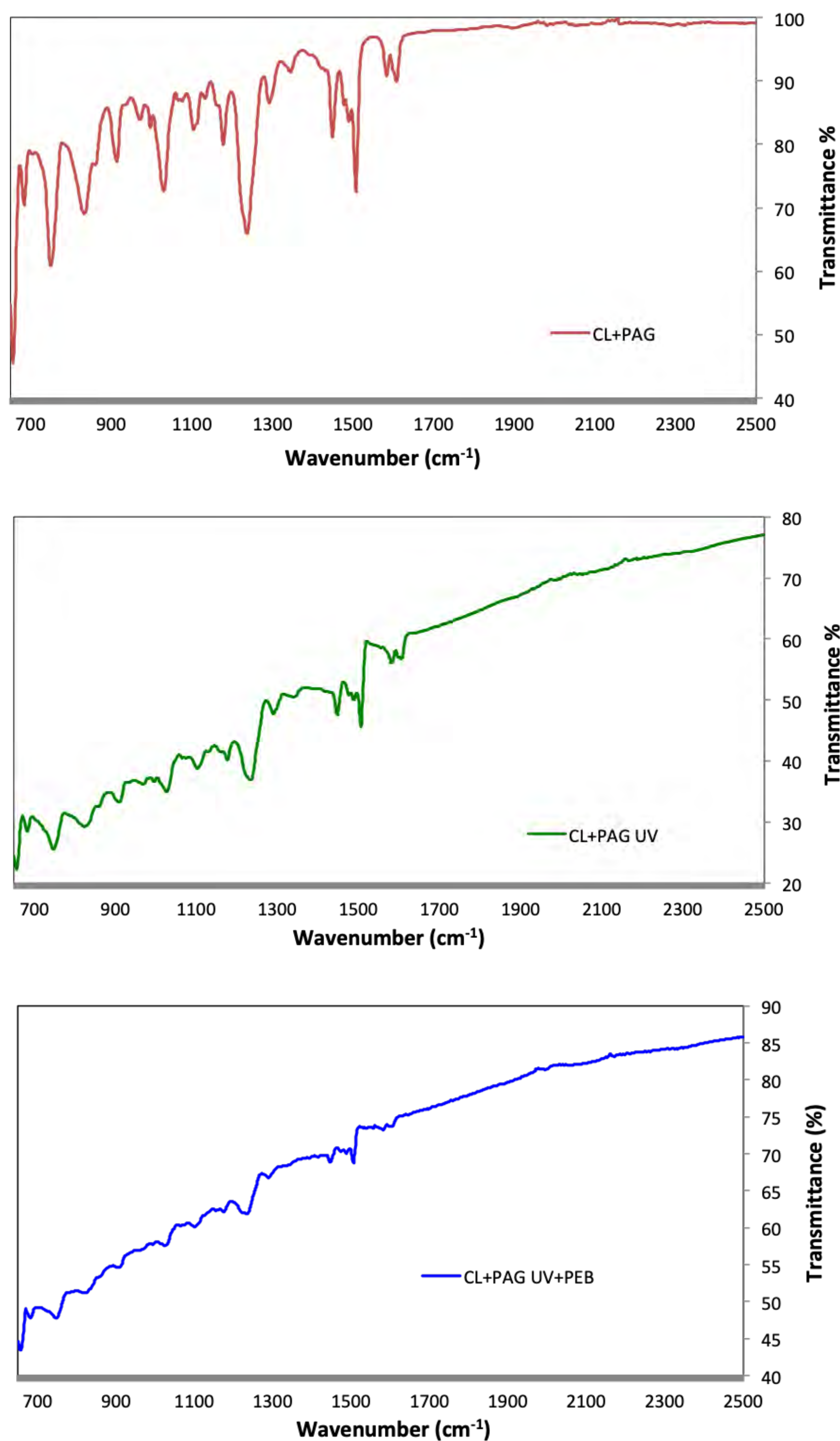

FIGURE B.3: IR complete spectra of formulations of cross-linker and photoacid generator: a) after drop casting, b) after 15 minutes exposure to UV light, c) exposed to UV for 15 minutes and received PEB

Bibliography

[1] WA Goddard, D Brenner, S Edward Lyshevski, and GJ Iafrate. Theres Plenty of Room at the Bottom: An Invitation to Enter a New Field of Physics. In *Handbook of Nanoscience, Engineering, and Technology*, pages 19–27. CRC Press, 2002.

[2] T Newman. Tiny Tale Gets Grand, California Institute Technol. *J. Eng. Sci*, 49:24, 1986.

[3] Hai-Dong Yu, Michelle D Regulacio, Enyi Ye, and Ming-Yong Han. Chemical routes to top-down nanofabrication. *Chemical Society Reviews*, 42(14):6006–6018, 2013.

[4] GM Whitesides. Nanoscience, Nanotechnology, and Chemistry. *Small*, 1(2): 172–179, 2005.

[5] H Shoji, Y Nakata, K Mukai, Y Sugiyama, M Sugawara, N Yokoyama, and H Ishikawa. Temperature Dependent Lasing Characteristics of Multi-Stacked Quantum Dot Lasers. *Applied physics letters*, 71(2):193–195, 1997.

[6] YS Tang, WX Ni, CM Sotomayor Torres, and GV Hansson. Fabrication and Characterisation of Si-$Si_{0.7}Ge_{0.3}$Quantum Dot Light Emitting Diodes. *Electronics Letters*, 31(16):1385–1386, 1995.

[7] CM Niemeyer. Nanoparticles, Proteins, and Nucleic Acids: Biotechnology Meets Materials Science. *Angewandte Chemie International Edition*, 40(22): 4128–4158, 2001.

[8] SY Chou. Patterned Magnetic Nanostructures and Quantized Magnetic Disks. *Proceedings of the IEEE*, 85(4):652–671, 1997.

[9] A. Senefelder. The Invention of Lithography. In Julius Washington Alois Senefelder, Muller, editor, *The Invention of Lithography*, volume 1 of *Frontiers of Nanoscience*. The Fuchs & Lang Manufacturing Company, 1911.

[10] Richard A Lawson. *Molecular resists for advanced lithography-design, synthesis, characterization, and simulation*. PhD thesis, Georgia Institute of Technology, 2011.

[11] GE Moore. Lithography and the Future of Moore's Law. In *Integrated Circuit Metrology, Inspection, and Process Control IX*, volume 2439, pages 2–18. International Society for Optics and Photonics, 1995.

[12] SE Thompson and S Parthasarathy. Moore's law: The Future of Si Microelectronics. *Materials Today*, 9(6):20–25, 2006.

[13] Zheng Cui. Nanofabrication: Principles, capabilities and limits: Second. *doi*, 10:978–3.

[14] A.P.G. Robinson. Top-down fabrication program-year 4. Technical report, University of Birmingham, 2013.

[15] H Levinson and W Arnold. In SPIE Handbook of Microlithography, Micromachining and Microfabrication; Rai-Choudhury, p., ed, 1997.

[16] Masafumi Hori, Takehiko Naruoka, Hisashi Nakagawa, Tomohisa Fujisawa, Takakazu Kimoto, Motohiro Shiratani, Tomoki Nagai, Ramakrishnan

Ayothi, Yoshi Hishiro, Kenji Hoshiko, et al. Novel euv resist development for sub-14nm half pitch. In *Extreme Ultraviolet (EUV) Lithography VI*, volume 9422, page 94220P. International Society for Optics and Photonics, 2015.

[17] N Mojarad, M Hojeij, L Wang, J Gobrecht, and Y Ekinci. Single-digit-resolution nanopatterning with extreme ultraviolet light for the 2.5 nm technology node and beyond. *Nanoscale*, 7(9):4031–4037, 2015.

[18] Elizabeth Buitrago, O Yildirim, C Verspaget, N Tsugama, R Hoefnagels, G Rispens, and Y Ekinci. Evaluation of euv resist performance using interference lithography. In *Extreme Ultraviolet (EUV) Lithography VI*, volume 9422, page 94221S. International Society for Optics and Photonics, 2015.

[19] Harun H Solak, Dongxing He, Weimin Li, Sangeet Singh-Gasson, Francesco Cerrina, Byeong-Hyeok Sohn, XM Yang, and P Nealey. Exposure of 38 nm period grating patterns with extreme ultraviolet interferometric lithography. *Applied Physics Letters*, 75(15):2328–2330, 1999.

[20] DC Ockwell, NCE Crosland, and VC Kempson. Synchrotron light as a source for extreme ultraviolet lithography. *Journal of Vacuum Science & Technology B: Microelectronics and Nanometer Structures Processing, Measurement, and Phenomena*, 17(6):3043–3046, 1999.

[21] VY Banine, JPH Benschop, and HGC Werij. Comparison of extreme ultraviolet sources for lithography applications. *Microelectronic Engineering*, 53 (1-4):681–684, 2000.

[22] D Colombant and GF Tonon. X-ray emission in laser-produced plasmas. *Journal of Applied Physics*, 44(8):3524–3537, 1973.

[23] Philip A Grunow, Leonard E Klebanoff, Samuel Graham, Steven J Haney, and W Miles Clift. Rates and mechanisms of optic contamination in the euv

engineering test stand. In *Emerging Lithographic Technologies VII*, volume 5037, pages 418–429. International Society for Optics and Photonics, 2003.

[24] Toshihisa Tomie, Tatsuya Aota, Yoshifumi Ueno, Gohta Niimi, Hidehiko Yashiro, Jingqian Lin, Isao Matsushima, Kazumasa Komiyama, Dong-Hoon Lee, Kentaro Nishigori, et al. Use of tin as a plasma source material for high conversion efficiency. In *Emerging Lithographic Technologies VII*, volume 5037, pages 147–156. International Society for Optics and Photonics, 2003.

[25] Troy W Barbee, Stanley Mrowka, and Michael C Hettrick. Molybdenum-silicon multilayer mirrors for the extreme ultraviolet. *Applied Optics*, 24(6): 883–886, 1985.

[26] K Boller, R-P Haelbich, H Hogrefe, W Jark, and C Kunz. Investigation of carbon contamination of mirror surfaces exposed to synchrotron radiation. *Nuclear Instruments and Methods in Physics Research*, 208(1-3):273–279, 1983.

[27] Shinya Fujii, Takahiro Kozawa, Kazumasa Okamoto, Julius Joseph Santillan, and Toshiro Itani. Shot noise limit of sensitivity of chemically amplified resists used for extreme ultraviolet lithography. *Japanese Journal of Applied Physics*, 54(11):116501, 2015.

[28] Ogletree D.F. Chapter 2 - Molecular Excitation and Relaxation of Extreme Ultraviolet Lithography Photoresists. In Alex Robinson and Richard Lawson, editors, *Materials and Processes for Next Generation Lithography*, volume 11 of *Frontiers of Nanoscience*, pages 91 – 113. Elsevier, 2016.

[29] Robin Santra, Jürgen Zobeley, Lorenz S Cederbaum, and Nimrod Moiseyev. Interatomic coulombic decay in van der waals clusters and impact of nuclear motion. *Physical review letters*, 85(21):4490, 2000.

[30] Robin Santra, Jürgen Zobeley, and Lorenz S Cederbaum. Electronic decay of valence holes in clusters and condensed matter. *Physical Review B*, 64 (24):245104, 2001.

[31] Kirill Gokhberg, Přemysl Kolorenč, Alexander I Kuleff, and Lorenz S Cederbaum. Site-and energy-selective slow-electron production through intermolecular coulombic decay. *Nature*, 505(7485):661, 2014.

[32] V Stumpf, P Kolorenč, K Gokhberg, and LS Cederbaum. Efficient pathway to neutralization of multiply charged ions produced in auger processes. *Physical review letters*, 110(25):258302, 2013.

[33] Robin Santra and Lorenz S Cederbaum. Coulombic energy transfer and triple ionization in clusters. *Physical review letters*, 90(15):153401, 2003.

[34] MA McCord and MJ Rooks. Handbook of Microlithography, Micromachining, and Microfabricaiton vol. *Rai-Choudhury, P., Bellingham, WA: SPIE Press*, 144, 1997.

[35] Araldo van de Kraats and Raghunath Murali. Proximity effect in e-beam lithography. *Atlanta, Georgia: Nanotechnoogy Research Center, Georgia Institute of Technoogy*, 2005.

[36] Ripon Kumar Dey and Bo Cui. Lift-off with solvent for negative resist using low energy electron beam exposure. *Journal of Vacuum Science & Technology B, Nanotechnology and Microelectronics: Materials, Processing, Measurement, and Phenomena*, 32(6):06F507, 2014.

[37] APG Robinson, RE Palmer, T Tada, T Kanayama, EJ Shelley, D Philp, and JA Preece. Exposure mechanism of fullerene derivative electron beam resists. *Chemical physics letters*, 312(5-6):469–474, 1999.

[38] LD Jackel, RE Howard, PM Mankiewich, HG Craighead, and RW Epworth. Beam energy effects in electron beam lithography: The range and intensity of backscattered exposure. *Applied Physics Letters*, 45(6):698–700, 1984.

[39] Paul FA Alkemade, Emma M Koster, Emile van Veldhoven, and Diederik J Maas. Imaging and nanofabrication with the helium ion microscope of the v an l eeuwenhoek laboratory in d elft. *Scanning*, 34(2):90–100, 2012.

[40] Kensuke Inai, Kaoru Ohya, and Tohru Ishitani. Simulation study on image contrast and spatial resolution in helium ion microscope. *Journal of electron microscopy*, 56(5):163–169, 2007.

[41] R Lawson. Molecular Resists for Advanced Lithography - Design , Synthesis , Characterization , and Simulation. (May), 2011.

[42] CA Mack. Pitch: The Other Resolution. *Microlithography World*, pages 23–24, 1998.

[43] A Yamaguchi, R Tsuchiya, H Fukuda, O Komuro, H Kawada, and T Iizumi. Characterization of Line-Edge Roughness in Resist Patterns and Estimations of its Effect on Device Performance. In *Metrology, Inspection, and Process Control for Microlithography XVII*, volume 5038, pages 689–699. International Society for Optics and Photonics, 2003.

[44] CH Diaz, HJ Tao, YC Ku, A Yen, and K Young. An Experimentally Validated Analytical Model for Gate Line-Edge Roughness (LER) Effects on Technology Scaling. *IEEE Electron Device Letters*, 22(6):287–289, 2001.

[45] K Patterson, JL Sturtevant, JR Alvis, N Benavides, D Bonser, N Cave, C Nelson-Thomas, WD Taylor, and KL Turnquest. Experimental Determination of the Impact of Polysilicon LER on sub-100-nm Transistor Performance. In *Metrology, Inspection, and Process Control for Microlithography*

XV, volume 4344, pages 809–815. International Society for Optics and Photonics, 2001.

[46] S Xiong, J Bokor, Q Xiang, P Fisher, IM Dudley, and P Rao. Gate Line-Edge Roughness Effects in 50-nm Bulk MOSFET Devices. In *Metrology, Inspection, and Process Control for Microlithography XVI*, volume 4689, pages 733–742. International Society for Optics and Photonics, 2002.

[47] A Asenov, S Kaya, and AR Brown. Intrinsic Parameter Fluctuations in Decananometer MOSFETs Introduced by Gate Line Edge Roughness. *IEEE Transactions on Electron Devices*, 50(5):1254–1260, 2003.

[48] Q Lin, CT Black, C Detavernier, L Gignac, K Guarini, B Herbst, H Kim, P Oldiges, KE Petrillo, and MI Sanchez. Does Line-Edge Roughness Matter?: FEOL and BEOL Perspectives. In *Advances in Resist Technology and Processing XX*, volume 5039, pages 1076–1086. International Society for Optics and Photonics, 2003.

[49] A Yamaguchi, K Ichinose, S Shimamoto, H Fukuda, R Tsuchiya, K Ohnishi, H Kawada, and T Iizumi. Metrology of LER: Influence of Line-Edge Roughness (LER) on Transistor Performance. In *Metrology, Inspection, and Process Control for Microlithography XVIII*, volume 5375, pages 468–477. International Society for Optics and Photonics, 2004.

[50] J-Y Lee, J Shin, H-W Kim, S-G Woo, H-K Cho, W-S Han, and J-T Moon. Effect of Line-Edge Roughness (LER) and Line-Width Roughness (LWR) on sub-100-nm Device Performance. In *Advances in Resist Technology and Processing XXI*, volume 5376, pages 426–434. International Society for Optics and Photonics, 2004.

[51] K Shibata, N Izumi, and K Tsujita. Influence of Line-Edge Roughness on MOSFET Devices with sub-50-nm Gates. In *Metrology, Inspection, and*

Process Control for Microlithography XVIII, volume 5375, pages 865–874. International Society for Optics and Photonics, 2004.

[52] S Bhattarai, AR Neureuther, and PP Naulleau. Simulation Study of the Influence of peb Reaction Rates on Resist LER. In *Extreme Ultraviolet (EUV) Lithography VI*, volume 9422, page 94222I. International Society for Optics and Photonics, 2015.

[53] S Bhattarai. Study of Line Edge Roughness and Interactions of Secondary Electrons in Photoresists for EUV Lithography. 2017.

[54] JS Villarrubia. Issues in Line Edge and Linewidth Roughness Metrology. In *AIP Conference Proceedings*, volume 788, pages 386–393. AIP, 2005.

[55] H Ito. Chemical Amplification Resists for Microlithography, 2005. ISSN 00653195.

[56] R Dammel. *Diazonaphthoquinone-Based Resists*, volume 11. SPIE press, 1993.

[57] H Ito. Chemical Amplification Resists: History and Development within IBM. *IBM Journal of research and development*, 41(1.2):119–130, 1997.

[58] H Lorenz, M Despont, N Fahrni, N LaBianca, P Renaud, and P Vettiger. Su-8: A Low-Cost Negative Resist for mems. *Journal of Micromechanics and Microengineering*, 7(3):121, 1997.

[59] Carmen Popescu, Alexandra McClelland, Guy Dawson, John Roth, Dimitrios Kazazis, Yasin Ekinci, Wolfgang Theis, and Alex PG Robinson. Multi-trigger resist for electron beam lithography. In *33rd European Mask and Lithography Conference*, volume 10446, page 1044608. International Society for Optics and Photonics, 2017.

[60] SV Postnikov, MD Stewart, HV Tran, MA Nierode, DR Medeiros, T Cao, J Byers, SE Webber, and CG Wilson. Study of resolution limits due to intrinsic bias in chemically amplified photoresists. *Journal of Vacuum Science & Technology B: Microelectronics and Nanometer Structures Processing, Measurement, and Phenomena*, 17(6):3335–3338, 1999.

[61] D Van Steenwinckel, JH Lammers, T Koehler, RL Brainard, and P Trefonas. Resist effects at small pitches. *Journal of Vacuum Science & Technology B: Microelectronics and Nanometer Structures Processing, Measurement, and Phenomena*, 24(1):316–320, 2006.

[62] T Yoshimura, Y Nakayama, and S Okazaki. Acid-diffusion effect on nanofabrication in chemical amplification resist. *Journal of Vacuum Science & Technology B: Microelectronics and Nanometer Structures Processing, Measurement, and Phenomena*, 10(6):2615–2619, 1992.

[63] Y Kawai, A Otaka, A Tanaka, and T Matsuda. The effect of an organic base in chemically amplified resist on patterning characteristics using KrF lithography. *Japanese Journal of Applied Physics*, 33(12S):7023, 1994.

[64] AR Pawloski and PF Nealey. The multifunctional role of base quenchers in chemically amplified photoresists. *Chemistry of materials*, 14(10):4192–4201, 2002.

[65] H Wu and KE Gonsalves. A novel single-component negative resist for DUV and electron beam lithography. *Advanced Materials*, 13(3):195–197, 2001.

[66] V Singh, VSV Satyanarayana, SK Sharma, S Ghosh, and KE Gonsalves. Towards novel non-chemically amplified (n-cars) negative resists for electron beam lithography applications. *Journal of Materials Chemistry C*, 2(12): 2118–2122, 2014.

[67] T Tada and T Kanayama. Nanolithography using fullerene films as an electron beam resist. *Japanese Journal of Applied Physics*, 35(1A):L63, 1996.

[68] J Manyam. *Novel resist materials for next generation lithography.* PhD thesis, University of Birmingham, 2011.

[69] FP Gibbons, APG Robinson, RE Palmer, M Manickam, and JA Preece. Ultrathin fullerene films as high-resolution molecular resists for low-voltage electron-beam lithography. *Small*, 2(8-9):1003–1006, 2006.

[70] H Okamura, DC Forman, and CK Ober. C_{60}-containing polymers for electron beam lithography. *Polymer Bulletin*, 71(9):2395–2405, 2014.

[71] DX Yang, Andreas Frommhold, X Xue, RE Palmer, and APG Robinson. Chemically amplified phenolic fullerene electron beam resist. *Journal of Materials Chemistry C*, 2(8):1505–1512, 2014.

[72] RG Hobbs. Semiconductor nanowire fabrication via bottom-up & top-down paradigms. 2011.

[73] H Namatsu, Y Takahashi, K Yamazaki, T Yamaguchi, M Nagase, and K Kurihara. Three-dimensional siloxane resist for the formation of nanopatterns with minimum linewidth fluctuations. *Journal of Vacuum Science & Technology B: Microelectronics and Nanometer Structures Processing, Measurement, and Phenomena*, 16(1):69–76, 1998.

[74] MJ Loboda, CM Grove, and RF Schneider. Properties of a-sio x: H thin films deposited from hydrogen silsesquioxane resins. *Journal of the Electrochemical Society*, 145(8):2861–2866, 1998.

[75] JKW Yang and KK Berggren. Using high-contrast salty development of hydrogen silsesquioxane for sub-10-nm half-pitch lithography. *Journal of Vacuum Science & Technology B: Microelectronics and Nanometer Structures Processing, Measurement, and Phenomena*, 25(6):2025–2029, 2007.

[76] AS Gangnaik, YM Georgiev, G Collins, and JD Holmes. Novel germanium surface modification for sub-10 nm patterning with electron beam lithography and hydrogen silsesquioxane resist. *Journal of Vacuum Science & Technology B, Nanotechnology and Microelectronics: Materials, Processing, Measurement, and Phenomena*, 34(4):041603, 2016.

[77] AE Grigorescu, MC Van der Krogt, CW Hagen, and P Kruit. 10 nm lines and spaces written in HSQ, using electron beam lithography. *Microelectronic Engineering*, 84(5-8):822–824, 2007.

[78] J Stowers and DA Keszler. High resolution, high sensitivity inorganic resists. *Microelectronic Engineering*, 86(4-6):730–733, 2009.

[79] A S. Gangnaik, YM. Georgiev, and JD Holmes. New Generation Electron Beam Resists: A Review. *Chemistry of Materials*, 29(5):1898–1917, 2017. ISSN 15205002.

[80] H Namatsu, K Kurihara, M Nagase, K Iwadate, and K Murase. Dimensional Limitations of Silicon Nanolines Resulting from Pattern Distortion due to Surface Tension of Rinse Water. *Applied Physics Letters*, 66(20):2655–2657, 1995. ISSN 0003-6951.

[81] SP Delcambre, RA Riggleman, JJ de Pablo, and PF Nealey. Mechanical Properties of Antiplasticized Polymer Nanostructures. *Soft Matter*, 6(11): 2475, 2010. ISSN 1744-683X.

[82] DL Goldfarb, RL Bruce, JJ Bucchignano, DP Klaus, MA Guillorn, and CJ Wu. Pattern Collapse Mitigation Strategies for EUV Lithography. In *Extreme Ultraviolet (EUV) Lithography III*, volume 8322, page 832205. International Society for Optics and Photonics, 2012.

[83] K Yoshimoto, C Higgins, A Raghunathan, JG Hartley, DL Goldfarb, H Kato, K Petrillo, ME Colburn, J Schefske, O Wood, et al. Revisit Pattern Collapse

for 14nm Node and Beyond. In *Advances in Resist Materials and Processing Technology XXVIII*, volume 7972, page 79720K. International Society for Optics and Photonics, 2011.

[84] G Winroth, R Gronheid, TR Younkin, and JM Blackwell. Critical Material Properties for Pattern Collapse MMitigation. *Journal of Micro/Nanolithography, MEMS, and MOEMS*, 11(3):033004, 2012.

[85] CM Stafford, BD Vogt, C Harrison, D Julthongpiput, and R Huang. Elastic Moduli of Ultrathin Amorphous Polymer Films. *Macromolecules*, 39(15): 5095–5099, 2006.

[86] KJ Alvine, Y Ding, JF Douglas, HW Ro, BC Okerberg, A Karim, KA Lavery, S Lin-Gibson, and CL Soles. Effect of Fluorosurfactant on Capillary Instabilities in Nanoimprinted Polymer Patterns. *Journal of Polymer Science, Part B: Polymer Physics*, 47(24):2591–2600, 2009. ISSN 08876266.

[87] S Hien, GK Rich, G Molina, HB Cao, and PF Nealey. Collapse Behavior of Single Layer 193-and 157-nm Resists: Use of Surfactants in the Rinse to Realize the sub-130-nm Nodes. In *Advances in Resist Technology and Processing XIX*, volume 4690, pages 254–262. International Society for Optics and Photonics, 2002.

[88] AE. Zweber, M Wagner, J DeYoung, and RG Carbonell. Mechanism of Extreme Ultraviolet Photoresist Development with a Supercritical CO2 Compatible Salt. *Langmuir*, 25(11):6176–6190, 2009. ISSN 07437463.

[89] Lee J-K Ober CK Ouyang, CY. Studies of Environmentally Friendly Solvent-based Developers. *Journal of Photopolymer Science and Technology*, 24(2): 239–240, 2011. ISSN 09149244.

[90] MY Lee, KM Do, HS Ganapathy, YS Lo, JJ Kim, SJ Choi, and KT Lim. Surfactant-Aided Supercritical Carbon Dioxide Drying for Photoresists to

Prevent Pattern Collapse. *Journal of Supercritical Fluids*, 42(1):150–156, 2007. ISSN 08968446.

[91] PG. Pape. *Adhesion promoters.* Elsevier Inc., 2011. ISBN 9781437744613.

[92] WK Cho, B Kong, HJ Park, J Kim, W Chegal, JS Choi, and IS Choi. Long-Term Stability of Cell Micropatterns on Poly((3-(Methacryloylamino)Propyl)-Dimethyl(3-Sulfopropyl)Ammonium Hydroxide)-Patterned Silicon Oxide Surfaces. *Biomaterials*, 31(36): 9565–9574, 2010. ISSN 01429612.

[93] JH Song and MJ Sailor. Chemical Modification of Crystalline Porous Silicon Surfaces. *Comments on Inorganic Chemistry*, 21(1-3):69–84, 1999. ISSN 0260-3594.

[94] CG Allen, DJ Baker, JM Albin, HE Oertli, DT Gillaspie, DC Olson, TE Furtak, and RT Collins. Surface modification of ZnO using triethoxysilane-based molecules. *Langmuir*, 24(23):13393–13398, 2008.

[95] EP Plueddemann. Silane coupling agents. *Additives for Plastics*, 1:123–167, 1978.

[96] Uzodinma Okoroanyanwu. Chemistry and lithography. SPIE Bellingham, WA, 2010.

[97] Yasin Ekinci, Michaela Vockenhuber, Mohamad Hojeij, Li Wang, and Nassir Mojarad. Evaluation of euv resist performance with interference lithography towards 11 nm half-pitch and beyond. In *Extreme Ultraviolet (EUV) Lithography IV*, volume 8679, page 867910. International Society for Optics and Photonics, 2013.

[98] Yasin Ekinci, Michaela Vockenhuber, Bernd Terhalle, Mohamad Hojeij, Li Wang, and Todd R Younkin. Evaluation of resist performance with euv interference lithography for sub-22-nm patterning. In *Extreme Ultraviolet*

(EUV) Lithography III, volume 8322, page 83220W. International Society for Optics and Photonics, 2012.

[99] Wen-Di Li, Wei Wu, and Richard Stanley Williams. Combined helium ion beam and nanoimprint lithography attains 4 nm half-pitch dense patterns. *Journal of Vacuum Science & Technology B, Nanotechnology and Microelectronics: Materials, Processing, Measurement, and Phenomena*, 30(6): 06F304, 2012.

[100] Xiaoqing Shi, Philip Prewett, Ejaz Huq, Darren M Bagnall, Alex PG Robinson, and Stuart A Boden. Helium ion beam lithography on fullerene molecular resists for sub-10 nm patterning. *Microelectronic Engineering*, 155:74–78, 2016.

[101] B. Päivänranta, A. Langner, E. Kirk, C. David, and Y. Ekinci. Sub-10 nm patterning using euv interference lithography. *Nanotechnology*, 22(37): 375302, 2011.

[102] W. Karim, S. A. Tschupp, M. Oezaslan, T. J. Schmidt, J. Gobrecht, J. A. van Bokhoven, and Y. Ekinci. High-resolution and large-area nanoparticle arrays using euv interference lithography. *Nanoscale*, 7(16):7386–7393, 2015.

[103] Brittany M McClinton and Patrick P Naulleau. Mask roughness induced ler: a rule of thumb. In *Extreme Ultraviolet (EUV) Lithography*, volume 7636, page 76362G. International Society for Optics and Photonics, 2010.

[104] Simi A George, Patrick P Naulleau, Ahila Krishnamoorthy, Zeyu Wu, Edward W Rutter, Joseph T Kennedy, Song Yuan Xie, Kyle Y Flanigan, and Thomas I Wallow. Characterization of line-edge roughness (ler) propagation from resists: underlayer interfaces in ultrathin resist films. In *Extreme Ultraviolet (EUV) Lithography*, volume 7636, page 763605. International Society for Optics and Photonics, 2010.

[105] Thomas Verduin, Pieter Kruit, and Cornelis W Hagen. Determination of line edge roughness in low-dose top-down scanning electron microscopy images. *Journal of Micro/Nanolithography, MEMS, and MOEMS*, 13(3): 033009, 2014.

[106] Stewart A Robertson, John J Biafore, Mark D Smith, Michael T Reilly, and Jerome Wandell. Predictive linewidth roughness and cdu simulation using a calibrated physical stochastic resist model. In *Advances in Resist Materials and Processing Technology XXVII*, volume 7639, page 763934. International Society for Optics and Photonics, 2010.

[107] M Lessel, O Bäumchen, M Klos, H Hähl, R Fetzer, R Seemann, and K Jacobs. Self-assembled silane monolayers: A step-by-step high speed recipe for high-quality, low energy surfaces. *arXiv preprint arXiv:1212.0998*, 2012.

[108] W-M Yeh. *Pattern Collapse in Lithographic Nanostructures: Quantifying Photoresist Nanostructure Behavior and Novel Methods for Collapse Mitigation.* PhD thesis, Georgia Institute of Technology, 2013.

[109] JK Stowers, A Telecky, M Kocsis, BL Clark, DA Keszler, A Grenville, CN Anderson, and PP Naulleau. Directly Patterned Inorganic Hardmask for EUV Lithography. In *Extreme Ultraviolet (EUV) Lithography II*, volume 7969, page 796915. International Society for Optics and Photonics, 2011.

[110] M Krysak, M Trikeriotis, E Schwartz, N Lafferty, P Xie, B Smith, P Zimmerman, W Montgomery, E Giannelis, and CK Ober. Development of an Inorganic Nanoparticle Photoresist for EUV, e-beam, and 193nm Lithography. In *Advances in Resist Materials and Processing Technology XXVIII*, volume 7972, page 79721C. International Society for Optics and Photonics, 2011.

[111] B Cardineau, R Del Re, H Al-Mashat, M Marnell, M Vockenhuber, Y Ekinci, C Sarma, M Neisser, DA Freedman, and RL Brainard. Euv Resists Based on

Tin-Oxo Clusters. In *Advances in Patterning Materials and Processes XXXI*, volume 9051, page 90511B. International Society for Optics and Photonics, 2014.

[112] T Fujii, S Matsumaru, T Yamada, Y Komuro, D Kawana, and K Ohmori. Patterning Performance of Chemically Amplified Resist in EUV Lithography. In *Extreme Ultraviolet (EUV) Lithography VII*, volume 9776, page 97760Y. International Society for Optics and Photonics, 2016.

[113] H Tsubaki, W Nihashi, T Tsuchihashi, and F Nishiyama. Negative-Tone Imaging with EUV Exposure Toward 13 nm hp. *Journal of Photopolymer Science and Technology*, 29(3):479–487, 2016.

[114] J Stowers, J Anderson, B Cardineau, B Clark, P De Schepper, J Edson, M Greer, K Jiang, M Kocsis, S Meyers, et al. Metal Oxide EUV Photoresist Performance for N7 Relevant Patterns and Processes. In *Advances in Patterning Materials and Processes XXXIII*, volume 9779, page 977904. International Society for Optics and Photonics, 2016.

[115] P Argitis, VP Vidali, and D Niakoula. Chapter 9 - Positive Molecular Resists. In Alex Robinson and Richard Lawson, editors, *Materials and Processes for Next Generation Lithography*, volume 11 of *Frontiers of Nanoscience*, pages 319 – 348. Elsevier, 2016.

[116] E Buitrago, S Nagahara, O Yildirim, H Nakagawa, S Tagawa, M Meeuwissen, T Nagai, T Naruoka, C Verspaget, R Hoefnagels, et al. Sensitivity Enhancement of Chemically Amplified Resists and Performance Study Using EUV Interference Lithography. In *Extreme Ultraviolet (EUV) Lithography VII*, volume 9776, page 97760Z. International Society for Optics and Photonics, 2016.

[117] DX. Yang, A Frommhold, A McClelland, J Roth, M Rosamond, EH Linfield, J Osmond, RE Palmer, and APG Robinson. Performance of a High Resolution Chemically Amplified Electron Beam Resist at Various Beam Energies. *Microelectronic Engineering*, 155:97–101, 2016. ISSN 01679317.

[118] Carmen Popescu, Andreas Frommhold, Alexandra McClelland, John Roth, Yasin Ekinci, and Alex PG Robinson. Sensitivity enhancement of the high-resolution xmt multi-trigger resist for euv lithography. In *Extreme Ultraviolet (EUV) Lithography VIII*, volume 10143, page 101430V. International Society for Optics and Photonics, 2017.

[119] R. A. Lawson, A Frommhold, D Yang, and A.P.G. Robinson. Chapter 8 - Negative-Tone Organic Molecular Resists. In Alex Robinson and Richard Lawson, editors, *Materials and Processes for Next Generation Lithography*, volume 11 of *Frontiers of Nanoscience*, pages 267 – 318. Elsevier, 2016.

[120] RL Bristol and ME Krysak. Lithographic Stochastics: Beyond 3σ. *Journal of Micro/Nanolithography, MEMS, and MOEMS*, 16(2):023505, 2017.

[121] S Bhattarai, W Chao, S Aloni, AR Neureuther, and PP Naulleau. Analysis of Shot Noise Limitations Due to Absorption Count in euv Resists. In *Extreme Ultraviolet (EUV) Lithography VI*, volume 9422, page 942209. International Society for Optics and Photonics, 2015.

[122] T Kozawa and T Tamura. Theoretical Study on Effects of Exposure Pattern Width on Line Edge Roughness and Stochastic Defect Generation in Fabrication of 16-nm-Half-Pitch Line-and-Space Patterns by Electron Beam Lithography.

[123] R Fallica, JK Stowers, A Grenville, A Frommhold, APG Robinson, and Y Ekinci. Dynamic Absorption Coefficients of CAR and non-CAR Resists at EUV. In *Extreme Ultraviolet (EUV) Lithography VII*, volume 9776, page 977612. International Society for Optics and Photonics, 2016.

[124] E Buitrago, TS Kulmala, R Fallica, and Y Ekinci. EUV Lithography Process Challenges. In *Frontiers of Nanoscience*, volume 11, pages 135–176. Elsevier, 2016.

[125] D De Simone, M Mao, F Lazzarino, and G Vandenberghe. Metal Containing Resist Readiness for HVM EUV Lithography. *Journal of Photopolymer Science and Technology*, 29(3):501–507, 2016.

[126] C Popescu, D Kazazis, A McClelland, G Dawson, J Roth, W Theis, Y Ekinci, and APG Robinson. High-resolution euv lithography using a multi-trigger resist. In *Extreme Ultraviolet (EUV) Lithography IX*, volume 10583, page 105831L. International Society for Optics and Photonics, 2018.

[127] Carmen Popescu, Yannick Vesters, Alexandra McClelland, Danilo De Simone, Guy Dawson, John Roth, Wolfgang Theis, Geert Vandenberghe, and Alex PG Robinson. Multi trigger resist for euv lithography. *Journal of Photopolymer Science and Technology*, 31(2):227–232, 2018.

[128] Yannick Vesters, Alexandra McClelland, Danilo De Simone, Carmen Popescu, Guy Dawson, John Roth, Wolfgang Theis, Geert Vandenberghe, and Alex PG Robinson. Multi-trigger resist patterning with asml nxe3300 euv scanner. In *Extreme Ultraviolet (EUV) Lithography IX*, volume 10583, page 1058308. International Society for Optics and Photonics, 2018.

[129] P Naulleau. Chapter 5 - EUV Lithography Patterning Challenges. In Alex Robinson and Richard Lawson, editors, *Materials and Processes for Next Generation Lithography*, volume 11 of *Frontiers of Nanoscience*, pages 177 – 192. Elsevier, 2016.

[130] JN Helbert and N Saha. Application of Silanes for Promoting Resist Patterning Layer Adhesion in Semiconductor Manufacturing. *Journal of Adhesion Science and Technology*, 5(10):905–925, 1991. ISSN 15685616.

[131] G Dormán and GD Prestwich. Benzophenone Photophores in Biochemistry. *Biochemistry*, 33(19):5661–5673, 1994. ISSN 15204995.

[132] O Prucker, CA Naumann, J Rühe, W Knoll, and CW Frank. Photochemical Attachment of Polymer Films to Solid Surfaces via Monolayers of Benzophenone Derivatives. *Journal of the American Chemical Society*, 121(38): 8766–8770, 1999. ISSN 00027863.

[133] Z Liu, Z Li, H Zhou, G Wei, Y Song, and L Wang. Immobilization and Condensation of DNA with 3-aminopropyltriethoxysilane Studied by Atomic Force Microscopy. *Journal of microscopy*, 218(3):233–239, 2005.

[134] W-M Yeh, DE Noga, RA Lawson, LM Tolbert, and CL Henderson. Comparison of Positive Tone Versus Negative Tone Resist Pattern Collapse Behavior. *Journal of Vacuum Science & Technology B, Nanotechnology and Microelectronics: Materials, Processing, Measurement, and Phenomena*, 28 (6):C6S6–C6S11, 2010. ISSN 2166-2746.

[135] Ishida H and Koenig JL. Molecular Organization of the Coupling Agent Interphase of FiberGlass Reinforced Plastics. *Journal of Polymer Science: Polymer Physics Edition*, 17(10):1807–1813.

[136] CA. Hacker, KA. Anderson, JL Richter, and CA Richter. Comparison of Si-O-C Interfacial Bonding of Alcohols and Aldehydes on Si(111) Formed from Dilute Solution with Ultraviolet Irradiation. *Langmuir*, 21(3):882–889, 2005. ISSN 07437463.

[137] A Seeboth and W Hettrich. Spatial Orientation of Highly Ordered Self-assembled Silane Monolayers on Glass Surfaces. *Journal of Adhesion Science and Technology*, 11(4):495–505, 1997.

[138] S Kobayashi, S Shimura, T Kawasaki, K Nafus, S Hatakeyama, H Shite, E Nishimura, M Kushibiki, A Hara, R Gronheid, et al. LWR Reduction by

Novel Lithographic and Etch Techniques. In *Advances in Resist Materials and Processing Technology XXVII*, volume 7639, page 763914. International Society for Optics and Photonics, 2010.

[139] P Foubert, AV Pret, EA Sanchez, and R Gronheid. Impact of Post-Litho LWR Smoothing Processes on the Post-etch Patterning Result. In *Advances in Resist Materials and Processing Technology XXVIII*, volume 7972, page 797213. International Society for Optics and Photonics, 2011.

[140] A Vaglio-Pret, R Gronheid, and P Foubert. Roughness Characterization in the Frequency Domain and Linewidth Roughness Mitigation with Post-Lithography Processes. *Journal of Micro/Nanolithography, MEMS, and MOEMS*, 9(4):041203, 2010.